

© 2018 by Bryan Medaris Kerns. All rights reserved.

A MEASUREMENT OF THE x DEPENDENT SEA FLAVOR ASYMMETRY AT
SEAQUEST

BY

BRYAN MEDARIS KERNS

DISSERTATION

Submitted in partial fulfillment of the requirements
for the degree of Doctor of Philosophy in Physics
in the Graduate College of the
University of Illinois at Urbana-Champaign, 2018

Urbana, Illinois

Doctoral Committee:

Professor Matthias Gross Perdekamp, Chair
Professor Naomi C. R. Makins, Director of Research
Professor Aida X El-Khadra
Professor Peter Abbamonte

Abstract

SeaQuest is a fixed target forward spectrometer experiment located at Fermilab which uses a 120 GeV proton beam on liquid hydrogen, liquid deuterium, and several solid targets. The flagship measurement of this experiment is to use the Drell-Yan process to improve the accuracy of the antiquark PDFs in the parton momentum fraction x range 0.1 to 0.58. By measuring the cross section ratio of $\sigma_{pd}(x)/\sigma_{pp}(x)$ one can derive an estimate of the proton sea flavor asymmetry, \bar{d}/\bar{u} , as a function of x .

This measurement is of interest to many theoreticians who have proposed several different classes of models in order to simulate the inner workings of the proton, a good test of these models is how well they predict the sea flavor asymmetry. A measurement from a previous experiment, E866, measured $\bar{d} < \bar{u}$ at x above 0.3. The models proposed so far do not predict $\bar{d} < \bar{u}$ at any x , so the accuracy of the E866 experiment in this region is of great interest.

An analysis of some but not all of the data collected by SeaQuest is presented in this paper. It contains a measurement of $\sigma_{pd}(x)/\sigma_{pp}(x)$, the application of several corrections and uncertainties to this measurement, and the derivation of $\bar{d}(x)/\bar{u}(x)$ from this measurement. Major corrections and uncertainties are the rate dependence correction and the target contamination correction. Particular care is paid to how to correctly merge the results from multiple data sets and optimizing the accuracy of estimating the value of parton momentum fraction x from measured quantities. The most notable feature of these results is that \bar{d}/\bar{u} is not less than one at any value of x , and is above one by several σ where E866 measured \bar{d}/\bar{u} below one.

Acknowledgments

This research would not have been possible without the support of the National Science Foundation, via grant No. 1506416.

I would like to thank my advisor, Naomi Makins, for sharing her enthusiasm for physics, which is what first drew me to her group. I would like to offer my thanks to the professionals in the McKinley Mental Health department, without which it is possible my anxiety and depression would have prevented me from completing this thesis. I would also like to thank the physics department at the University of Illinois, Urbana-Champaign, for not kicking me to the curb when I took much longer than usual to complete my degree requirements.

Table of Contents

List of Figures	vi
List of Tables	x
Chapter 1 Background	1
1.1 Proton Structure	1
1.2 Deep Inelastic Scattering	3
1.3 Drell-Yan Process	5
1.4 Gottfried Sum Rule	8
1.5 Sea Flavor Asymmetry in Past Experiments	10
1.5.1 New Muon Collaboration	10
1.5.2 NA51	10
1.5.3 E866/NuSea	12
1.6 Motivation	13
1.7 Models	16
Chapter 2 Experimental Setup	21
2.1 Timeline	22
2.2 Beam	23
2.3 Targets	27
2.4 Magnets	32
2.5 Detectors	36
2.5.1 Hodoscopes	36
2.5.2 Drift Chambers	38
2.5.3 Proportional Tubes	41
2.6 Trigger	43
2.7 DAQ	45
2.8 Tracking	47
2.9 Production Overview	51
Chapter 3 Monte Carlo	53
3.1 Generators	53
3.1.1 Gun Generator	53
3.1.2 Dimuon Generator	54
3.2 Physics List	55
3.3 Geometry	55
3.4 Output	57
3.5 Running GMC	58
3.5.1 Commands	59
3.6 GMC Improvements	59
3.7 MySQL Usage	61

Chapter 4	Analysis	63
4.1	Kinematic Variables	63
4.2	Cuts	69
4.2.1	Spill Level	69
4.2.2	Event Level	72
4.3	Rate Dependence Corrections	79
4.3.1	QIE Pedestal	80
4.3.2	Chamber Intensity	83
4.3.3	kTracker Efficiency	84
4.3.4	Empty Flask Correction	91
4.3.5	Remaining Rate Dependence	94
4.4	Target Contamination	100
4.5	Logarithm of the Ratio	101
4.6	Cross Section Ratio Calculation	104
4.7	\bar{d}/\bar{u} Extraction	110
Chapter 5	Results	115
5.1	Cross Section Ratio	115
5.2	\bar{d}/\bar{u}	119
Chapter 6	Conclusions	122
References		124

List of Figures

1.1	CT10 PDFs from the CTEQ collaboration[12][13].	3
1.2	Feynman diagram for deep inelastic scattering. Time flows from left to right. The particle exchanged does not have to be a photon, it can be any electroweak gauge boson.	4
1.3	Feynman diagram for the Drell-Yan process. Time flows from left to right. The particle exchanged could also be a Z-boson, but at SeaQuest our energies are too low.	6
1.4	A graph of the average p_T versus \sqrt{s} [16].	8
1.5	A diagram of the Collins Soper plane[21].	9
1.6	Data from NMC. The black points use the scale to the right and are $F_2^p - F_2^n$ for that bin in x . The white points use the scale to the left and are the integral of $F_2^p - F_2^n$ from that value of x to 1. The white points are extrapolated to reach a value of S_G , which is significantly below the predicted value of 1/3 (Labelled with QPM).	11
1.7	The cross section ratio $\sigma_{pd}/2\sigma_{pp}$ results binned in x for E866. Predictions from various PDFs are also shown.	13
1.8	\bar{d}/\bar{u} binned as a function of x , from E866. Predictions from various PDFs are also shown. There is a significant difference at high x for PDF sets published before the E866 results in 1998 and those published after the E866 results. The drop below $\bar{d}/\bar{u} = 1$ at higher x was completely unexpected.	14
1.9	The dimuon mass spectrum from E866. Notice the J/Ψ and Ψ' peaks between 3 and 4 GeV. It also drops off quickly with mass[30].	15
1.10	The J/Ψ cross section as a function of \sqrt{s} . It grows quickly with higher energies[31].	16
1.11	Estimated statistical uncertainties for SeaQuest, compared to E866[29]. While we have fallen short of this goal, we have still improved upon the E866 measurement from about $x = 0.15$ to 0.35 and roughly measured the asymmetry at x up to 0.58.	17
1.12	Comparison of two similar meson cloud models to E866 data. The dotted line parametrises the pion as having an effective mass of 400 MeV inside the proton. Both approach $\bar{d} = \bar{u}$ at high x [35].	18
1.13	E866 data and the NA51 data point plotted with two variants of the Chiral Quark model (red and blue curves). The authors note that they could not get the ratio below 1 in their models[36].	19
1.14	A comparison of E866 and NA51 data with a Chiral Quark Soliton model (solid line) and several PDF sets[37]. This uses the early E866 data without a statistically significant $\bar{d} < \bar{u}$	19
1.15	A statistical model compared to E866 data. The solid line is the prediction from the statistical model[38]. In this model \bar{d}/\bar{u} keeps increasing.	20
2.1	A figure of the SeaQuest spectrometer.	22
2.2	A plot of protons in each bucket. The booster batch and turn structure is visible. A typical reconstructed event has 25,000 protons and our intensity cut (data quality cut, not inhibit threshold) is at 60,000 protons. Super bucket spikes (those crossing the red line) are visible about once a turn. A single super bucket causes dead time for dozens of turns if it is not inhibited.	24

2.3	A diagram of a splat event, generated by the SeaView program. Most of the detector elements have fired.	24
2.4	A diagram of a clean event, generated by the SeaView program. It is much more clear than the splat event.	25
2.5	The distribution of intensity within buckets in our beam. This was taken from the intensity of events from our random trigger, NIM3. These are after the inhibit is in place.	26
2.6	The distribution of intensity of triggering buckets in reconstructed dimuons.	27
2.7	A diagram of the target table.	28
2.8	This graph shows reconstructed GMC dimuons originating from the target, reconstructed GMC dimuons originating from the beam dump, and all reconstructed dimuons from data. The z origin peaks from target and beam dump merge and are hard to separate without cutting a lot of data.	33
2.9	This graph shows the spectrum of energy loss of muons passing through FMag. It was generated from a Geant4 simulation.	34
2.10	These graphs show the results of the reconstruction software running on Monte Carlo simulated data with a magnetic field strength multiplier. Inaccurate field strengths result in residuals in the reconstruction of the mass and z origin. The mass residual is positively correlated with both the FMag and KMag multipliers, while the z origin residual is positively correlated with the FMag multiplier and negatively correlated with the KMag multiplier.	35
2.11	A diagram of a set of drift chambers in station 3. Most drift chambers have more tightly spaced cathodes in the cathode plane.	40
2.12	A diagram of the prop tubes. The labelling for the horizontally aligned prop tubes is shown.	42
2.13	A diagram of the prop tubes. The labelling for the vertically aligned prop tubes are shown.	42
2.14	A diagram of rate dependence after various forms of cluster removal. Delta ray removal has a much stronger effect than all other cluster removal combined.	48
2.15	A diagram of how the sagittas are calculated.	49
2.16	Graphs of the sagitta ratio r_1/r_2 for the X and U views. They peak fairly sharply, enabling this to be used as a cut early on in the tracking process.	49
4.1	This graph shows reconstructed GMC dimuons originating from the target with the target cut applied and reconstructed GMC dimuons originating from the beam dump with the dump cut applied.	74
4.2	This graph shows dimuons reconstructed from data separated by the target and dump cuts.	75
4.3	Graphs of the mass spectrum with different intensity cuts. The 5 to 6 GeV peak is much stronger at high intensity.	76
4.4	Graphs of the track z momentum spectrum for different numbers of hits per track. That low momentum tracks are much rarer at high quality suggests that many of the low momentum low quality tracks are not true tracks.	76
4.5	Graph of the mass spectrum of the combinatoric background estimate. This estimate is created by combining two muon tracks from separate events where no dimuon was found and doing vertex reconstruction on them. The suggested cut strongly reduces the background near 5 to 6 GeV.	77
4.6	This graph shows the p_T distribution in data for one of the high x_T bins. Unlike the lower x_T bins, the p_T distribution is mostly flat instead of rapidly falling.	77
4.7	This graph is the same x_T range as 4.6, but with the distribution from the Monte Carlo instead of data. The yield falls rapidly with p_T above a p_T of 2 GeV compared to the data distribution.	78
4.8	A mass fit of J/Ψ , Ψ' , Drell-Yan, and background spectrums. The dark blue curve is the total of the fits. The fits don't quite match the data between 4.2 and 5 GeV. Cutting at 5 GeV like the initial suggestion cuts too much data, I use a 4.2 GeV cut. The Drell-Yan curve comes from GMC which depends partially on the anti quark distributions which we are measuring, so some slight discrepancy between that and data does not bother me.	78

4.9	There is a very large hump in rate dependence at lower intensity when the pedestal is neglected. This is a graph for dump dimuons, since the statistics are better and shows the shape more clearly. The rate dependence is different for target dimuons but the idea here is to show the pedestal dependence.	81
4.10	A rate dependence plot with the pedestal set to 37, fairly close to the correct value. When put next to a plot with a pedestal of zero the small hump suggests the pedestal is still a little too low, but since there are many contributions to the rate dependence we can't make such an assumption.	81
4.11	The pedestal set to 51, a value that is too high.	82
4.12	The distribution of RF+00 values when there is no beam.	82
4.13	The pedestal jumps suddenly in the middle of roadset 62, but otherwise doesn't drift.	83
4.14	Example of a fit of kTrackerEfficiency data to exponential decay.	88
4.15	Fitting the strength of the rate dependence as a function of x_T	89
4.16	The dependence of the kTracker efficiency on chamber intensity, with dependence on trigger intensity removed.	90
4.17	The dependence of the kTracker efficiency on trigger intensity, with dependence on chamber intensity removed.	91
4.18	The rate dependence of empty flask events. It is strongly rate dependent but also does not go to zero at zero intensity.	92
4.19	A fit of the natural log of the ratio of empty flask events to liquid target events, corrected for the number of protons on each target.	93
4.20	The rate dependence of empty flask events when plotted against trigger intensity instead of chamber intensity. It is relatively flat.	94
4.21	The remaining rate dependence after the kTracker efficiency and the empty flask corrections. It is still not very flat.	95
4.22	The natural log of the ratio of LD2 to LH2 as a function of chamber intensity. It is fit with a linear fit.	96
4.23	The natural log of the ratio of LD2 to LH2 as a function of chamber intensity. It is fit with a quadratic fit.	96
4.24	The natural log of the ratio of LD2 to LH2 as a function of chamber intensity. It is fit with a quadratic fit that is missing the linear term.	97
4.25	The natural log of the ratio of LD2 to LH2 as a function of trigger intensity. It is fit with a quadratic fit that is missing the linear term. The dependence is not as strong as the chamber dependence.	98
4.26	The natural log of the ratio of LD2 to LH2 as a function of trigger intensity. The points have been weighted based on a fit to the trigger intensity. It seems flat within the uncertainties.	98
4.27	The natural log of the ratio of LD2 to LH2 as a function of chamber intensity. The points have been weighted based on a fit to the chamber intensity. It seems flat within the uncertainties.	99
4.28	The rate dependence of the low x_T data after the remaining rate correction has been applied. It looks reasonably flat.	99
4.29	The rate dependence of the high x_T data after the remaining rate correction has been applied. It looks reasonably flat.	100
4.30	Plot of the X_T distribution for all three roadsets. The areas under the curves have been normalized to the same value.	107
4.31	Plot of the X_B distribution for all three roadsets. The areas under the curves have been normalized to the same value.	108
4.32	Plot of the X_F distribution for all three roadsets. The areas under the curves have been normalized to the same value.	108
4.33	Plot of the mass distribution for all three roadsets. The areas under the curves have been normalized to the same value.	109
4.34	Plot of the P_T distribution for all three roadsets. The areas under the curves have been normalized to the same value.	109

5.1	A graph of $\ln\left(\frac{\sigma_{pd}}{2\sigma_{pp}}\right)$ as a function of x_T	116
5.2	A graph of $\ln\left(\frac{\bar{d}}{\bar{u}}\right)$ as a function of x	120
5.3	A graph of $\ln\left(\frac{\bar{d}}{\bar{u}}\right)$ as a function of x , with comparison to two recent nlo PDF parametrizations. It is likely that these parametrizations above $x = 0.25$ will change with the publication of SeaQuest data.	121

List of Tables

1.1	A list of relevant variables in DIS.	5
1.2	A list of relevant variables in the Drell-Yan process used in the SeaQuest experiment.	7
2.1	A table of important dates for this data analysis.	23
2.2	List of target identifiers	28
2.3	List of target contamination for runID ranges	30
2.4	List of target contamination	30
2.5	List of target properties. For the deuterium for a given roadset, note that the contamination is not necessarily constant, and these properties would not be constant. These are the properties for the average contamination.	31
2.6	More target properties. For the deuterium for a given roadset, note that the contamination is not necessarily constant, and these properties would not be constant. These are the properties for the average contamination.	31
2.7	Hodoscope properties during run 2.	37
2.8	Hodoscope positions during run 3.	37
2.9	Drift chamber properties.	39
2.10	Drift chamber properties.	41
2.11	A list of the level 2 trigger logic conditions for the FPGA triggers. They are sometimes called MATRIX 1, MATRIX 2, etc. In the half column, T stands for a track in the top half and B stands for a track in the bottom half. TB means there needs to be one track from each half.	44
2.12	A list of all the occupancy cuts that an event has to pass in order to be eligible for tracking.	48
3.1	Table of GMC commands.	59
4.1	List of approximation formulas for Bjorken x to quadratic terms in parton p_{\perp} . Do note that k_{\parallel} and j_{\parallel} have opposite signs.	68
4.2	List of Spill Quality cuts	70
4.3	List of bad spill ranges. The problems with the middle of roadset 67 have been solved and will not be excluded from future analysis.	71
4.4	List of number of spills at different stages in the cutting process. All is number of spills in the Spill table outside the ranges in table 4.3. Complete is the number of spills that have entries in all tables, and both EOS and BOS entries in Scaler. Liquid or Empty Flask is the result of requiring that the spill be on LH2, LD2, or the empty flask. Valid is the number of spills left after applying all data quality cuts.	72
4.5	List of event level cuts.	73
4.6	Uncut is all reconstructed dimuons from valid spills and relevant targets. Valid is the number of those dimuons in the x_T range that pass all of the quality cuts. Target also requires that the dimuon origin is from the target. Drell-Yan also includes the mass cut to cut out the Ψ peaks, but does not include the target cut. T and DY includes both the target and mass cut. The last field includes all of these cuts and the intensity cut as well. The intensity cut removes fewer dimuons in later roadsets as the beam quality has improved.	79
4.7	The weights associated with each RF bucket.	85

4.8	The fit parameters for the LD2 and LH2 targets and the empty flask. The empty flask fit parameters were extrapolated from the LH2 and LD2 parameters.	89
4.9	Table of parameters for empty flask corrections.	92
4.10	A very simple example of a data set C, arbitrarily split into data sets A and B. Both X and Y follow Poisson distributions.	102
4.11	Table 4.10 with more fields.	102
4.12	Like table 4.11, but for a logarithmic study.	103
4.13	Corrected cross section ratio values for the E866 high mass setting. Ratio and Ratio Stat are the traditional cross section ratio and their uncertainties. Log is $\ln(\sigma_{pd}/2\sigma_{pp})$. Log Stat is the uncertainty on $\ln(\sigma_{pd}/2\sigma_{pp})$. Ln Weight is the weight used when combining separate data sets using the log method.	104
4.14	The number of live protons on each target.	105
4.15	Models comparing the cross section of deuterium to what it would be if the nucleons were free.	113
5.1	This table lists the average kinematics for reconstructed dimuons from the LH2 target. The dimuons were weighted with the rate dependence weights.	115
5.2	This table lists the average kinematics for reconstructed dimuons from the LD2 target. The dimuons were weighted with the rate dependence weights.	116
5.3	This table lists how many dimuons were reconstructed from the LH2 target for each bin, and the total weight of all the dimuons at each step.	116
5.4	This table lists how many dimuons were reconstructed from the LD2 target for each bin, and the total weight of all the dimuons at each step.	117
5.5	$\ln(\frac{\sigma_{pd}}{2\sigma_{pp}})$ and its uncertainties for each bin.	117
5.6	A breakdown of the upper uncertainties on $\ln(\frac{\sigma_{pd}}{2\sigma_{pp}})$. Efficiency is the systematic uncertainty from the kTracker efficiency corrections. Empty is the uncertainty from the empty flask corrections. Remaining rate is the uncertainty from the corrections for the remaining rate dependence. Contamination is the uncertainty for the target contamination correction.	117
5.7	A breakdown of the lower uncertainties on $\ln(\frac{\sigma_{pd}}{2\sigma_{pp}})$. The fields are the same as in table 5.6.	118
5.8	$\ln(\frac{\bar{d}}{\bar{u}})$ and its uncertainties, binned in x.	119
5.9	The breakdown of upper systematic uncertainties on $\ln(\frac{\bar{d}}{\bar{u}})$. Propagated is the systematic uncertainty propagated from the cross section ratio. PDF uncertainty is the uncertainty within the PDF set. PDF high x is the uncertainty from the unknown value of $\ln(\bar{d}/\bar{u})$ outside of our measuring range. PDF group is the systematic uncertainty from the choice of PDF set, i.e. we chose MMHT2014 instead of CT14. Nuclear correction is the systematic uncertainty from nuclear effects in deuterium.	119
5.10	The breakdown of lower systematic uncertainties on $\ln(\frac{\bar{d}}{\bar{u}})$. The fields are the same as in table 5.9.	120

Chapter 1

Background

The purpose of SeaQuest is to measure the distribution of antiquarks inside the proton. Therefore, a basic understanding of proton structure is necessary in order to understand what we are trying to measure. The history of several other experiments are also presented to give context to our own results and the motivations for this experiment. In this thesis, I will use "God given" units, where $c = 1$ and $\hbar = 1$.

1.1 Proton Structure

In the early days of particle physics experiments, there seemed to be no end to the number of hadrons that existed. Then Zweig and Gell-Mann independently suggested that the hadrons were made up of constituent quarks with $1/2$ spin that explained the properties of the hadrons[1][2]. At the time of the original papers there were three suggested quarks: up, down, and strange (u, d, s). Later on three more quarks were discovered: charm, bottom, and top (c, b, t). These six varieties are called flavors. The up, charm, and top quarks each have an electric charge of $\frac{2}{3}e$ and the down, strange, and bottom quarks have a charge of $-\frac{1}{3}e$. Each quark has an anti-quark of opposite charge. Mesons are bound states of a quark and an anti-quark, while baryons are bound states of three quarks (or three anti-quarks). When the quark model was first introduced, it wasn't known if quarks existed as real particles or if they were purely mathematical entities.

The concept of color was soon suggested by Greenberg[3] in order to explain the existence of the Δ^{++} particle which was composed of three seemingly identical up quarks. All quarks have color charge, which is a property that has nothing to do with visual color. A quark can have a color charge of red, blue, or green (r, b, g), while anti-quarks can have anti-red, anti-blue, or anti-green ($\bar{r}, \bar{b}, \bar{g}$)[4][5]. A particle is white or colorless if it has equal amounts of red, blue, and green, i.e. $rgb, \bar{r}\bar{g}\bar{b}, r\bar{r}$, etc. The quarks are bound together by a strong force which is carried by gluons. The gluons come in eight varieties and simultaneously carry both a color and anti-color charge, i.e. a $r\bar{b}$ gluon. They are also electrically neutral.

In 1969 the parton model was developed[6] which represented the proton as consisting of fundamental point like constituents. This model was supported by deep inelastic scattering (DIS) experiments at Stanford

Linear Accelerator Center (SLAC)[7][8] which found that the scattering cross sections matched the profile of scattering off of a proton composed of multiple point like particles. The partons from this model and the quarks from the quark model turned out to be the same entities, and quarks were no longer thought of as purely mathematical entities.

After the parton model came the concept of asymptotic freedom [9] [10] which says that at high energy or small distances the proton can be modeled as a group of free non-interacting particles. Equation 1.1 gives the strength of α_s , the coupling constant of the strong force, as a function of the energy scale squared[5]. n_f is the number of quark flavors and Λ is an experimentally determined constant around 200 GeV[4]. The flipside of equation 1.1 is that the strong force becomes more powerful at large distances. No quark can exist on its own outside a hadron and all hadrons must be colorless. The energy involved in attempting to free a quark from its hadron will create more quark antiquark pairs from the vacuum which combine with the quarks and antiquarks already present to form new hadrons in a process called hadronization, leaving no free quarks.

$$\alpha_s(Q^2) = \frac{12\pi}{(33-2n_f)\ln(Q^2/\Lambda^2)} \quad (1.1)$$

The three quarks from the quark model that make up the proton, uud, are not the only three partons in the proton. The uud that give the proton its properties are called the valence quarks, but there are many $q\bar{q}$ pairs within the proton called sea quarks. The gluons are also partons.

The distributions of partons in the proton are typically mapped out according to a variable called Bjorken x , which I will simply refer to as x . x is the ratio of the momentum of the parton to the momentum of the proton it is inside, in a frame where the proton has infinite momentum. At high enough energies the structure functions that describe the structure of the proton in DIS are only a function of x , this is known as Bjorken scaling[11]. The number density of partons inside the proton as a function of x are called parton distribution functions (PDFs). Due to isospin symmetry, which says that strong interactions are symmetric under the transformation $u \leftrightarrow d$ if one ignores the very slight light quark mass differences, PDFs for the proton can be applied to the neutron. $u(x)$ and $\bar{u}(x)$ for the proton become $d(x)$ and $\bar{d}(x)$ for the neutron and vice versa. PDFs exist for some other particles, such as pions, but generally when someone says PDFs they mean the proton PDFs. An example of some PDFs are graphed in figure 1.1. PDFs are calculated by groups such as the CTEQ collaboration by fitting the data from dozens of experiments.

Bjorken scaling is not exact, the PDFs also depend on Q^2 , although with a weaker dependence. Quarks are not truly non-interacting in the proton, and with higher resolution it is possible to see more of the gluon emission, gluon absorption, and gluon splitting into $q\bar{q}$ pairs. That means at higher Q^2 we will see

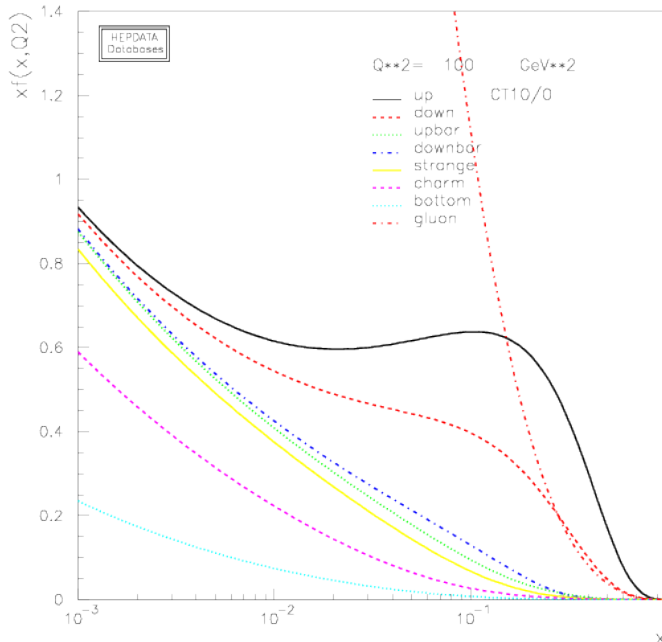


Figure 1.1: CT10 PDFs from the CTEQ collaboration[12][13].

more partons at low x and fewer at high x . Fortunately, if one knows the PDFs at one value of Q^2 it can be known at any value of Q^2 according to equation 1.2, the DGLAP or Dokshitzer-Gribov-Lipatov-Altarelli-Parisi evolution equation[14]. A quark with momentum fraction x can come from a quark with larger momentum fraction y that radiated a gluon, which is represented by the function $P_{qq}(z)$.

$$\frac{d}{d \ln Q^2} q(x, Q^2) = \frac{\alpha_s}{2\pi} \int_x^1 \frac{dy}{y} q(y, Q^2) P_{qq}\left(\frac{x}{y}\right) \quad (1.2)$$

$$P_{qq}(z) = \frac{4}{3} \frac{1+z^2}{1-z} \quad (1.3)$$

1.2 Deep Inelastic Scattering

Deep Inelastic Scattering is the scattering of a high energy lepton off of a nucleus by exchanging a virtual gauge boson, as shown in the leading order Feynman diagram in figure 1.2. A list of relevant variables is in table 1.1. The high energy of the lepton allows it to resolve distances much smaller than that of a proton, allowing it to probe "deep" and see a single parton. The struck parton receives enough energy to break up the proton and cause hadronization, but DIS experiments are not concerned with the hadron end products.

DIS experiments calculate q from the change in lepton momentum, which is in turn used to calculate x using equation 1.4. At high enough Q^2 it is possible to approximate the DIS cross section as equation 1.5, assuming the gauge boson exchanged is a virtual photon. By measuring the cross section as a function of x , it is possible to get a measure of the parton distribution functions. While DIS has been very useful for exploring PDFs, the basic electron/muon emits a virtual photon DIS is not sensitive to the difference between a quark and its antiquark, as seen in equations 1.5, 1.6, and 1.7. Semi-inclusive DIS (SIDIS), which measures some of the hadronization end products, can give us some insight into the antiquark PDFs. Neutrino DIS can explore such things with the emission of W bosons instead of photons but the details of other forms of DIS are outside the scope of this paper.

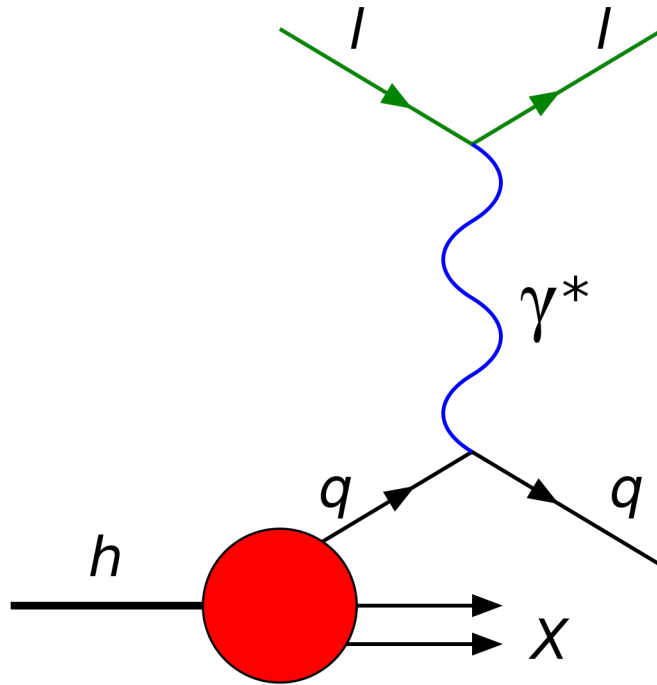


Figure 1.2: Feynman diagram for deep inelastic scattering. Time flows from left to right. The particle exchanged does not have to be a photon, it can be any electroweak gauge boson.

$$x = \frac{Q^2}{2P \cdot q} \quad (1.4)$$

$$\frac{d\sigma}{dE' d\Omega} = \frac{\alpha^2}{4E^2 \sin^4(\theta/2)} \left(\frac{F_2(x)}{v} \cos^2(\theta/2) + \frac{2F_1(x)}{M} \sin^2(\theta/2) \right) \quad (1.5)$$

Variable	Description
k_i, k_f	Initial and final lepton 4-momentum
q	Gauge Boson 4-momentum
P	Proton 4-momentum
E	Initial energy of the lepton
E'	Final energy of the lepton
v	$E - E'$, energy of the gauge boson
M	Proton mass
θ	Scattering angle of the lepton
Q^2	$-q^2$, energy scale of the process
x	Bjorken scaling variable
α	Fine structure constant
$q_i(x)$	PDF of quark flavor i
e_i	Electric charge of quark flavor i, as a fraction of e
Σ_i	Means sum over all quark flavors

Table 1.1: A list of relevant variables in DIS.

$$F_1(x) = \frac{1}{2} \Sigma_i e_i^2 (q_i(x) + \bar{q}_i(x)) \quad (1.6)$$

$$F_2(x) = \Sigma_i e_i^2 x (q_i(x) + \bar{q}_i(x)) \quad (1.7)$$

1.3 Drell-Yan Process

The Drell-Yan process[15] is where a quark antiquark pair annihilate into a virtual photon (or Z-boson) that then decays into a lepton antilepton pair, as shown in figure 1.3. A list of the relevant variables for the Drell-Yan process is shown in table 1.2. The leading order Drell-Yan cross section can be quickly derived from the simple $e^+e^- \rightarrow \mu^+\mu^-$ leading order cross section, shown in equation 1.8[5].

$$\sigma(e^+e^- \rightarrow \mu^+\mu^-) = \frac{4\pi\alpha^2}{3s} \quad (1.8)$$

The first change that is necessary is that the mass of the virtual photon of the Drell-Yan process is not the same as s of the proton nucleon collision, so s becomes M^2 . Second, the structure of the proton has to be taken into account, so the total cross section is a double integral over all the partons in the beam proton and all the partons in the target nucleon. One must take into account that a quark can only annihilate with a matching flavor of anti-quark, and that the likelihood of this annihilation is proportional to e_i^2 . Third, a factor of 1/3 must be added as the annihilation has to match colorwise, i.e. red can only annihilate with antired. These changes result in equations 1.9 and 1.10.

$$\sigma_{DY} = \frac{4\pi\alpha^2}{9} \int_0^1 \int_0^1 \Sigma_i \frac{e_i^2}{M^2} (q_i(x_B)\bar{q}_i(x_T) + \bar{q}_i(x_B)q_i(x_T)) dx_B dx_T \quad (1.9)$$

$$\frac{d\sigma_{DY}}{dx_B dx_T} = \frac{4\pi\alpha^2}{9M^2} \Sigma_i e_i^2 (q_i(x_B)\bar{q}_i(x_T) + \bar{q}_i(x_B)q_i(x_T)) \quad (1.10)$$

Looking at the equation for the Drell-Yan cross section we can see that unlike basic DIS the term for a quark from the target is not symmetric with the term for an antiquark from the target. If one uses an antiproton beam on a proton target the cross section changes to equation 1.11, giving yet another avenue of attack for distinguishing between quark and antiquark PDFs.

$$\frac{d\sigma_{DY}}{dx_B dx_T} = \frac{4\pi\alpha^2}{9M^2} \Sigma_i e_i^2 (q_i(x_B)q_i(x_T) + \bar{q}_i(x_B)\bar{q}_i(x_T)) \quad (1.11)$$

If one wants to simulate Drell-Yan reactions with Monte Carlo, the angular differential cross section (or at least the angular dependence of $1 + \cos^2(\theta)$) in equation 1.12 is also needed.

$$\frac{\sigma_{DY}}{d\Omega} |_{cm} = \frac{\alpha^2}{4} (1 + \cos^2(\theta)) \int_0^1 \int_0^1 \Sigma_i \frac{e_i^2}{M^2} (q_i(x_B)\bar{q}_i(x_T) + \bar{q}_i(x_B)q_i(x_T)) dx_B dx_T \quad (1.12)$$

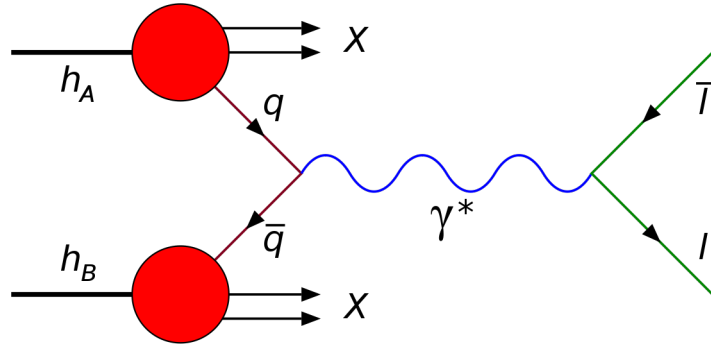


Figure 1.3: Feynman diagram for the Drell-Yan process. Time flows from left to right. The particle exchanged could also be a Z-boson, but at SeaQuest our energies are too low.

Several of the measured variables in Drell-Yan are related to one another. Out of the four variables, M , x_F , x_B , and x_T , if you know two of them the other two can be calculated via equations 1.13 through 1.16. However, these are only approximate, and a more in depth calculation of x_B and x_T from experimentally measured variables is found in the analysis chapter. Still, using these approximations, it is possible to transform equation 1.10 into equation 1.17 by using a Jacobian to do a change of variables.

Variable	Description
k	Initial 4-momentum of the quark from the beam proton
j	Initial 4-momentum of the quark from the target nucleon
q	Virtual photon 4-momentum
s	Invariant mass squared of the proton nucleon system, c.m. frame
P_1	Beam proton 4-momentum
P_2	Target nucleon 4-momentum
M	Invariant mass of the $\mu + \mu^-$ pair
Q^2	$-q^2$, energy scale of the process
x_B	Bjorken scaling variable, beam parton, sometimes called x_1
x_T	Bjorken scaling variable, target parton, sometimes called x_2
x_B	Feynman x, longitudinal momentum of the virtual photon, divided by the maximum it could have
y	Rapidity, $\frac{1}{2} \ln\left(\frac{E+p_{\parallel}}{E-p_{\parallel}}\right)$
τ	M^2/s
θ	Angle of μ^- with respect to the z-axis in the Collins Soper frame
ϕ	Azimuthal angle of μ^- measured with respect to \hat{q}_T in the Collins Soper frame
α	Fine structure constant
$q_i(x)$	PDF of quark flavor i
e_i	Electric charge of quark flavor i, as a fraction of e
Σ_i	Means sum over all quark flavors

Table 1.2: A list of relevant variables in the Drell-Yan process used in the SeaQuest experiment.

$$M \approx \sqrt{s x_B x_T} \quad (1.13)$$

$$x_F \approx x_B - x_T \quad (1.14)$$

$$x_B \approx \frac{x_F + \sqrt{x_F^2 + 4M^2/s}}{2} \quad (1.15)$$

$$x_T \approx \frac{-x_F + \sqrt{x_F^2 + 4M^2/s}}{2} \quad (1.16)$$

$$\frac{d\sigma_{DY}}{dM dx_F} = \frac{8\pi\alpha^2}{9M^3} \frac{x_B x_T}{x_B + x_T} \Sigma_i e_i^2 (q_i(x_B) \bar{q}_i(x_T) + \bar{q}_i(x_B) q_i(x_T)) \quad (1.17)$$

After Drell and Yan published their paper, experimental data on the differential cross section of the Drell Yan process showed a few surprising results[16]. First, there were dileptons with transverse momentum much higher than the expected 300 to 500 MeV[17][18]. Second, while the shape of the differential cross section was close to what was expected, the total cross section was off by approximately a factor of 2. This

factor is called the K factor, and the next to leading order (NLO) cross section terms are responsible for this K factor[19]. The significant contribution of NLO terms are also responsible for the higher than expected observed p_T . A plot of p_T in Drell-Yan experiments is shown in figure 1.4.

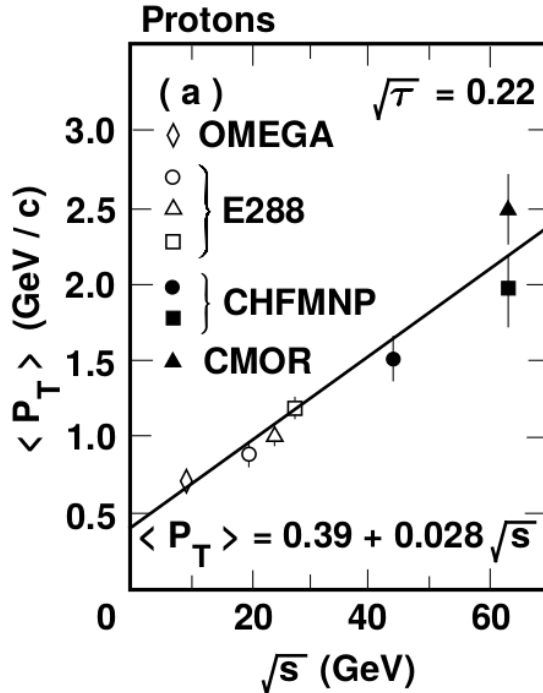


Figure 1.4: A graph of the average p_T versus \sqrt{s} [16].

When the Drell-Yan process has high p_T , it is no longer reliable to calculate θ in equation 1.12 as the angle between the beam axis and $\vec{\mu}^-$. Because of this, Collins and Soper came up with the Collins Soper frame[20]. This frame is the center of mass frame of the dilepton pair, with the z axis chosen to bifurcate the angle between \vec{P}_1 and $-\vec{P}_2$. θ is measured as the angle between this axis and $\vec{\mu}^-$. Defining a vector \hat{q}_T as the unit vector in the (\vec{P}_1, \vec{P}_2) plane orthogonal to the z-axis, the azimuthal angle ϕ for μ^- is defined with respect to \hat{q}_T . \hat{q}_T is sometimes the definition of the x-axis but Collins and Soper preferred not to define an x or y-axis. A more intuitive way to calculate ϕ is as the angle between the dilepton plane and the dihadron plane. A visual diagram of this frame is displayed in figure 1.5.

1.4 Gottfried Sum Rule

The naive expectation among most physicists at the time was that $\bar{u}(x) = \bar{d}(x)$. One expression of this expectation was the Gottfried sum rule[22], which was that the Gottfried Sum, S_G , is equal to 1/3. The Gottfried sum is shown in equation 1.18 and is a function of the difference between proton and neutron

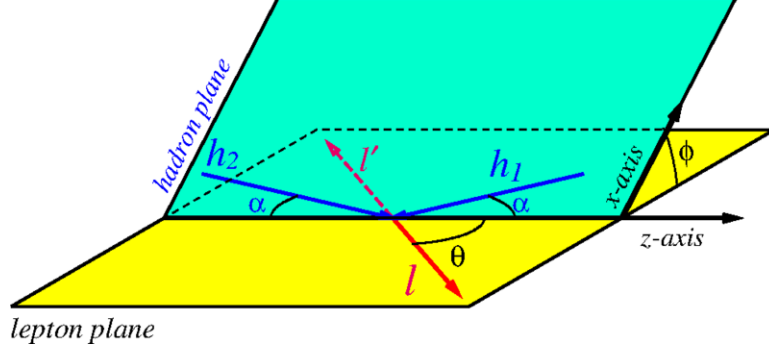


Figure 1.5: A diagram of the Collins Soper plane[21].

structure functions.

$$S_G = \int_0^1 (F_2^p - F_2^n) \frac{dx}{x} \quad (1.18)$$

Subbing in from equation 1.7, we get equation 1.19.

$$S_G = \int_0^1 \Sigma_i e_i^2 (q_i^p + \bar{q}_i^p - q_i^n - \bar{q}_i^n) dx \quad (1.19)$$

The strange and heavier quarks are expected to have the same distributions for protons and neutrons, so those contributions cancel out. Isospin symmetry gives us $u^n(x) = d^p(x)$, $d^n(x) = u^p(x)$, $\bar{u}^n(x) = \bar{d}^p(x)$, and $\bar{d}^n(x) = \bar{u}^p(x)$. This leads to equation 1.20.

$$S_G = \int_0^1 \frac{1}{3} (u(x) + \bar{u}(x) - d(x) - \bar{d}(x)) dx \quad (1.20)$$

Adding a $2/3(\bar{u}(x) - \bar{u}(x))$ and a similar term for $\bar{d}(x)$ gets us equation 1.21.

$$S_G = \frac{1}{3} \int_0^1 (u(x) - \bar{u}(x)) dx - \frac{1}{3} \int_0^1 (d(x) - \bar{d}(x)) dx + \frac{2}{3} \int_0^1 (\bar{u}(x) - \bar{d}(x)) dx \quad (1.21)$$

$\int_0^1 (u(x) - \bar{u}(x)) dx = 2$ and $\int_0^1 (d(x) - \bar{d}(x)) dx = 1$ as the proton has valence content of two u quarks and one d quark, which gives us equation 1.22.

$$S_G = \frac{1}{3} + \frac{2}{3} \int_0^1 (\bar{u}(x) - \bar{d}(x)) dx \quad (1.22)$$

If $\bar{d}(x) = \bar{u}(x)$, then $S_G = 1/3$.

1.5 Sea Flavor Asymmetry in Past Experiments

The purpose of the SeaQuest experiment is to study the asymmetry in the parton sea, $\bar{d}(x) \neq \bar{u}(x)$. The study of this asymmetry started with the New Muon Collaboration (NMC) experiments who first discovered this and continues today with SeaQuest.

1.5.1 New Muon Collaboration

The NMC were not the first experiment to measure the Gottfried Sum, but the others had large uncertainties and the NMC were the first to find out that $S_G \neq \frac{1}{3}$ [23]. They found a value of $S_G = 0.24 \pm 0.016$, unambiguously below the $\frac{1}{3}$ of the expected value. They used two muon beams of energies 90 and 280 GeV to do DIS on hydrogen and deuterium targets. The definition of F_2^d in the NMC papers is sometimes $F_2^p + F_2^n$ and sometimes $(F_2^p + F_2^n)/2$, I will consistently use the former definition. First, the NMC calculated the ratio $\frac{\sigma_d}{\sigma_p}$ from the ratio of events on their hydrogen and deuterium targets[24]. Then they calculated the ratio of the structure functions via equations 1.23 and 1.24

$$\frac{F_2^d}{F_2^p} = \frac{\sigma_d}{\sigma_p} \quad (1.23)$$

$$\frac{F_2^n}{F_2^p} = \frac{F_2^d}{F_2^p} - 1 \quad (1.24)$$

After the ratio $\frac{F_2^n}{F_2^p}$ was calculated, the NMC then calculated F_2^d from a fit to data from several DIS experiments. With these values, they then calculated $F_2^p - F_2^n$ via equation 1.25.

$$F_2^p - F_2^n = F_2^d \frac{1 - \frac{F_2^n}{F_2^p}}{1 + \frac{F_2^n}{F_2^p}} \quad (1.25)$$

This calculation was done separately for many different bins in the x range 0.004 to 0.8. The NMC plotted this data on a graph in figure 1.6 and extrapolated the integral of $\int_x^1 (F_2^p - F_2^n) \frac{dx}{x}$ data to $x = 0$ to calculate S_G .

1.5.2 NA51

NA51 was designed to test between two hypotheses to explain the S_G result from NMC[25]. The first hypothesis was that the contents of the proton at $x < 0.004$ make a large contribution to S_G and therefore the extrapolation of NMC from $x = 0.004$ to 0 was not valid. The second hypothesis was that the quark

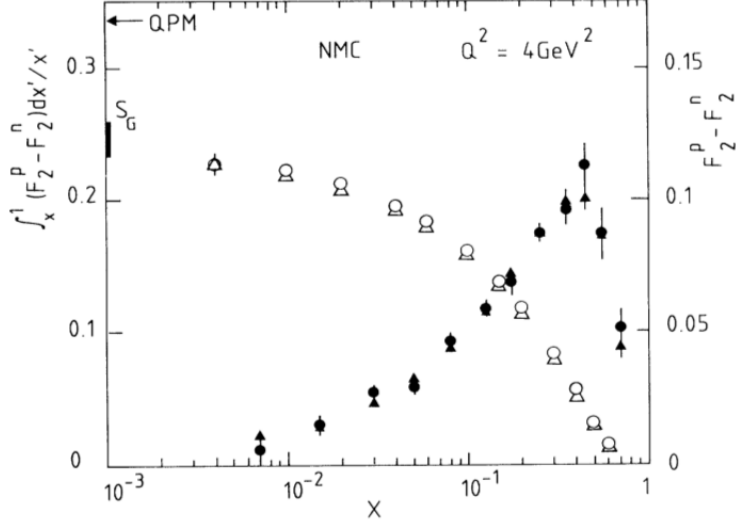


Figure 1.6: Data from NMC. The black points use the scale to the right and are $F_2^p - F_2^n$ for that bin in x . The white points use the scale to the left and are the integral of $F_2^p - F_2^n$ from that value of x to 1. The white points are extrapolated to reach a value of S_G , which is significantly below the predicted value of $1/3$ (Labelled with QPM).

sea was asymmetric, $\bar{d}(x) \neq \bar{u}(x)$. NA51 used a 450 GeV proton beam on hydrogen and deuterium targets and compared their Drell-Yan cross sections. They assumed shadowing, which is an effect that modifies the PDFs when the nucleons are inside of a nucleus, was negligible and that $\sigma_{pd} = \sigma_{pp} + \sigma_{pn}$. NA51 defined a quantity A_{DY} in equation 1.26 and measured it as in equation 1.27.

$$A_{DY} = \frac{\sigma^{pp} - \sigma^{pn}}{\sigma^{pp} + \sigma^{pn}} \quad (1.26)$$

$$A_{DY} = 2 \frac{\sigma_{pp}}{\sigma_{pd}} - 1 \quad (1.27)$$

In the kinematics of NA51, $y \approx 0$ and $x_1 \approx x_2$. NA51 treated the contributions of interactions between two sea partons as insignificant, which led to the proton and neutron cross sections being proportional to equations 1.28 and 1.29.

$$\sigma_{pp} \propto 8u_v(x)\bar{u}(x) + 2d_v(x)\bar{d}(x) \quad (1.28)$$

$$\sigma_{pn} \propto 5u_v(x)\bar{d}(x) + 5d_v(x)\bar{u}(x) \quad (1.29)$$

All of the constants in front of the parton distributions cancel out and when we sub equations 1.28 and

1.29 into equation 1.26 we end up with equation 1.30.

$$A_{DY} = \frac{(4u_v - d_v)(\bar{u} - \bar{d}) + (u_v - d_v)(4\bar{u} - \bar{d})}{(4u_v + d_v)(\bar{u} + \bar{d}) + (u_v + d_v)(4\bar{u} + \bar{d})} \quad (1.30)$$

Defining the ratio of valence quarks as $\lambda_v = u_v/d_v$ and the ratio of sea quarks as $\lambda_s = \bar{u}/\bar{d}$ we end up with equation 1.31.

$$A_{DY} = \frac{(4\lambda_v - 1)(\lambda_s - 1) + (\lambda_v - 1)(4\lambda_s - 1)}{(4\lambda_v + 1)(\lambda_s + 1) + (\lambda_v + 1)(4\lambda_s + 1)} \quad (1.31)$$

This equation can be solved for λ_s , shown in equation 1.32

$$\lambda_s = \frac{2 - 5\lambda_v - 2A_{DY} - 5A_{DY}\lambda_v}{5 - 8\lambda_v + 5A_{DY} + 8A_{DY}\lambda_v} \quad (1.32)$$

NA51 calculated one value for λ_s at an average value for x or 0.18. They used a value of $\lambda_v(0.18) = 2.2$ taken from an average of several PDFs and measured A_{DY} from their experiment. After calculating corrections for the sea-sea terms they neglected in their approximation, in 1994 they published results showing a value of $\lambda_s = 0.51 \pm 0.04(sta) \pm 0.05(sys)$, which translates into $\bar{d}/\bar{u} = 1.96 \pm 0.15(sta) \pm 0.19(sys)$.

1.5.3 E866/NuSea

The E866 experiment was a fixed target experiment at Fermilab using an 800 GeV proton beam on hydrogen and deuterium targets[26]. It used a spectrometer that favored events where $x_B > x_T$. It is similar to our own experiment, sharing some wire chambers, collaboration members, Monte Carlo code, and a similar design. E866 measured the Drell-Yan cross section ratio σ_{pd}/σ_{pp} and used that to estimate \bar{d}/\bar{u} . In the kinematic region $x_B > x_T$ it is much more likely that the antiquark comes from the target than the beam due to the large ratio of quarks to antiquarks at higher x . The ratio of the Drell-Yan differential cross section for proton-proton and proton-deuterium collisions is in equation 1.33 if one neglects strange and higher mass quarks and also drops the terms where the antiquark comes from the beam.

$$\frac{\sigma_{pd}}{\sigma_{pp}} = 1 + \frac{4u(x_B)\bar{d}(x_T) + d(x_B)\bar{u}(x_T)}{4u(x_B)\bar{u}(x_T) + d(x_B)\bar{d}(x_T)} \quad (1.33)$$

By recognizing that $4u$ is greater than d by a factor of 8 and making an approximation where the d terms in the ratio are omitted, we receive equation 1.34.

$$\frac{\sigma_{pd}}{\sigma_{pp}} = 1 + \frac{\bar{d}(x_T)}{\bar{u}(x_T)} \quad (1.34)$$

This much of an approximation is clearly unfit for calculating real physics results but it shows the sensitivity of the measurement of the cross section ratio to \bar{d}/\bar{u} in forward spectrometer Drell-Yan experiments such as E866 and SeaQuest. NuSea's actual calculation used an iterative process where a prediction for the cross section ratio σ_{pd}/σ_{pp} was calculated based on a hypothetical value for \bar{d}/\bar{u} . This predicted ratio was compared to the measured ratio and \bar{d}/\bar{u} was adjusted accordingly for the next iteration. The quark PDFs and $\bar{d}(x)+\bar{u}(x)$ values were taken from the CTEQ4M PDFs. The iteration converged on a value for $\bar{d}(x)/\bar{u}(x)$ when the predicted and measured cross section ratios matched. In 1998 E866 published results showing a dependence of $\bar{d}(x)/\bar{u}(x)$ on x . A plot of the cross section ratio results are shown in figure 1.7 and the sea flavor asymmetry results are shown in figure 1.8 from the improved measurement results from 2001[27]. An interesting feature of the improved results is the high x point where $\bar{d} < \bar{u}$ with a certainty greater than 1σ .

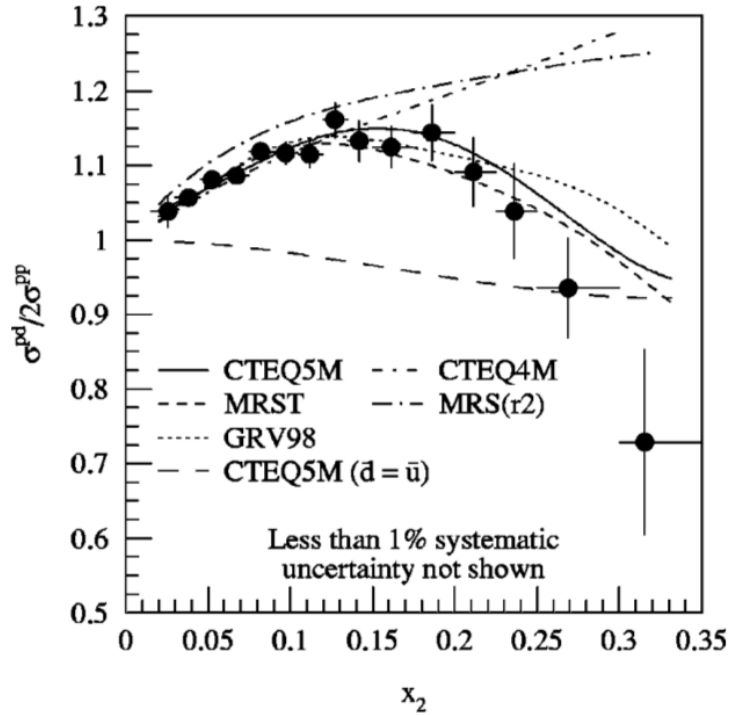


Figure 1.7: The cross section ratio $\sigma_{pd}/2\sigma_{pp}$ results binned in x for E866. Predictions from various PDFs are also shown.

1.6 Motivation

The Drell-Yan process can be used to study the PDFs in a way complementary to DIS experiments. Drell-Yan has sensitivity to sea quarks and can be used to research the antiquark PDFs, especially with a forward spectrometer. The SeaQuest experiment was designed to pick up where E866 left off and research the

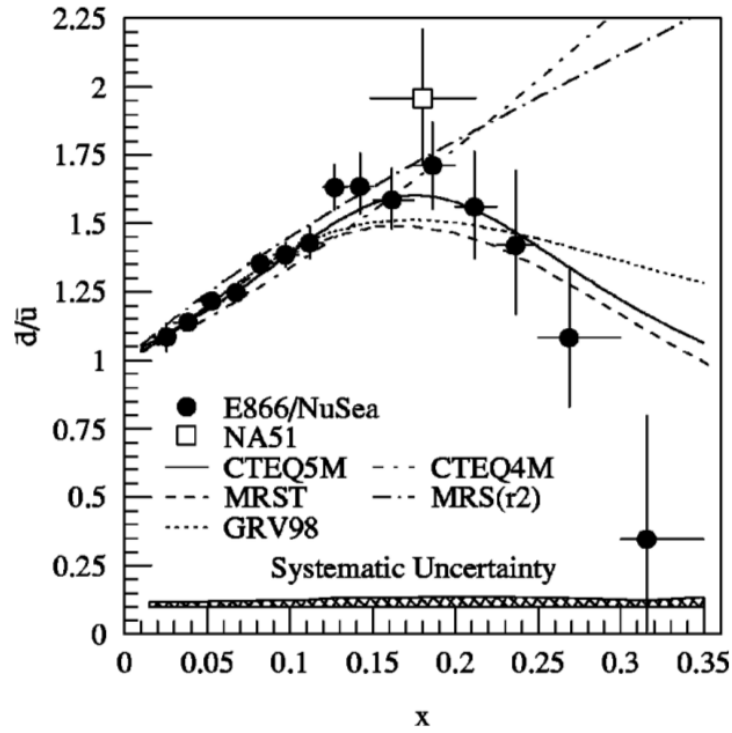


Figure 1.8: \bar{d}/\bar{u} binned as a function of x , from E866. Predictions from various PDFs are also shown. There is a significant difference at high x for PDF sets published before the E866 results in 1998 and those published after the E866 results. The drop below $\bar{d}/\bar{u} = 1$ at higher x was completely unexpected.

$\bar{d}(x)/\bar{u}(x)$ distribution at even higher x [28][29]. The Drell-Yan cross section drops off quickly with higher mass, as shown in figure 1.9 and equation 1.10, and high mass dimuons are high x dimuons. Because of this, some way to improve the statistics of the measurement was needed in order to design an experiment that measured higher x antiquark PDFs than E866. Rewriting equation 1.10 to put the M^2 in terms of s , we can see that the Drell-Yan cross section is inversely proportional to s .

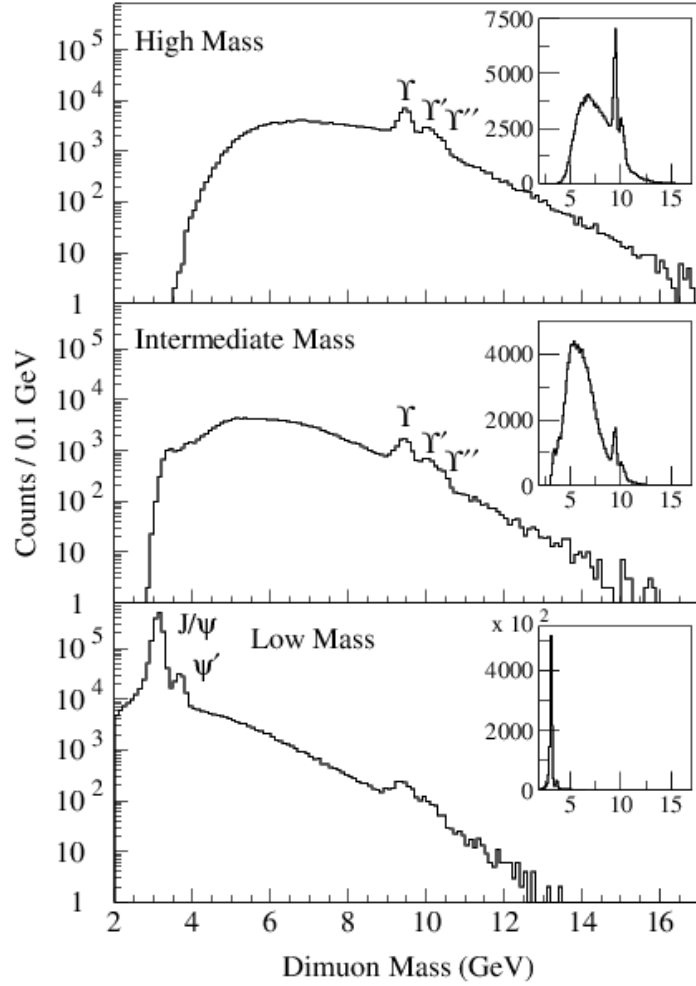


Figure 1.9: The dimuon mass spectrum from E866. Notice the J/Ψ and Ψ' peaks between 3 and 4 GeV. It also drops off quickly with mass[30].

$$\frac{d\sigma_{DY}}{dx_B dx_T} = \frac{4\pi\alpha^2}{9s x_B x_T} \sum_i e_i^2 (q_i(x_B)\bar{q}_i(x_T) + \bar{q}_i(x_B)q_i(x_T)) \quad (1.35)$$

Calculating s shows us it is very close to being proportional to the beam energy.

$$s = m_t * E_{Beam} + m_t^2 + m_b^2 \quad (1.36)$$

SeaQuest uses a beam energy of 120 GeV, which gives about an improvement of 6.7 times more cross section than the 800 GeV beam of E866. Another improvement is that SeaQuest can support higher luminosity. As radiation dosage scales with beam energy SeaQuest can have a higher luminosity without going over radiation safety limits. Background also scales with luminosity, and the main background of E866 was muon singles from J/Ψ decay. As can be seen in figure 1.10, the J/Ψ production cross section rises quickly with \sqrt{s} , so SeaQuest can have a higher luminosity without running into background troubles. \sqrt{s} for a proton-proton reaction is about 38.76 GeV for E866 and 15.06 GeV for SeaQuest. The proposal for SeaQuest estimated a factor of 50 increase in statistics compared to E866, with estimated statistical uncertainties by the end of the experiment estimated in figure 1.11. This high x region is of much interest, as E866 suggests $\bar{d} < \bar{u}$ in that region and no known model predicts this. The results of E866 were interesting but of not enough statistical significance to be compelling, SeaQuest's flagship measurement of \bar{d}/\bar{u} aims to answer the question, "Does \bar{d}/\bar{u} really fall below 1?"

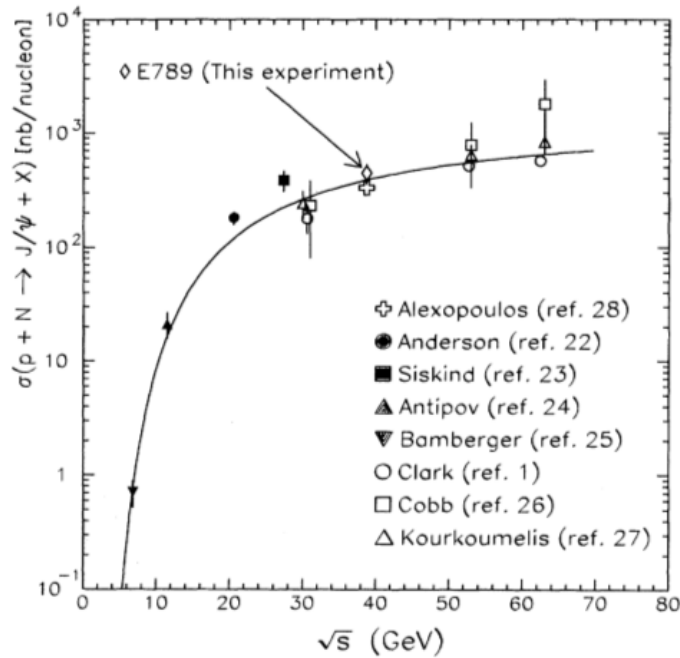


Figure 1.10: The J/Ψ cross section as a function of \sqrt{s} . It grows quickly with higher energies[31].

1.7 Models

One early hypothesis was that Pauli blocking was the cause of the sea flavor asymmetry, as the two valence u quarks blocked \bar{u} more than the valence d quark blocked \bar{d} [32]. However, it has been shown that Pauli

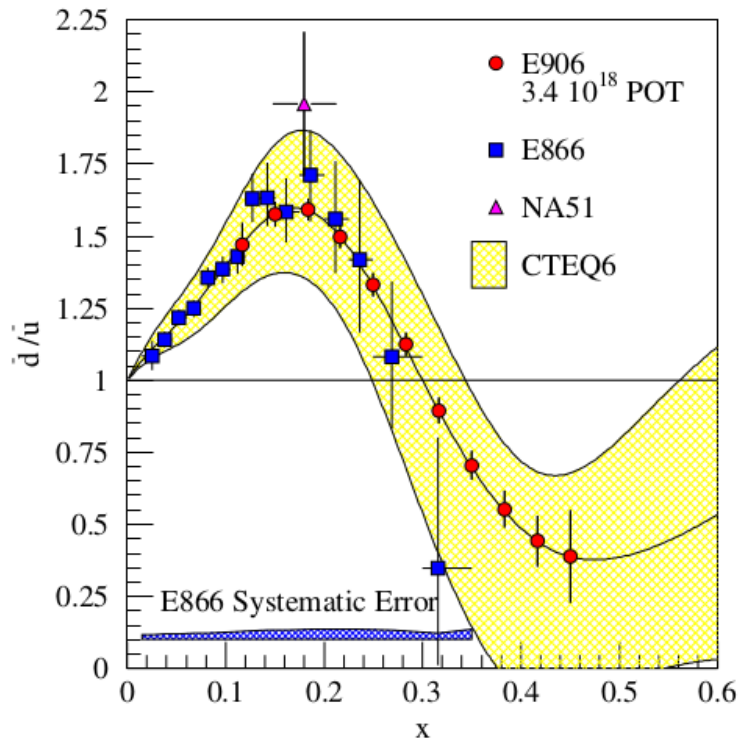


Figure 1.11: Estimated statistical uncertainties for SeaQuest, compared to E866[29]. While we have fallen short of this goal, we have still improved upon the E866 measurement from about $x = 0.15$ to 0.35 and roughly measured the asymmetry at x up to 0.58 .

blocking does not contribute to the excess of \bar{d} [33]. Since then, many models have been proposed to explain the \bar{d}/\bar{u} asymmetry[34]. As stated earlier, none of them predict $\bar{d} < \bar{u}$ at any x . Figures for predictions of the meson cloud model, chiral quark model, chiral quark soliton model, and the statistical model are in figures 1.12, 1.13, 1.14, and 1.15. An explanation of each model is outside the scope of this paper.

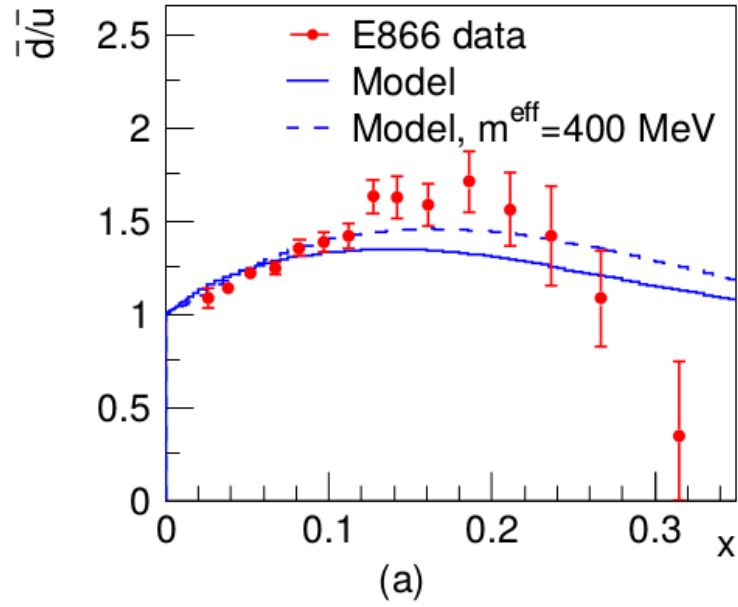


Figure 1.12: Comparison of two similar meson cloud models to E866 data. The dotted line parametrises the pion as having an effective mass of 400 MeV inside the proton. Both approach $\bar{d} = \bar{u}$ at high x [35].

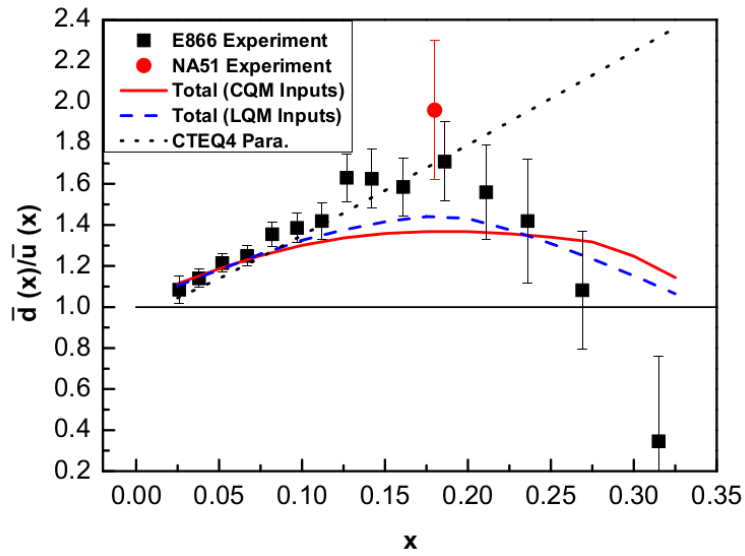


Figure 1.13: E866 data and the NA51 data point plotted with two variants of the Chiral Quark model (red and blue curves). The authors note that they could not get the ratio below 1 in their models[36].

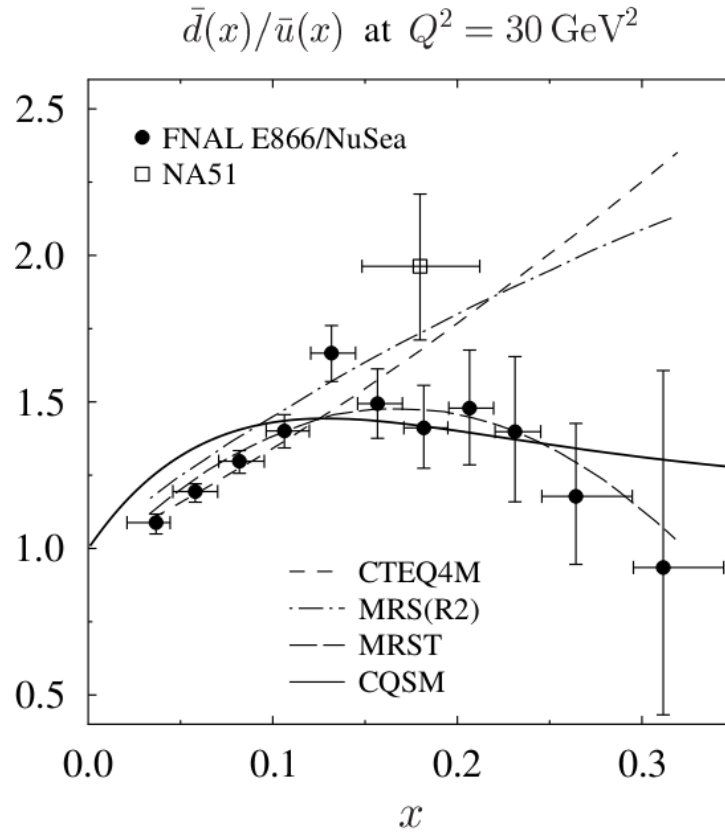


Figure 1.14: A comparison of E866 and NA51 data with a Chiral Quark Soliton model (solid line) and several PDF sets[37]. This uses the early E866 data without a statistically significant $\bar{d} < \bar{u}$.

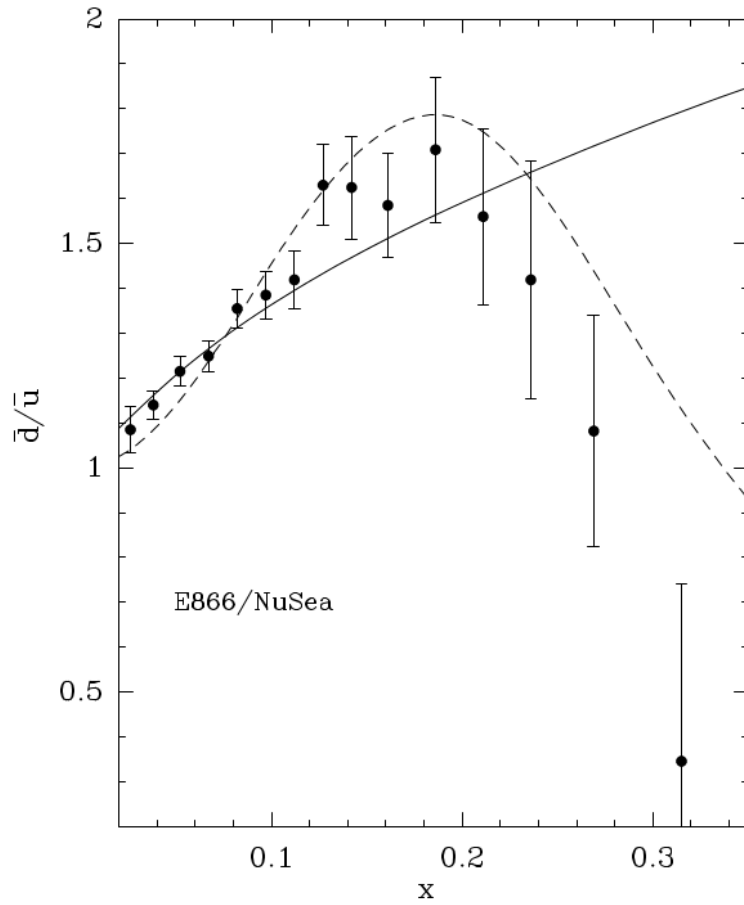


Figure 1.15: A statistical model compared to E866 data. The solid line is the prediction from the statistical model[38]. In this model \bar{d}/\bar{u} keeps increasing.

Chapter 2

Experimental Setup

This chapter is a basic introduction to the spectrometer at SeaQuest. It covers how the measurements used in this analysis were made. It also examines the origins of many of the challenges of this analysis, particularly those related to beam quality and target purity.

SeaQuest is a fixed target experiment that takes place at Fermilab and uses the 120 GeV proton beam from the main injector. A diagram of our spectrometer can be found in figure 2.1. The beam passes by or through detectors placed to monitor the strength of the beam. It then strikes our choice of one of seven targets, producing the dimuons we are interested in analysing and a large number of background particles. Behind the targets is FMag (Fe Magnet), a thick iron core magnet that focuses dimuons inwards and also acts as a beam dump. Located behind FMag are many detectors for tracking the muons, these include several planes of hodoscopes, drift chambers, and propulsion tubes. These detectors are sorted into four tracking stations. Station 1 is just behind FMag. Between stations 1 and 2 is KMag (kTeV Magnet), an air core magnet previously used by kTeV that bends the incoming muons so that their momentum can be calculated. Station 2 is behind KMag, followed by a gap in the spectrometer and then station 3. Between stations 3 and 4 is about a meter of iron that is used to block any hadronic matter that is left. Station 4 is mainly used for muon identification. Hodoscopes in each station are fed into a trigger matrix where the right combination of input signals will cause the DAQ to read out the data from that event. The prop tubes and drift chambers in each station are used for track reconstruction.

The beam travels in the positive z direction. The positive y direction is straight upwards and the positive x direction is defined by requiring a right handed coordinate system. The origin of the coordinate system is the location where the beam strikes the front of FMag.

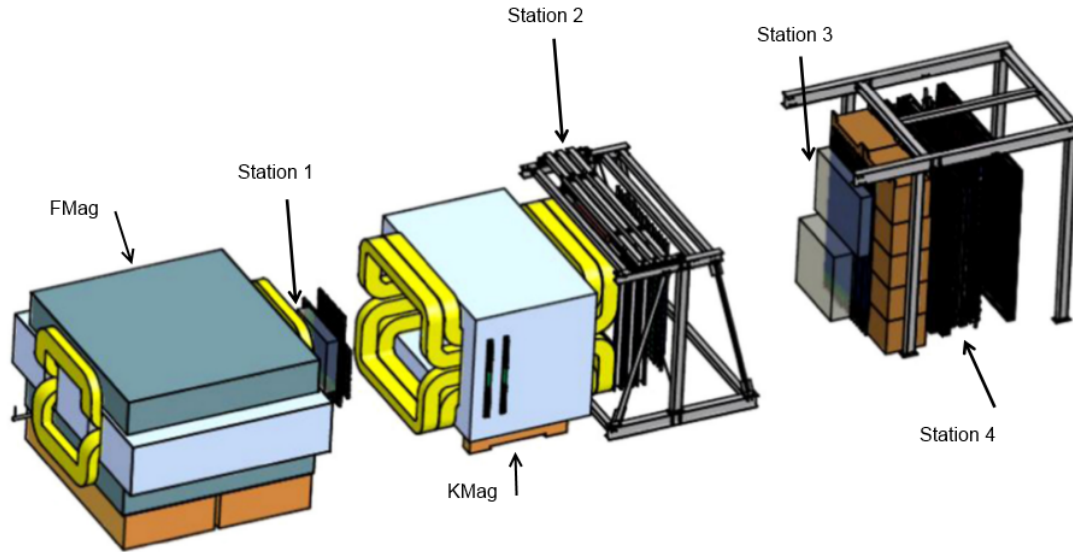


Figure 2.1: A figure of the SeaQuest spectrometer.

2.1 Timeline

Changes have been made to our setup throughout our experiment. Detectors have been moved out and back in for repairs, requiring new surveys. The trigger matrix has been updated. The magnet polarity has been flipped. The deuterium has been replaced with new bottles that have different contamination levels. All of these things affect the analysis of the data. Table 2.1 contains the dates of each roadset (roadsets will be explained in the Trigger section) and a few other significant events relevant to the analysis. Runs in this experiment are major data taking divisions, which mark significant events such as moving from commissioning to viable data taking or the installation of a new detector. The first viable data starts in run 2 and of this writing the experiment has finished run 5.

Run	Event	Date
2	Roadset 57	06/25/2014 to 08/20/2014
	Roadset 59	08/20/2014 to 09/03/2014
N/A	D3p and D3m moved	10/03/2014
3	Roadset 62	11/08/2014 to 01/14/2015
	Deuterium Change	11/13/2014
	Deuterium Change	12/02/2014
	Magnet Polarity flipped	01/14/2015
	Roadset 67	01/25/2015 to 06/19/2015
	Deuterium Change	04/24/2014
	D1 and H1 moved	05/13/2015
	Roadset 70	06/19/2015 to 07/03/2015
4	Constant adjustments	11/13/2015 to 03/06/2016
5	Roadset 78	03/06/2016 to 07/29/2016

Table 2.1: A table of important dates for this data analysis.

2.2 Beam

The 120 GeV beam energy that SeaQuest uses is a low beam energy compared to other Drell-Yan experiments, and this gives three main advantages[29][28]. First, the Drell-Yan cross section scales with $1/E$, where E is the energy of the beam. This increases the cross section by about a factor of seven compared to the previous experiment, E866. Secondly, radiation dose roughly scales with beam power, and a lower beam energy means one can have a higher luminosity but still have the same beam power and radiation. E866 received $2e12$ protons during their 20 second spill, once per minute. E906 receives an average of $6e12$ protons each five second spill, once per minute. The third advantage is background reduction. J/Ψ production was a large source of muons in the detectors in E866 but J/Ψ production is lower by about a factor of eight, according to the fit in *Measurement of J/Ψ and Ψ' production in 800 GeV/c proton-gold collisions*[31]. Most other backgrounds scale with s which is roughly proportional to the beam energy in a fixed target experiment.

The beam has a frequency of 53.1 MHz; SeaQuest receives a group of protons about every 18.8 ns. These groups of protons are no more than 2 ns long and are called buckets. Each bucket is part of a booster batch that is about 83 buckets long. There is a gap of about three buckets between each booster batch. A combination of six booster batches and a long gap of about 80 buckets makes up a single turn, which is exactly 588 buckets. There are 369,000 turns in a single five second spill. Every minute SeaQuest receives a five second spill followed by 55 seconds of no beam.

The beam provided to SeaQuest has unfortunate issues with non-uniformity. The beam contains a large number of "super buckets" that contain many more protons than the average bucket, as can be seen in figure 2.2, these events are nicknamed "splat events". These cause so many tracks that often more of the

detector elements have a hit than don't have a hit, as can be seen in figure 2.3. A clean event is provided for comparison in figure 2.4. A super bucket that lights up almost the entire detector is almost guaranteed to satisfy the trigger, but the event is so messy that it is extremely unlikely that any dimuon in the data can be reconstructed. When the trigger requirements are met the DAQ reads out the data which prevents any more data from being taken until the DAQ is finished. This dead time is proportional to the number of hits in the event, which makes these super buckets a particularly bad type of garbage event as they can cause several hundred μs of dead time.

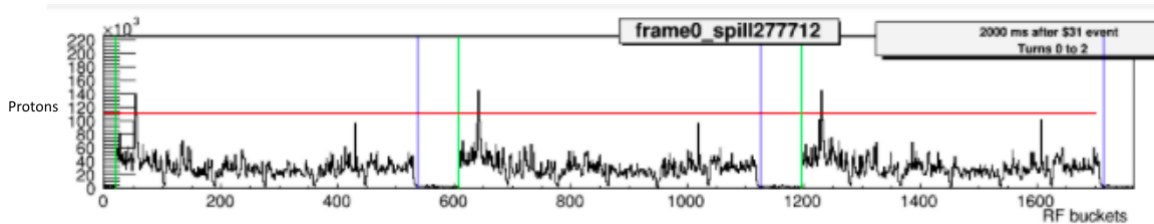


Figure 2.2: A plot of protons in each bucket. The booster batch and turn structure is visible. A typical reconstructed event has 25,000 protons and our intensity cut (data quality cut, not inhibit threshold) is at 60,000 protons. Super bucket spikes (those crossing the red line) are visible about once a turn. A single super bucket causes dead time for dozens of turns if it is not inhibited.

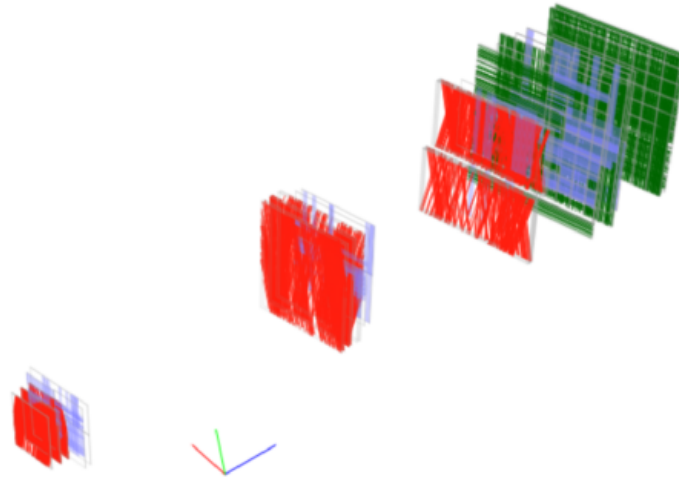


Figure 2.3: A diagram of a splat event, generated by the SeaView program. Most of the detector elements have fired.

A measure of the beam quality is the duty factor. Duty factor is usually given as a percent, and a duty factor of 100% would have a perfectly uniform distribution of protons between the buckets. The formula is in equation 2.1. When the experiment first began the duty factor was about 29%. This was much lower than expected, as the previous experiment E866 enjoyed a duty factor between 70% and 80%. In the middle

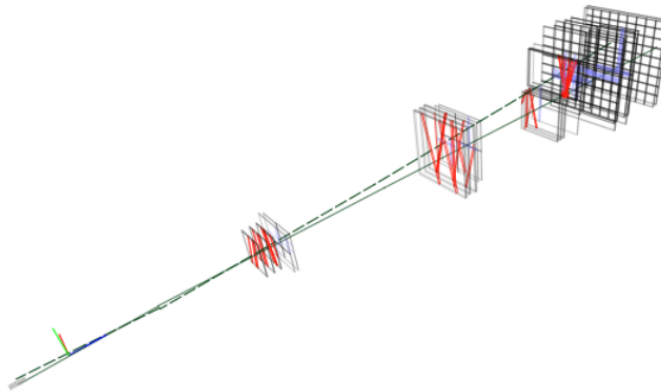


Figure 2.4: A diagram of a clean event, generated by the SeaView program. It is much more clear than the splat event.

of December 2014, the duty factor improved drastically to an average of about 43%. This event is known as the Christmas miracle.

$$duty_factor = \frac{(\sum_i^n I)^2}{n \sum_i^n I^2} \quad (2.1)$$

When we first started taking data, the recorded events were dominated by un-analysable super bucket events. The eventual solution was to install a Cerenkov counter in the beam line that outputs an analog signal proportional to the number of protons passing through it. The Cerenkov counter output was connected to a charge integrator and encoder(QIE) circuit board, which converted the total analog signal over the duration of a bucket into a digital signal. The QIE is synchronized with the Main Injector RF clock so that the integration intervals align with the buckets. If the QIE output is higher than a programmed inhibit threshold then the trigger can not fire for that bucket or for eight buckets before or after the offending bucket. Currently, this trigger inhibit blocks about 40% of the incoming protons. The trigger inhibit is also sometimes called the QIE inhibit or the beam monitor veto.

The QIE provides a lot of useful information as well as the trigger inhibit. When an event is read out, the QIE values for the triggering bucket and 16 buckets before and after the trigger are recorded. This is crucial for understanding the rate dependence of SeaQuest. It is also useful for normalizing data by the number of protons on target. The QIE records the total QIE value for the entire spill, the total QIE value while the trigger was inhibited, and the total QIE value while the trigger was not inhibited but we had dead time due to DAQ read out. These values are QIEsum, inhibit_block.sum, and trigger_sum.no_inhibit respectively and are in the BeamDAQ table.

To properly use the QIE numbers it is important to understand a couple of things. The QIE has a

pedestal, which is a non zero value that it reads out when there is no incoming beam. That number must be subtracted from any QIE values that are used. Also, the number that is read out is not the number of protons. A measure of the total number of protons for that spill, such as S:G2SEM in the Beam table or NM3ION in the BeamDAQ table, needs to be used to convert QIE values to protons. The conversion factor for QIE value to protons is $QIESum/S:G2SEM$. This number is not constant. The conversion factor gradually drifts over time as the mirror degrades over the course of several weeks. It also jumps suddenly if the mirror or the neutral density filters are replaced. This means this conversion factor should be calculated separately for every spill. Using all this information equation 2.2 can be used to calculate the number of live protons in the spill, which is the number of protons in the spill where the trigger was active and it was possible to take data and is the relevant measure of intensity.

$$live_protons = S : G2SEM \frac{QIESum - inhibit_block_sum - trigger_sum_no_inhibit}{QIESum} \quad (2.2)$$

Even after implementing the trigger inhibit, the intensity for any given event varies quite widely. The intensity distribution of buckets in our experiment is presented in figure 2.5. The intensity distribution of reconstructed dimuons is different and presented in figure 2.6. As a consequence of this we do our rate dependence corrections on an event by event basis instead of a spill by spill basis. The wide range of event intensities also helps us understand our rate dependence.

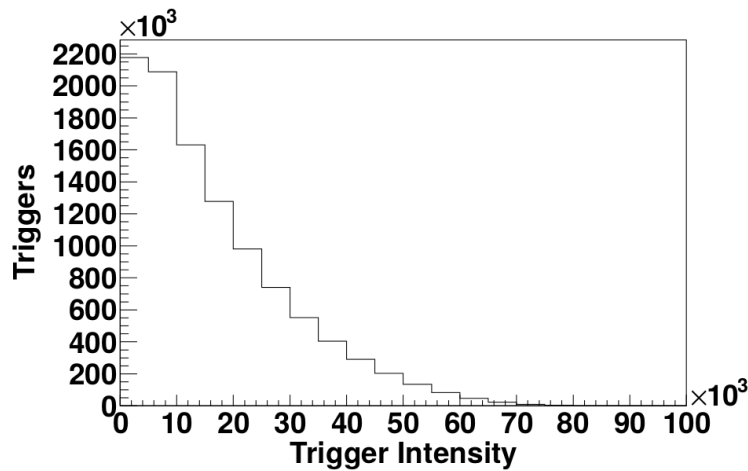


Figure 2.5: The distribution of intensity within buckets in our beam. This was taken from the intensity of events from our random trigger, NIM3. These are after the inhibit is in place.

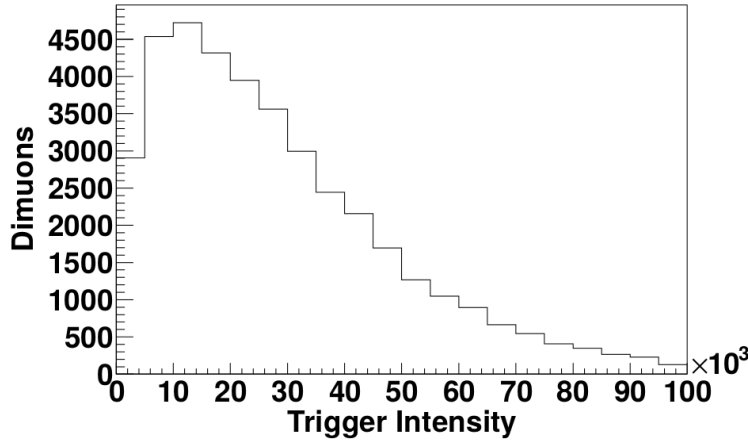


Figure 2.6: The distribution of intensity of triggering buckets in reconstructed dimuons.

2.3 Targets

SeaQuest uses seven different targets which are placed on a target rotation table, a diagram of which is in figure 2.7. The two liquid targets are flasks filled with liquid hydrogen (LH2) and liquid deuterium (LD2). There is a third flask of the same dimensions that contains vacuum which is for correcting for background that appears to come from the target. There are three solid targets made out of iron, carbon, and tungsten. There is a fourth solid target slot on the target table that contains nothing and is called the none target, this is also for background subtraction. Each solid target is actually made out of three separate discs that are spaced apart to attempt to cancel out any z position dependence in acceptance when comparing to the liquid targets. The center of the targets are at the position of 129.5 cm in front of the face of FMag. The liquid targets and the empty flask have a length of 50.8 cm. One target is in the path of the beam at a time, and the targets are changed in the 55 second gap between spills. A typical target rotation lasts about 23 spills, and then goes in reverse order for another 23 spills. This constant rotation avoids any systematic differences between the targets that could be caused by any feature of the spectrometer slowly changing over time. When we first started taking data there were 10 spills on the LH2 target and five spills on the LD2 target for every spill on the empty flask. Currently it is 10 spills on LH2 and five spills on LD2 for every two spills on the empty flask. Each target has an integer assigned to it that is used to identify it in our data. These integers can be found in table 2.2.

For a significant portion of our data taking our deuterium target was filled with impure deuterium. This was expected, but the puzzling aspect of this contamination is that it is significantly different between all four deuterium samples that were analysed. The four samples come from different bottles of deuterium in our experiment which were all filled many years ago at the same time from the same tube trailer which was

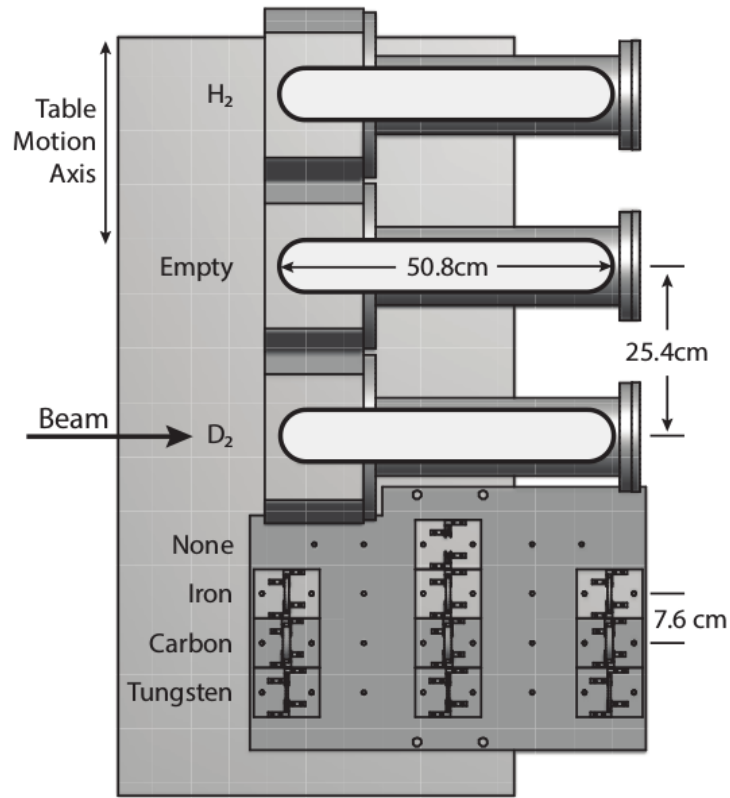


Figure 2.7: A diagram of the target table.

Target Material	Target Number
Liquid Hydrogen	1
Empty Flask	2
Liquid Deuterium	3
No Target	4
Iron	5
Carbon	6
Tungsten	7

Table 2.2: List of target identifiers

filled from a Fermilab bubble chamber. Some of the samples were filled from the bottles and some of the samples were filled from the target flask. Each sample has been analysed twice and the different analyses on the same samples are very consistent, with differences on the order of less than 0.1%. This has led to people asking if we have introduced major contamination during the sampling process and if all three bottles really do have the same composition. These theories have additional weight because some of the samples have significant N_2 and O_2 components, suggesting contamination by air. Additionally, hydrogen can diffuse into metal surfaces, so often containers are baked under vacuum in order to remove the hydrogen contamination. Word of mouth from Fermilab is that the bottles that hold our deuterium were probably not baked out before being filled with deuterium, although there is no documentation about the procedure used to fill them. We know that the target flasks and sample bottles were not baked out before being filled with deuterium, and that the deuterium target flask has been tested with hydrogen several times to avoid wasting the more expensive deuterium.

The samples taken have small amounts of helium and heavier nuclei. We have decided to work under the assumption that the heavier nuclear molecules are caught in the cold trap in the cryogenics system and do not make it into the target. We also assume that the helium exists in a gaseous state at the top of the target and does not interact with the proton beam. We then use the ratios of H_2 , HD , and D_2 to calculate the contamination while assuming the H_2 , HD , and D_2 adds up to 100%. We treat all the sample analyses as correct when deciding where to place the cross section ratio points, but use the minimum and maximum contaminations between all the samples as systematic uncertainties. SeaQuest continues to look into this and hopes to reduce the uncertainty from this value. Partway through roadset 67, we switched to commercial deuterium. This commercial deuterium is pure to a high level of precision. Our 1H gas has always been very pure as well.

The amount of contamination and its uncertainty by run number is found in table 2.3. There are a few different run ranges with different contamination levels, and transitions between these run ranges often happen in the middle of a roadset. For roadsets or combinations of roadsets where the contamination changes partway through, I average the contamination over all deuterium dimuons. The results of this averaging are in table 2.4.

To calculate a cross section requires some knowledge of the target properties. The lengths of the targets are 20 inches \pm 2.5 mm. The nuclear interaction lengths (NIL) in g/cm^2 and atomic masses were taken from the particle data group[39]. The target densities at our pressure and temperature were taken from National Institute of Standards and Technology[40]. The values for the deuterium targets need to be corrected for the 1H contamination. Using A as atomic mass, λ as the nuclear interaction length (in g/cm^2), ρ as the

first runID	last runID	contamination %	uncertainty+	uncertainty-
Commissioning	N/A	7.235	2.35	2.765
3230	11143	9.585	0	5.115
11144	11477	4.47	5.115	0
11478	14652	8.785	0.8	4.315
14653	present	0	0	0

Table 2.3: List of target contamination for runID ranges

roadset	percent ¹ H
57	9.585
59	9.585
62	8.707
67	4.691
70	0.0
All	6.209

Table 2.4: List of target contamination

density, H as hydrogen, D as deuterium, and F_i as the fraction of isotope i in the target:

$$A = A_H F_H + A_D F_D \quad (2.3)$$

$$\rho = \rho_H F_H + \rho_D F_D \quad (2.4)$$

$$\frac{1}{\lambda} = \frac{F_H}{\lambda_H} + \frac{F_D}{\lambda_D} \quad (2.5)$$

$$\lambda = \frac{\lambda_H \lambda_D}{F_H \lambda_D + F_D \lambda_H} \quad (2.6)$$

Some other quantities are calculated from these basic quantities.

$$NIL(cm) = \frac{NIL(\frac{g}{cm^3})}{\rho} \quad (2.7)$$

Beam Strength is the fraction of the original beam left at a distance z deep in the target.

$$BS = BeamStrength = e^{-z/NIL_{cm}} \quad (2.8)$$

Interaction fraction is the fraction of the beam that interacts with the target of length L .

$$IFrac = InteractionFraction = BS_{BeforeTarget} - BS_{AfterTarget} = 1 - e^{-L/NIL(cm)} \quad (2.9)$$

Target attenuated length is the average target length seen by a proton traversing the target. This is less than the actual length because some protons don't make it the full distance.

$$TargetAttenuatedLength = L' = \int_0^L e^{-z/NIL(cm)} dz \quad (2.10)$$

$$L' = -NIL(cm) * (e^{-L/NIL(cm)} - 1) = NIL(cm) * IFrac \quad (2.11)$$

Atoms per area is the number area density of atoms in the target, as seen by a proton moving in the z direction through the target.

$$AtomsPerArea = \rho * L' / A \quad (2.12)$$

The target properties are listed in tables 2.5 and 2.6, including for the contaminated deuterium targets.

material	length(cm)	ρ (g/cm ³)	NIL (g/cm ²)	NIL (cm)	A (g/mol)
LH2	50.8 ± 0.25	0.0708	52.0	734.5	1.00794
LD2 pure	50.8 ± 0.25	0.1634	71.8	439.4	2.01410
LD2 57, 59	50.8 ± 0.25	0.1545	69.3	448.3	1.91751
LD2 62	50.8 ± 0.25	0.1553	69.5	447.4	1.9262
LD2 67	50.8 ± 0.25	0.1591	70.5	443.5	1.9669
LD2 All	50.8 ± 0.25	0.1576	70.14	444.9	1.9515

Table 2.5: List of target properties. For the deuterium for a given roadset, note that the contamination is not necessarily constant, and these properties would not be constant. These are the properties for the average contamination.

material	IFrac	L'(cm)	atoms per area (atoms/cm ²)
LH2	0.0668	49.08	2.076e24
LD2 pure	0.1092	47.97	2.344e24
LD2 57, 59	0.1071	48.027	2.331e24
LD2 62	0.1073	48.022	2.332e24
LD2 67	0.1082	48.00	2.338e24
LD2 All	0.1079	48.005	2.335e24

Table 2.6: More target properties. For the deuterium for a given roadset, note that the contamination is not necessarily constant, and these properties would not be constant. These are the properties for the average contamination.

2.4 Magnets

The first magnet in the SeaQuest spectrometer, FMag, is located downstream of the target and upstream of all the detectors. It is an iron core magnet with no air gap between the iron and the coils and is five meters thick. The field is 2.07 T inside the iron. FMag serves many purposes; it increases our acceptance of high mass dimuons, it sweeps low momentum particles out of the acceptance, it acts as a beam dump, and it absorbs hadronic particles produced in the target.

Higher mass dimuons have larger opening angles and thus the muons have more p_T . Normally muons with this much p_T would be outside the acceptance of our experiment, but FMag bends the path of the muons passing through it. Depending on the orientation of the dimuon the muons could be bent outwards or inwards. Inward bent dimuons are moved into the acceptance of the spectrometer, while the outward bent ones probably would not have been in the acceptance to begin with. High x_T is correlated with high mass and low statistics, making acceptance at high mass very valuable.

Fmag also helps with background reduction. Any sort of hadron produced in the target is very unlikely to make it all the way through five meters of iron without being absorbed. While muons aren't absorbed through nuclear collisions like hadrons are, muons do lose energy while traversing the magnet and lower energy particles are bent farther by the magnet, usually bending them all the way out of the acceptance at low energies. This reduces the amount of low momentum background that makes it into the spectrometer.

Fmag has a hole that is approximately a foot deep and two inches in diameter drilled into the upstream face of it in the path of the beam. The portion of the beam that does not interact with the target strikes FMag at the end of the hole, a foot deep into the iron. Having this hole lessens the radiation in the target area that sometimes has to be accessed by people, both by moving it farther from the targets and by surrounding the interaction point with more iron.

The five meters of iron that make up FMag come with a significant downside. The amount of multiple scattering in FMag is significant and it adds a lot of uncertainty to the reconstruction process. According to the Monte Carlo simulations the average of the absolute value of the p_T change from multiple scattering is 0.44 GeV. As a result all of the kinematic variables have a lot of uncertainty to them. Running the reconstruction software on simulated J/Ψ tracks from the Monte Carlo ends up reconstructing a peak with that is smeared to have a half height width of about 300 MeV. Another important variable that has considerable uncertainty is the z position of the origin of the dimuon. Even with about a meter from the end of the target to the beginning of FMag there is not a clear separation between the peak from the target and the peak from the dump when looking at a graph of dimuon reconstructed z position, as seen in figure 2.8. Several cuts had to be applied to clearly separate the target dimuons from the dump dimuons, which is

very important if one is interested in the ratio of cross sections between two targets.

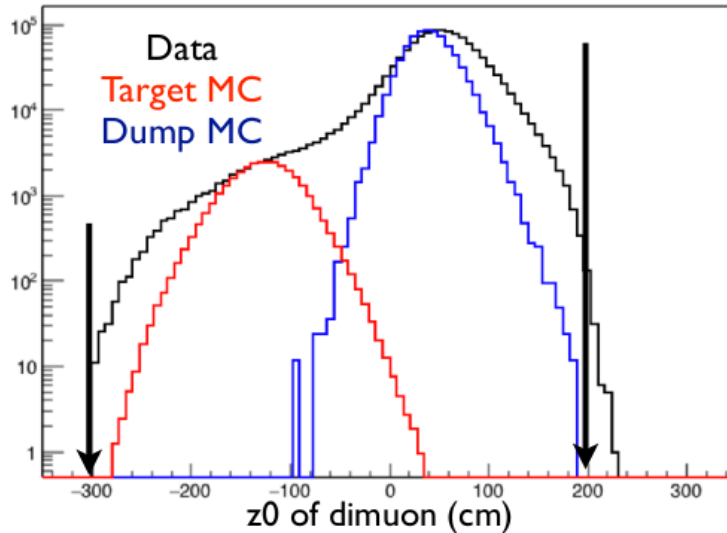


Figure 2.8: This graph shows reconstructed GMC dimuons originating from the target, reconstructed GMC dimuons originating from the beam dump, and all reconstructed dimuons from data. The z origin peaks from target and beam dump merge and are hard to separate without cutting a lot of data.

The average p_T kick in FMag is 3.07 GeV. The peak of the energy loss of a muon travelling through the magnet is about 7.6 GeV, but the spectrum has a long tail into the higher energy loss region and a short tail for lower energy loss which puts the mean energy loss at about 8.45 GeV. A graph of the energy loss distribution is shown in figure 2.9.

The second magnet, KMag, is located between detector stations one and two. It is an air core magnet with a magnetic field that peaks at 0.31 T in the center. The magnetic field is always parallel with the field from FMag. The placement between stations one and two causes the track to bend between stations one and two. Measuring the bend in the track allows us to calculate both the momentum of the track and its electric charge. The p_T kick going through KMag is 0.385 GeV. There is no energy loss since it is an air core magnet.

The polarities of both magnets were flipped between roadsets 62 and 67. Up to and including roadset 62 the fields pointed in the positive y direction, afterwards they pointed in the negative y direction. This was done to identify any left / right asymmetries in our spectrometer by comparing data sets before and after the switch. Another benefit was to reduce the radiation striking most of the electronic equipment, which was mostly on one side of the spectrometer. With the incoming beam being positive most of the radiation is also positive so there is an asymmetry in the amount of radiation between the two sides.

The shapes of both of the magnetic fields were calculated and their magnitudes estimated with simulations

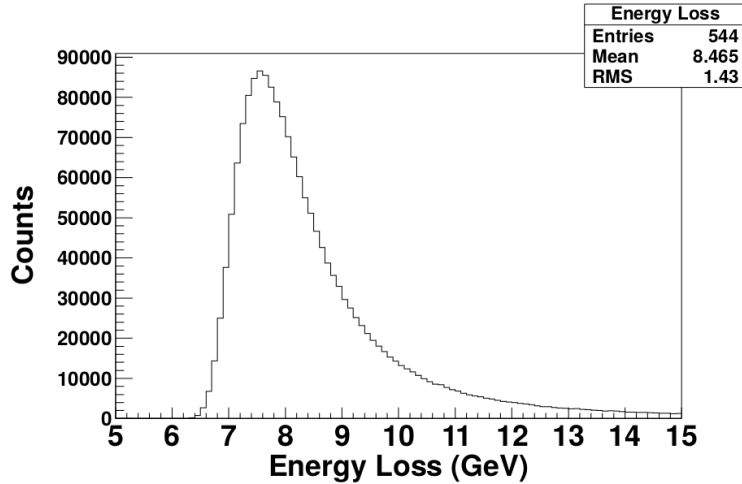


Figure 2.9: This graph shows the spectrum of energy loss of muons passing through FMag. It was generated from a Geant4 simulation.

done using CST EM Studio. Using the initial magnitudes the reconstruction of data was found to be inaccurate, with the J/Ψ peak at the wrong mass and the peak for the z origin of dimuons from the target at the wrong location. The reconstruction of Monte Carlo simulated data placed these peaks in the correct locations. Monte Carlo simulated data was used to calculate the effects of using inaccurate field strengths in the reconstruction software. Using the fits shown in 2.10 it was possible to know how much each field magnitude needed to change in order to accurately reconstruct the data. The multiplier for FMag field strength was found to be 1.054 and the multiplier for KMag field strength was found to be 0.951. After these multipliers were added to the tracking software it could accurately reconstruct these peaks in data.

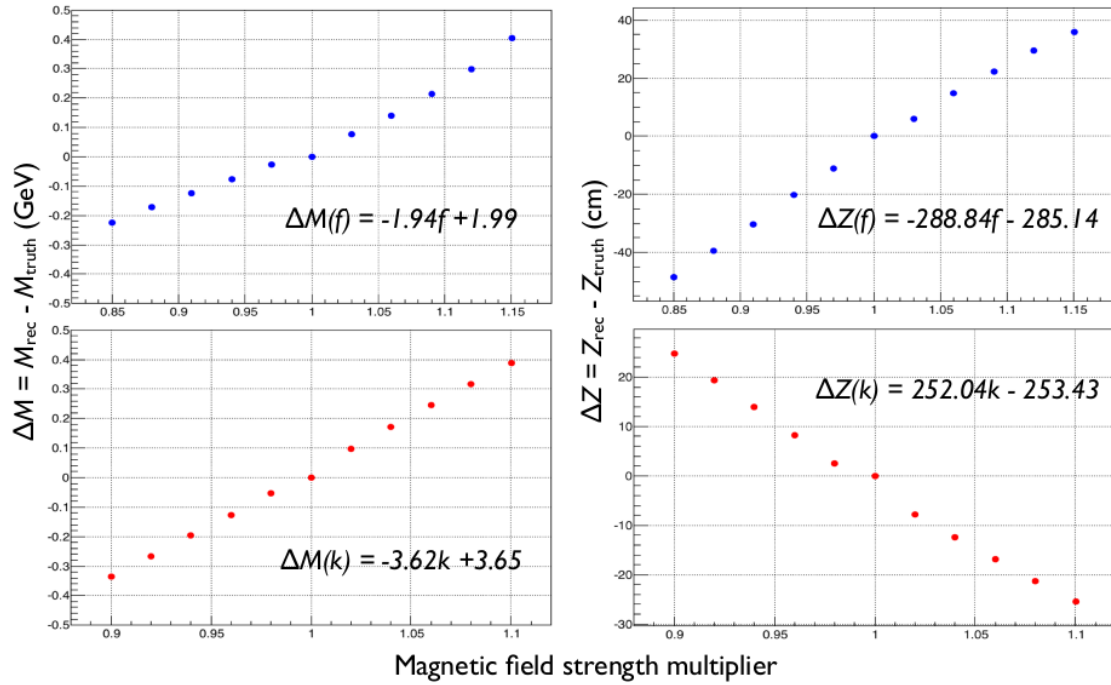


Figure 2.10: These graphs show the results of the reconstruction software running on Monte Carlo simulated data with a magnetic field strength multiplier. Inaccurate field strengths result in residuals in the reconstruction of the mass and z origin. The mass residual is positively correlated with both the FMag and KMag multipliers, while the z origin residual is positively correlated with the FMag multiplier and negatively correlated with the KMag multiplier.

2.5 Detectors

The detectors are loosely arranged into four stations, with gaps between the various stations. All of the stations contain hodoscopes, while only the first three contain drift chambers and only the fourth station contains proportional tubes (prop tubes). KMag is located between stations 1 and 2 to bend the tracks so that their momentum can be reconstructed. There are several meters of air between stations 2 and 3 so that the trajectory after the bend can be measured. There is a meter of iron between stations 3 and 4 that acts as a hadron absorber so that station 4 can act as a muon identification station, although the majority of tracks in the first stations should still be leptons.

2.5.1 Hodoscopes

The hodoscopes are detector planes that are made up of several long paddles placed side by side. Each paddle has a rectangular length made of scintillator, which is a type of material that emits light when struck by particles passing through. At the end of the rectangle is a shaped piece of scintillator called a light guide, mostly triangular, that connects to the rectangle at one end and has a narrow cylindrical end at the other side. This light guide funnels emitted photons from the paddle into a photo-multiplier tube (PMT). The photo-multiplier tube converts incoming photons to electrons and then amplifies the electric signal so that it can be read by the DAQ.

The main role of the hodoscopes is to be used as input for the trigger system. The trigger supervisor looks for preprogrammed combinations of hodoscope paddles, called roads, in order to fire. Hodoscopes are ideal for triggering because the signal that moves through them is light, so the largest possible drift time is still much shorter than the difference in time between buckets. With the drift chambers or prop tubes it is not possible to tell which bucket a signal came from. The width of the hodoscopes and lack of drift distance information means they are far too coarse to be used in track reconstruction.

There are two types of hodoscopes, x measuring hodoscopes and y measuring hodoscopes. The x measuring hodoscopes have vertically oriented paddles and are spaced horizontally, while the y measuring hodoscopes have horizontally oriented paddles and are spaced vertically. In each station there are two sets of x measuring hodoscopes, one that covers $y > 0$ and one that covers $y < 0$. The y measuring hodoscopes are similarly divided into a left set and right set covering $x > 0$ and $x < 0$, respectively. There is one plane of y measuring hodoscopes in stations 1 and 2, none in station 3, and two planes in station 4. The hodoscopes in stations 1 and 2 are single ended, while the hodoscopes in stations 3 and 4 are double ended. All of the hodoscopes have some slight overlap between neighbouring paddles. The names of all the hodoscope stations begin with "H", then the station number, then either "T", "B", "L", "R", "X", or "Y" for top, bottom, left,

right, x-measuring, or y-measuring. "X" is the combination of "T" and "B" and "Y" is the combination of "L" and "R". There is an exception for the station 4 y measuring hodoscopes, which instead of using 4 for the station numbers uses "4Y1" and "4Y2". So the left half of the second station 4 y measuring hodoscopes would be H4Y1L, and the top half of the station 2 x measuring hodoscopes would be H2T. The dimensions and z positions of the hodoscopes during run 2 are listed in table 2.7. Some of the hodoscopes had to be moved out and then back in place between runs 2 and 3. Their positions were surveyed again afterwards. The positions of the hodoscopes during run 3 are listed in table 2.8 if they changed.

Name	# Paddles	Paddle Width [cm]	Overlap [cm]	Width x Height [cm x cm]	z-Position [cm]
H1L	20	7.32	0.3175	78.74 x 140.117	654.03
H1R	20	7.32	0.3175	78.74 x 140.117	654.03
H1B	23	7.32	0.3175	162.008 x 69.85	667.118
H1T	23	7.32	0.3175	162.008 x 69.85	667.118
H2L	19	13	0.3175	132 x 241.285	1402.86
H2R	19	13	0.3175	132 x 241.285	1402.86
H2B	16	13	0.3175	203.238 x 152	1421.06
H2T	16	13	0.3175	203.238 x 152	1421.06
H3T	16	14.5875	0.3175	227.518 x 167.64	1958.51
H3B	16	14.5875	0.3175	227.518 x 167.64	1958.51
H4Y1L	16	23.4775	0.3175	152.4 x 365.797	2130.27
H4Y1R	16	23.4775	0.3175	152.4 x 365.797	2146.45
H4Y2L	16	23.4775	0.3175	152.4 x 365.797	2200.44
H4Y2R	16	23.4775	0.3175	152.4 x 365.797	2216.62
H4T	16	19.6475	0.3175	304.518 x 182.88	2235.5
H4B	16	19.6475	0.3175	304.518 x 182.88	2250.68

Table 2.7: Hodoscope properties during run 2.

Name	z-Position [cm]
H1L	653.923
H1R	653.923
H1B	666.681
H1T	666.681
H2L	1404.93
H2R	1404.93
H2B	1421.11
H2T	1421.11
H3T	1958.62
H3B	1958.62
H4Y1L	2130.27
H4Y1R	2146.45
H4Y2L	2200.44
H4Y2R	2216.62
H4T	2234.91
H4B	2251.09

Table 2.8: Hodoscope positions during run 3.

The hodoscopes for stations 1 and 2 were designed and assembled by the University of Illinois at Urbana-Champaign.

2.5.2 Drift Chambers

Drift chambers are sealed chambers filled with gas, many wires, and an electric field. A charged particle passing through the gas at high enough velocity will ionize the gas, creating positive nuclei and free electrons. The electric field is between the sense wires, which are held at a higher voltage, and the field wires, which are held at a lower voltage. The electrons are pulled towards the sense wires and are accelerated enough to ionize other atoms, producing more electrons. When the electrons reach the sense wire a signal is created. A typical drift chamber has three planes of wires. The first and third planes are all cathode wires, and the second plane alternates between sense wires and field wires. The cathodes have varying voltages designed to create a uniform electric field. The cathodes nearest the sense wires are held at the sense wire voltage while the wires nearest the field wires are held at the field wire voltage. There are usually several wires between those extremes that form a gradient of voltages. A drift chamber has a strong position resolution because the time it takes for the electrons to drift to the sense wire depends on the distance of the track from the sense wire. Using this sensitivity requires scintillating detectors like the hodoscopes nearby so that the track timing is known. The longest possible drift time is known as the memory time of the chamber.[41]

The gas mixture used in our drift chambers is Argon:Methane:CF₄ (88%:8%:4%) which has a drift speed of about 20 $\mu\text{m}/\text{ns}$. The position resolutions of our chambers vary a bit but are about 0.25 mm. The memory times of our chambers are up to about 250 ns. There is a problem called left / right ambiguity, it is not known whether the particle passed on the left side of the sense wire or the right. For this reason the drift chamber planes in our experiment come in sets of two, a primed and an unprimed plane. The wires of the primed plane are shifted half a cell width compared to the unprimed plane. The left / right ambiguity of the unprimed plane is solved by seeing which wire in the primed plane was struck. At any station in our experiment there are three views, each with one primed unprimed pair. The "X" view has wires aligned with the y direction and measures in the x direction. The "U" view is rotated 14 degrees from the y direction and the "V" view is rotated -14 degrees from the y direction. The combination of three views lets us reconstruct the trajectory of the particle, although we have given up some slight precision in measuring in the y direction for more precision in the x direction. At station 3 there are two sets of wire chambers with three views each, one at $y > 0$ and one at $y < 0$. There is some small overlap between the top and bottom chambers at station 3.

The names of all the wire chambers start with "D". Then either "1", "2", "3m", or "3p" depending on

which station; "3p" stands for three plus and are the $y > 0$ wire chambers at station 3 while "3m" stands for three minus. Next is "X", "U", or "V" depending on the view, and if the plane is primed it has a " ' " or a "p" at the end. So the station 1 x view unprimed plane would be "D1X", and the top station 3 u view primed plane would be "D3pU'" or "D3pUp". A list of the wire chamber statistics during runs 2 and 3 can be found in table 2.9. A diagram of one of our drift chambers is found in figure 2.11.

Detector Plane	# of Wires	Cell Width [cm]	Width x Height [cm x cm]	z-Position [cm]
D1U	201	0.635	101.6 x 121.92	594.49
D1U'	201	0.635	101.6 x 121.92	595.125
D1X	160	0.635	101.6 x 121.92	617.086
D1X'	160	0.635	101.6 x 121.92	617.721
D1V	201	0.635	101.6 x 121.92	637.169
D1V'	201	0.635	101.6 x 121.92	637.805
D2V	128	2.021	233.274 x 264.16	1314.98
D2V'	128	2.021	233.274 x 264.16	1321.96
D2X'	112	2.083	233.274 x 264.16	1340.36
D2X	112	2.083	233.274 x 264.16	1347.34
D2U	128	2.021	233.274 x 264.16	1365.99
D2U'	128	2.021	233.274 x 264.16	1372.98
D3mV'	134	2	320 x 166	1886.77
D3mV	134	2	320 x 166	1888.77
D3mX'	116	2	320 x 166	1892.77
D3mX	116	2	320 x 166	1894.77
D3mU'	134	2	320 x 166	1898.77
D3mU	134	2	320 x 166	1900.77
D3pV'	134	2	320 x 166	1923.33
D3pV	134	2	320 x 166	1925.33
D3pX'	116	2	320 x 166	1929.33
D3pX	116	2	320 x 166	1931.33
D3pU'	134	2	320 x 166	1935.33
D3pU	134	2	320 x 166	1937.33

Table 2.9: Drift chamber properties.

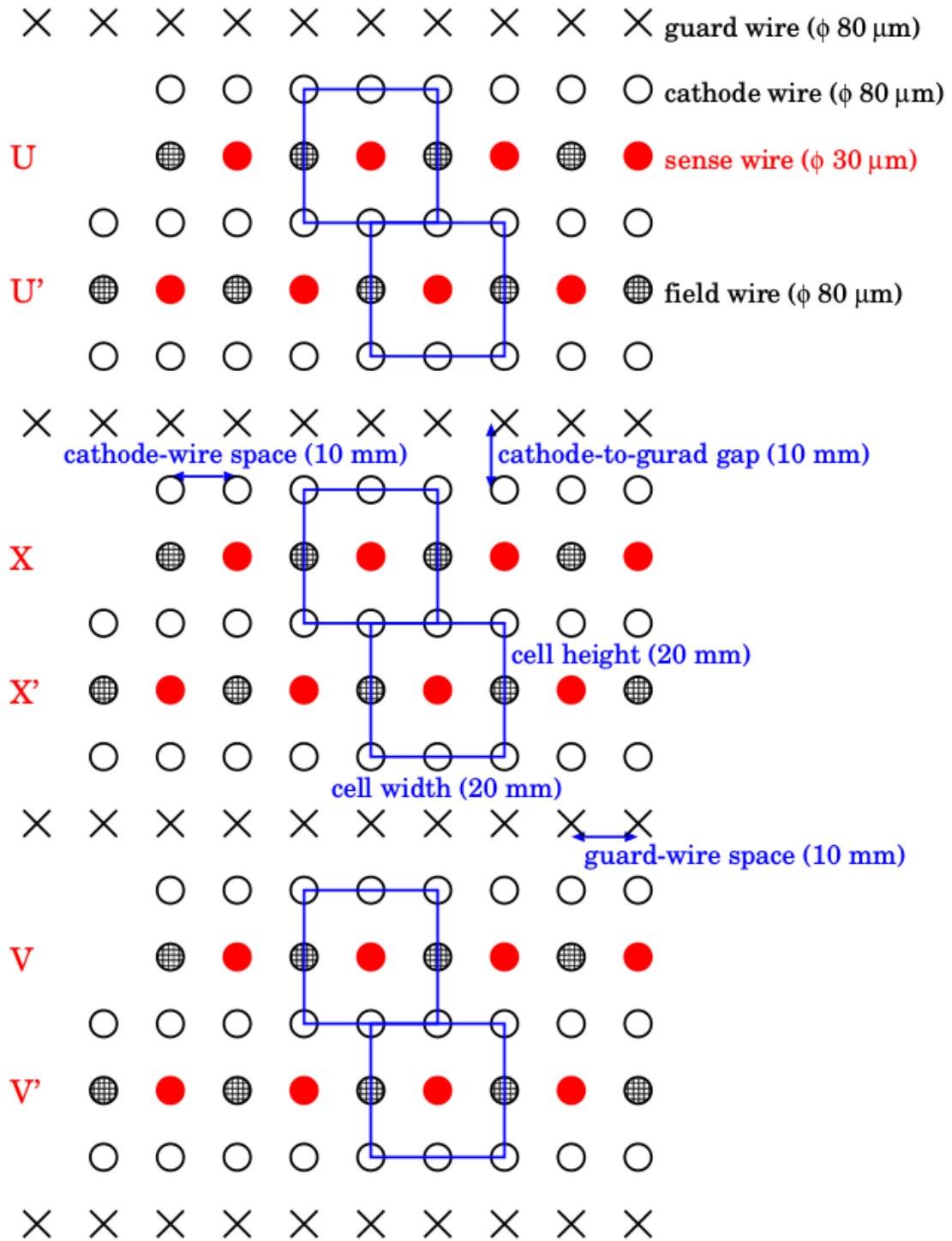


Figure 2.11: A diagram of a set of drift chambers in station 3. Most drift chambers have more tightly spaced cathodes in the cathode plane.

2.5.3 Proportional Tubes

The proportional tubes in our experiments are planes of tubes each individually filled with gas. The outside of the tubes are grounded and each one has a positively charged wire running along the center. Each tube is filled with the same gas that fills our wire chambers and in a similar manner the positions of the hits are known from the drift times. Proportional tubes are receive their name from the fact that the strength of the output signal is proportional to the energy of the passing particle. Unfortunately, this only works for lower energies and the difference in signal strength for different relativistic energies is negligible, so this feature is not useful in our experiment.

The main role of the prop tubes in our experiment is muon identification. There is a meter of iron between station 3 and station 4, and the prop tubes are only located in station 4. The meter of iron is there to absorb hadrons and electrons while letting muons pass through. If there are several prop tube hits aligned with a track passing through stations 2 and 3 the track is considered to be a muon.

There are four planes of prop tubes in the experiment. In each plane there are two layers of prop tubes, with the second layer directly behind the first and staggered half a tube width, similar to the primed and unprimed planes in the wire chambers. Each plane is also divided up into nine modules in sets of 16 tubes each, containing 8 consecutive tubes in the front layer and 8 consecutive tubes in the back layer. Two of the planes are aligned horizontally (pointing along the x axis) and two of the planes are aligned vertically (pointing along the y axis). The prop tube names begin with "P", then either a "1" or a "2" if they are one of the first two or last two planes, respectively. Then an "H" or a "V" based on whether they are aligned horizontally or vertically. The prop tube modules also have names that begin with the name of the plane and appends a number "1" through "9". An "f" or "b" is appended if one is only talking about the upstream or downstream layer, respectively. Diagrams of the labelling can be found in figures 2.12 and 2.13. A list of the prop tube stats can be found in table 2.10.

Plane Name	# of Tubes	Tube Width [cm]	Width x Height [cm x cm]	z-Position [cm]
P1H	144	5.08	368.3 x 368.3	2100.7
P1V	144	5.08	368.3 x 368.3	2176.6
P2V	144	5.08	368.3 x 368.3	2369.1
P2H	144	5.08	368.3 x 368.3	2392.2

Table 2.10: Drift chamber properties.

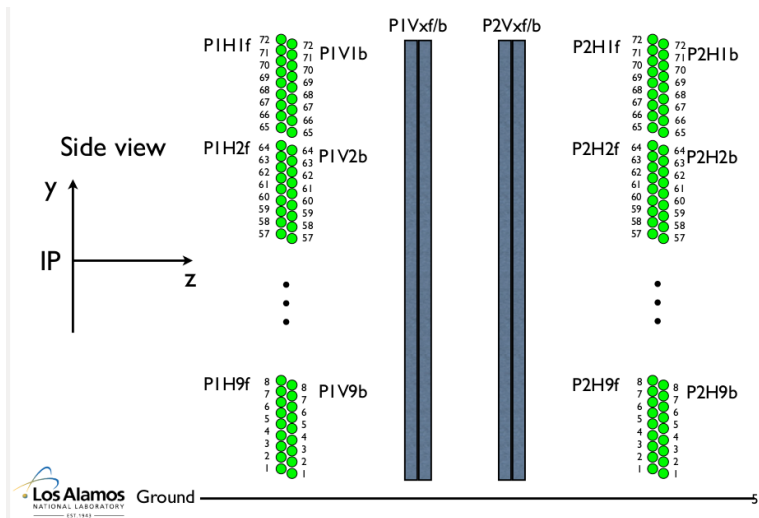


Figure 2.12: A diagram of the prop tubes. The labelling for the horizontally aligned prop tubes is shown.

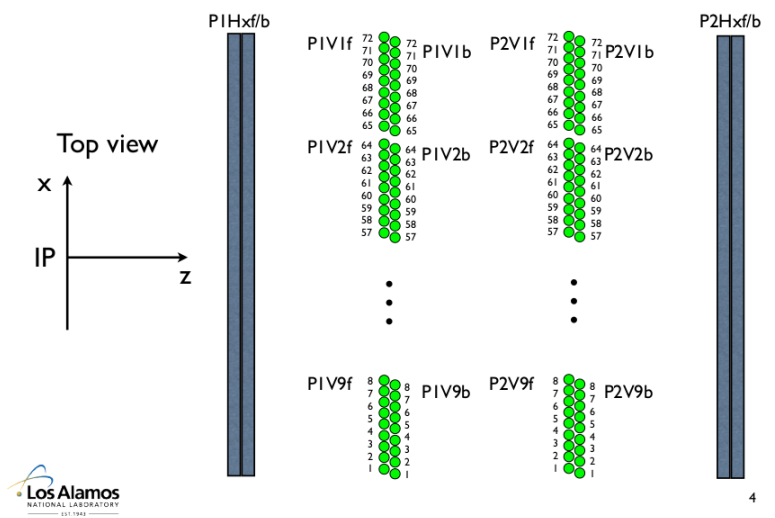


Figure 2.13: A diagram of the prop tubes. The labelling for the vertically aligned prop tubes are shown.

2.6 Trigger

Seaquest has a high background to signal ratio and requires a robust trigger system to capture the events we are interested in while reducing the readout of useless data. The Drell-Yan process is a relatively rare process and contributes very little of the total number of muons moving through the detector. Additionally, the targets are all very roughly around 10% interaction length, so most of the Drell-Yan events that reach the spectrometer are events from the beam dump which we do not want to record. When we trigger on an event, whether it is one we desire or not, the dead time has a rough average of 150 μs and varies a lot based on how many hits the DAQ needs to readout. During periods in which the QIE based trigger inhibit is letting triggers fire, the dead time with our current trigger blocks about 20% of the incoming protons. The trigger also has to be simple enough that it can output a decision within one μs , which is the amount of time before the data from an event is readout from the drift chambers. Put together, these factors require a robust trigger system for the SeaQuest experiment[42].

The main trigger system for the experiment is the FPGA trigger system, and is comprised of several levels of logic gates. All of the levels use CAEN v1495 6U VMEbus modules. I will call them v1945s for short. Each module has a TDC, which stands for time to digital converter. The TDCs read the leading edges of the signals from the hodoscope paddles and store the timing information. The TDCs store many hits at once for each channel, but only one hit per channel per 16 ns timing bin. The fine timing information has 1 ns resolution but there is still only one hit stored per 16 ns timing bin. If a second hit arrives from the same channel in the same bin, the earlier hit is discarded. Also, adjustable, channel specific delays are applied to the data at this point. These delays are necessary because the hodoscopes are not all the same distance from the trigger electronics and with ns resolution the distance has a very significant effect on the timing. The v1495s also each contain an FPGA, which stands for field programmable gate array. The field programmable part means that the logic gates can be setup by the user. In the v1495s each logic gate can take up to four inputs and have a single output based on a simple logic operator.

The first level, level 0, uses four v1495s and simply passes the signals from the hodoscopes on unchanged to level 1 during data taking. When we are not taking data, level 0 is used to perform diagnostic tests of the trigger. It can be switched to output signals from a pulser instead of signals from the hodoscopes. This pulser sends user-defined signal patterns to the level 1 module in order to test the response of the trigger logic. The level 1 trigger uses four v1495s and looks for combinations of hodoscope hits matching "trigger roads". A trigger road is a combination of four hodoscope paddles, one from each of the four hodoscope stations, that was deemed likely to contain a muon from a Drell-Yan event. The first part of the level 1 trigger uses a separate AND gate for each trigger road. The outputs from this first step are then combined with OR

gates to a smaller number of output channels. Trigger roads from the top half of the spectrometer are kept separate from trigger roads from the bottom half. Trigger roads for positive tracks are kept separate from trigger roads for negative tracks. The output channels are also divided by an estimate of the x momentum of the track but that information is not used in the dimuon trigger. The set of all valid trigger roads is called a roadset. The roadset has changed several times over the course of the experiment. The level 2 triggers use a single v1495 and looks for combinations of input channels which match its criteria. There are multiple triggers, most of which are turned on during data taking, most of which are prescaled. A prescale means the trigger will only take effect 1 out of x times, where x is the prescale number. A list of these trigger conditions can be found in table 2.11. When a trigger fires, a Common Stop signal is sent out to all of the TDCs, including the ones for the hodoscopes, drift chambers, and trigger system. When this signal is received the data stored in these TDCs is recorded by the DAQ.

Trigger	Half	Charge	Momentum	Notes
FPGA 1	TB	+-	N/A	The standard dimuon trigger which we use for data taking
FPGA 2	TT or BB	+-	N/A	Not used, too many background events
FPGA 3	TB	++ or --	N/A	Same sign trigger used for estimating combinatoric background
FPGA 4	T or B	+ or -	N/A	Single muon trigger
FPGA 5	T or B	+ or -	$> 3GeV$	High momentum single muon trigger

Table 2.11: A list of the level 2 trigger logic conditions for the FPGA triggers. They are sometimes called MATRIX 1, MATRIX 2, etc. In the half column, T stands for a track in the top half and B stands for a track in the bottom half. TB means there needs to be one track from each half.

There are also a handful of NIM triggers that don't use the logic array. The most important of these triggers is the NIM 3 trigger, which selects which bucket to record data from at random. This is turned on at a fairly large prescale during data taking. This is useful for analysing background because all of the other triggers have a bias towards high background events. It is also useful for analysing the intensity spectrum of the incoming buckets.

There were some improvements to the trigger system between runs 2 and 3. In run 2, the clocks of the v1495s were not synchronized with the Main Injector RF-Clock. The hodoscope hits were separated into 16 ns bins in the v1495s, and there could only be one hodoscope hit recorded per channel per bin. Since these bins were not lined up with the RF-Clock, half of the bin could be closer to one bucket and the other half to another bucket. Because of this, a hit from one bucket could overwrite a hit from a different bucket, causing inefficiencies in the trigger and also the detector elements in the recorded data. This would not be uncommon in high intensity events, as the timing jitter for the largest hodoscope paddles is close to ± 8 ns. For run 3 the v1945s were synchronized to the RF-Clock. The time resolution was increased to 1.177

ns and the width of the timing bins in the TDCs were increased to 18.9 ns which is the amount of time between buckets. This has fixed the issue. Analysers should be aware that there may be a small difference in recording hits between runs 2 and 3. This thesis has analysed data from both runs 2 and 3.

A lot of care has been put into choosing which trigger roads are programmed into the FPGAs. Simulated Drell-Yan data from our Monte Carlo, called GMC, was used to estimate what roads would have a high frequency of signal. Of special interest were the events with high x_T values, higher than the region precisely measured by E866. GMC was also used to simulate where the regions of high background would be and roads with high background were not used in the trigger even if there was Drell-Yan signal in that region as crippling dead time had to be avoided. Once an initial set of trigger roads was generated, it was used to take data, and the data was analysed for hot roads that were generating more dead time than they were worth. Several of these hot roads were found and turned off to reduce the dead time.

2.7 DAQ

The Data Acquisition (DAQ) systems in SeaQuest are divided into four parts. The Main DAQ responds to the trigger system and controls the readout of hit information. The Beam DAQ controls the real time analysis and readout of information from the QIE. The Scaler DAQ controls the readout of counters that are tallied throughout the spill. The Slow Control coordinates an assortment of miscellaneous scripts that only need to be recorded once per spill.

The Main DAQ starts with the trigger supervisor, which is a VME (Versa Module Europa, which is a computer bus standard) crate that receives the trigger signals. If the DAQ is already busy reading something out, or the trigger inhibit from the beam monitoring electronics is on, then the trigger signal is ignored. The prescale is also applied at this step, the trigger supervisor keeps track for each trigger how many times the signal has been received since the last time that trigger fired. If that number is less than the prescale number and the signal is not ignored due to the beam based inhibit or the DAQ being busy, then the trigger is accepted. When this happens, the trigger supervisor sends a signal to all of the other VME crates that are part of the main DAQ. Each VME crate has a CPU called a ROC (read out controller) that handles the readout of the several TDCs in each crate. When the ROC receives the trigger accepted signal it will interrupt the normal behavior of the TDCs and start reading out the data collected by the TDCs, one TDC at a time.

The software that coordinates all of this is called CODA (CEBAF (continuous electron beam accelerator facility) On-line Data Acquisition), which was developed at Jefferson lab. CODA takes the several separate

information streams from all the different ROCs and uses them to build a single event data structure, one event for each accepted trigger. When CODAs buffer is full or when a run ends the events are written to a CODA file. A separate piece of software, called the decoda and written by Bryan Dannowitz [43], translates these files into MySQL schemas. A small sample of the events are uploaded to a MySQL server in real time in order to provide online monitoring of the hit data so people can keep an eye out for dead or hot channels and other potential problems.

The Beam DAQ also reads out information when the trigger is accepted and outputs the intensity information of all buckets within 16 buckets of the trigger bucket to the Main DAQ to be included in its CODA file. Additionally, it stores all of the intensity information from a single spill and at the end of the spill analyses it to calculate several spill level quantities relating to the beam. It calculates the total QIE values for all buckets, the total QIE value of all buckets that occurred while the trigger inhibit was active, the total value of all buckets that occurred during dead time when the trigger inhibit was not active, and the duty factor. These quantities are recorded once per spill and are also displayed in the control room for monitoring. Additionally, a multi-threaded process can record the intensity data for the entire spill to a text file before the next spill occurs. It is approximately 300 MB of data for a single spill and the collaboration possesses no software to analyse the files. However, it is good to have such records available just in case they are needed for debugging something.

The scaler DAQ is governed by a separate instance of CODA software which records data twice per spill, once at the beginning and once at the end. It records a measure of beam intensity from NM3SEM (NM3 is the location at Fermilab, and SEM stands for secondary emission monitor). It also, for each trigger, records the raw number of triggers generated, how many triggers were generated when the beam monitor inhibit was not on, and how many triggers were accepted by the trigger supervisor. There are also channels that record rates of hits in the top and bottom halves of all the hodoscope planes, but this data is not included in the MySQL schemas. Many of these scalers are monitored in real time in the control room. They are also uploaded to the MySQL schemas.

Slow Control is coordinated by an EPICS(Experimental Physics and Industrial Control System) program which collects data together from several different sources. Fermilab Accelerator Controls Network (ACNET) provides some of this information, which includes the status of the magnets and measurements of the beam intensity which are independent of the Cherenkov counter. These measurements are only on the timescale of an entire spill but are also well calibrated and do not drift over time. There is also equipment that monitors environmental information in the experimental hall including temperature, humidity, and pressure. These environmental quantities are not used in analysis but are recorded so that we would have the capability to

debug related time dependent effects in our data. Fortunately, no such effects have been discovered. Target position is recorded, as well as the temperature and pressure of the liquid targets. The status of the liquid targets is closely monitored in the control room and alarms will go off if problems occur.

The data taking for all of the DAQs can be stopped and started from an instance of CODA running in the main control room. It has been the practice of this experiment to stop data taking and start a fresh data taking run whenever the current file reaches a size around 1 GB. This happens on the order of about one hour. This is a compromise between stability and how often we lose a spill of data by stopping and restarting. Each of these files is a single run and has a unique run number. All run numbers for viable data are four or five digits long. These are not to be confused with the other definition of run for our experiment, where run numbers are assigned to major sections of data taking that last several months.

2.8 Tracking

The main tracking program for our experiment is called kTracker, which stands for Kalman Tracker as it is based on a Kalman filter. The tracking for this experiment is a very non-trivial exercise due to the high rates in our detectors. A balance of efficiency, purity, and computation time all factored into the development of this tracking program. Another tracking program called Sqerp (SeaQuest Event Reconstruction Program) is also being developed for purposes of cross checking and refining tracking technique.

The first step in kTracker is to remove artificial clusters of hits. If there are two hits on two adjacent wires where one of the hits is greater than 90% of half the cell width and the other hit is greater than 40% of half the cell width, then it is assumed that both hits were caused by a single track moving at an angle. In this case, the hit with the greater drift distance is removed. This removes approximately 25% of the clusters in the data.

Another type of hit cluster removal used is a cut on electronic noise. If two hits on two adjacent wires have times within 8 ns of each other, the hits are considered to be electronic noise and are removed. If a string of 3 or more hits on adjacent wires have similar times, with an average time difference between hits of 10 ns or less, then all of the hits are considered electronic noise and are removed. This removes about 15% of the clusters.

The last type of hit cluster removal is delta-ray removal. Clusters that are at least three hits long and not considered electronic noise have the hits in the middle removed and keep one hit on each end. This is the only type of hit removal that seems to have a major problem of removing true hits, as leaving out the delta ray removal improves the rate dependent inefficiency by a lot, as shown in 2.14. Unfortunately, the

computational time of running kTracker on all the data without delta ray removal is prohibitive.

In addition to cluster removal, when there are two hits on the same wire in the same event, the later of the two hits is discarded. This is called after pulse removal and we believe that most of these hits are the result of electronic reflections and not true hits. Also, all the trigger roads for the event's hodoscope hits are calculated and any hodoscope hit that is not on one of these trigger roads is discarded.

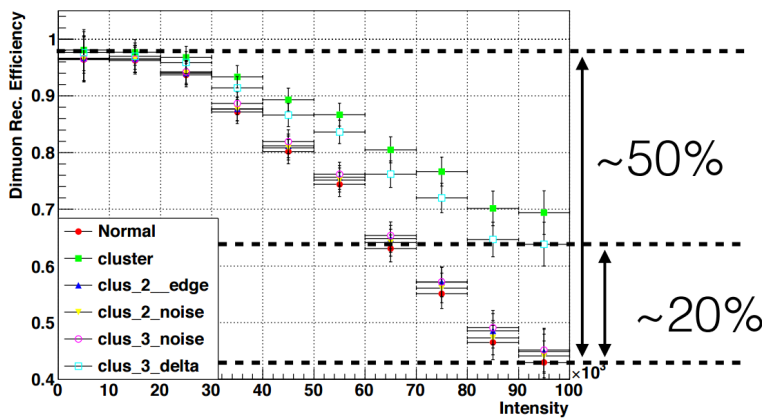


Figure 2.14: A diagram of rate dependence after various forms of cluster removal. Delta ray removal has a much stronger effect than all other cluster removal combined.

After the first step of hit removal are the event quality cuts. Events with high occupancies in any given wire chamber are removed, as the likelihood of a successful reconstruction is very low and the amount of computational time given to such an event is very high. The cuts on detector occupancy are listed in table 2.12.

Detector	Maximum
D1	320 Hits
D2	160 Hits
D3p	150 Hits
D3m	150 Hits

Table 2.12: A list of all the occupancy cuts that an event has to pass in order to be eligible for tracking.

After this stage "triplets" are built in stations 2 and 3. They are called triplets because they combine wires from the X, U, and V views. First, hits in the X and X' planes are combined. Then they are matched up with possible hits from the U and/or U' planes. Then they are matched up with hits in the V and/or V' planes. Valid triplets have to contain at least four hits and have at least one hit from each of the X, U, and V views. A rough fit of each triplet that does not use drift distance is done, and the triplet has to point towards both a hodoscope hit (with a fudge factor because of triplet imprecision) and be on a trajectory that could have possibly come from the target.

After these triplets are generated, combinations of triplets from station 2 and 3 that roughly point towards each other are fitted. These fits have a more precise trajectory and are requirement to point towards hodoscope hits in stations 2, 3, and 4, this time without a fudge factor. The requirement to be on a trajectory that could have come from the target is again checked. Also, it has to point towards enough prop tube hits, after accounting for multiple scattering in the absorber, to be considered a muon track. If two partial tracks share at least a third of the hits, the one with the larger χ^2 is dropped. At this stage, the tracker attempts to resolve the left right ambiguity in the wire chamber hits.

While searching for possible cuts, it was noticed that the ratio of two quantities, r_1 and r_2 shown in figure 2.15, was close to a constant. Figure 2.16 shows the consistency of this ratio. The kTracker takes advantage of this by calculating the value of r_2 for the partial track and using it to estimate the value of r_1 . This estimate is used to generate a narrow window ($r_1 \pm 5cm$) of station 1 hits that can be paired with that partial track. The tracker then resolves the leftover left right ambiguity for each view that has both a primed and unprimed hit by requiring that the track slope is consistent with the hits. For any views that only have one hit a χ^2 value is calculated for the entire track twice, once with the hit on each side, and the hit is assigned to the side with the smallest χ^2 .

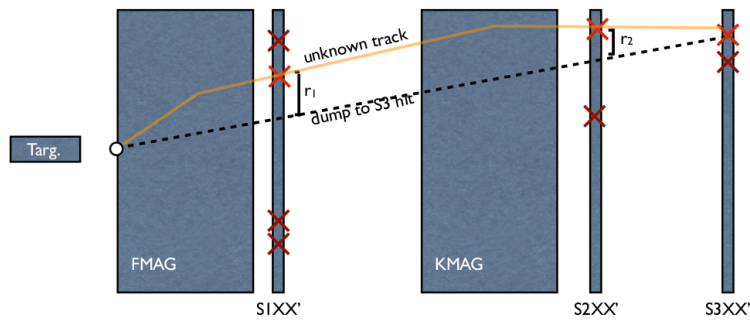


Figure 2.15: A diagram of how the sagittas are calculated.

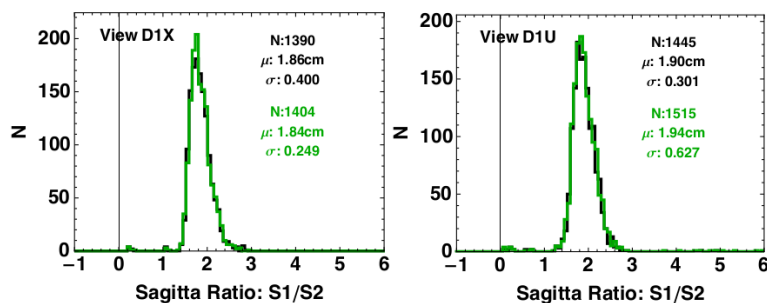


Figure 2.16: Graphs of the sagitta ratio r_1/r_2 for the X and U views. They peak fairly sharply, enabling this to be used as a cut early on in the tracking process.

Next the track removes bad hits. The hit with the largest residual is removed if the residual between the track and the hit is greater than three times the resolution of the chamber. The track is then refit. The process is repeated until no hits have a residual that is greater than three times the resolution of the chamber. The entire track is dropped if the track no longer fits the basic criteria. The track must still point to fired x hodoscope paddles in all stations. The track must have at least four hits in all stations and at least one hit in each view in all stations. The track must be between 5 and 100 GeV, and the deflection in the absorber in front of station 4 can not be too much larger than expected.

At this stage the tracker uses a method based on the Kalman Filter technique in order to do a more precise fit of the track compared to the earlier coarse results. The Kalman Filter technique is where one uses a series of measurements to iteratively update the parameters of a model. At each step the difference between the model's prediction and the current measurement, the uncertainties on the measurement, and the uncertainties of current model's parameters are used to update the parameters of the model and the uncertainties of those parameters. Instead of a series of measurements in time, kTracker uses each hit as a separate measurement to update the model. Once all the hits have been added, it loops back around and adds the hits again, repeating until the track parameters have converged.

After the Kalman Filter kTracker "swims" the tracked muon back through FMag to find the origin of the track. The muon starts at the back end of FMag, with the position and momentum predicted by the tracker so far. Then FMag is divided up into slices and the muon is swum through each slice. In the first half of the slice, half of the energy loss is applied, although since the simulation is going backwards in time it is in one way an energy increase. Then the p_T kick for that slice is applied in the middle of that slice, and then the other half of the energy loss is applied. Kun found that the tracker is most accurate when the peak value for the energy loss is used, not the mean value. The position where the track comes closest to the beam line is considered the origin of the track.

If the tracker discovers two tracks that both come from the target, or two tracks that both come from the dump, the tracker attempts to calculate the properties of the dimuon. Both tracks are assigned the same origin, which is based on the z position during the tracking step in which the two tracks came closest to intersecting. The tracks are then recalculated using the same Kalman Filter and swimming process as before but with their origin fixed. The resulting track parameters are then used to calculate the momentum and invariant mass of the dimuon.

2.9 Production Overview

The data in this experiment is organized at the highest level by which roadset it belongs to. A handful of cuts are roadset dependent and so it is convenient to separate our data by roadset for analysis purposes. After the data is tracked the reconstructed tracks and dimuons for the entire roadset is copied into a single MySQL schema, along with spill and event level information. Hit level data is not copied into these schemas. These schemas are named `merged_roadset###_R###_V###`. The roadset number identifies which block of data is stored in the schema, while the `R###` part is the major software version number. The `V###` part is the minor software version number. The biggest changes when going to a new software version are usually in the tracking software. All of the merged productions can be found on all of the MySQL servers: `seaquel.physics.illinois.edu`, `e906-db1.fnal.gov`, `e906-db2.fnal.gov`, and `e906-db3.fnal.gov`. The version analysed in this thesis is `R005_V001` and the roadsets analysed are 57, 59, 62, 67, and 70.

All of the individual runs that make up a roadset are also stored on the MySQL servers, but each run is only on one server under most circumstances. Each run has an individual schema with the schema name `Run_#####` where `#####` is the run number. These schemas do store hit level information that would be impractical to store in the merged schemas as the table size would go over a TB.

Spill level data, which is data that is only recorded once or twice a spill, is stored in several different tables. These tables include `Spill`, `BeamDAQ`, `Beam`, `Target`, and `Scaler`. The `Spill` table contains the `liveProtons` field, which is the number of protons that struck the target that spill while the trigger was not inhibited and the DAQ was not unavailable due to reading out data. It also contains the `dataQuality` field, which is 0 if the Spill passed all of the Spill level cuts. The number in the field indicates which cuts were not passed. The `BeamDAQ` and `Beam` tables contain mostly information about the beam and the `Target` tables contain a lot of information about the Target. The `Scaler` table contains counts of how often a given event happened during a spill, such as a `Matrix1` or `NIM3` trigger. Unfortunately these tables are organized in an unintuitive manner, such as magnetic field strength information in the `Beam` table. The Analysis section of this thesis documents where each variable that is used in the data quality cuts can be found and what it means.

The event level tables are `Event` and `QIE`. The `Event` table contains information about which trigger conditions were met, and the `QIE` table contains information about the number of protons in the triggering bucket as well as the 16 buckets before and after the triggering bucket. The `QIE` table is indispensable to the rate dependence analysis. Again, all cuts on fields in these tables are documented in the Analysis section.

The `kTrack` and `kDimuon` tables are also event level tables, but they contain reconstructed information as opposed to raw data. These tables could change significantly between software versions while the other

tables wouldn't. The kTrack table contains tracks that are reconstructed by kTracker, and the kDimuon table contains reconstructed dimuons. Again, all cuts on fields in these tables are documented in the Analysis section.

Chapter 3

Monte Carlo

The Monte Carlo used in this experiment is called GMC, for Geant4 Monte Carlo. It is based off of FastMC, which is the Monte Carlo used in the previous experiment adapted to the spectrometer and beam energy of this experiment. The Monte Carlo has been used to estimate where the background noise would be concentrated during the commissioning step of this experiment. It was used in the initial development of trigger roads to estimate which roads had acceptable signal to background ratios and also to determine which roads had high value high x_T dimuons. It also is used extensively in refining kTracker to produce more accurate results, since unlike data, we know the results that tracking should arrive at when used on Monte Carlo. It is also used to develop cuts used to separate background and signal, such as the target dump separation cut. When mixed with the NIM3 random triggers from data before being run through kTracker, it provides a measure of the intensity based drop in efficiency.

3.1 Generators

In order for Geant4 to simulate anything, one or more particles have to be generated at the start of each event. The code for this resides in the `GeneratePrimaries()` function of the `PrimaryGeneratorAction.cc` file. Based on the settings given to GMC at runtime it will use either the gun generator or dimuon generator. In either case, at the end of the function at least one particle will be given to Geant4 to be tracked through the spectrometer. When a particle is given to Geant4 it needs a `particleID` (i.e. 11 for electron), a position, and a momentum.

3.1.1 Gun Generator

This should be thought of as the background generator, but the name gun generator has stuck. This is a very simple generator that creates a proton on the beam axis in front of the target with 120 GeV momentum towards the target. Unfortunately this is not a very efficient generator for simulating background as our experiment has a high rate of incoming protons but very few actually generate particles that make it through

to the detectors. A large number of instances of GMC running in parallel for long periods of time is necessary to generate a reasonable set of data.

This generator was good for estimating where the hot areas were going to be while the experiment was being commissioned. It has limitations though for estimating false positives in the background signals. While tracking particles through the spectrometer Geant4 will simulate common results of these particles colliding with materials. However Geant4 is not intended to simulate more rare interactions such as the Drell-Yan process, and some of these more rare interactions are significant enough to change the details of the results, especially since the more common interactions have difficulty getting a muon out of the iron magnet. Combined with the low efficiency of the generator it is much faster and a little more accurate to just use the NIM3 random triggers as a background sample.

3.1.2 Dimuon Generator

The dimuon generator is in one sense three generators, as it can generate Drell-Yan dimuons, J/Ψ dimuons, or Ψ' dimuons. The three options share a lot of code. If the J/Ψ or Ψ' option is chosen, the invariant mass of the dimuon is set accordingly. Otherwise the mass is picked from a flat distribution, usually from 2 to 10 GeV. x_F is also picked from a flat distribution from -1 to 1. These values are used to calculate x_b and x_t , according to equation 4.7. Equation 3.1 is used to pick p_T from a weighted distribution based on the measured p_T distribution of Drell-Yan dimuons[44]. $\cos(\theta)$ is picked from a weighted distribution according to $1 + \cos^2(\theta)$ if it is Drell-Yan or from a flat distribution if it is from a J/Ψ , and ϕ is picked from a flat distribution. The angles are the muon angles in the Collins Soper frame.

$$w(p_T) = \frac{p_T}{(1+(p_T/3)^2)^6} \quad (3.1)$$

A weight needs to be calculated for the event based on the kinematic variables in the equation. Since the invariant mass and x_f are picked from a flat distribution rather than one weighted according to the cross section, simply treating all events generated by the Monte Carlo equally will result in drastically inaccurate results. The likelier events need to have a larger weight when doing any sort of analysis. The Drell-Yan events are weighted according to equation 1.17, multiplied by the K factor. This cross section is multiplied by a value I call nucleons per area, which is the nucleon density of the target multiplied by the length of the target. The length of the target is reduced slightly to correct for beam attenuation. It is also multiplied by the beam current, which is 2e12 protons per second. This is because the Monte Carlo was designed to determine things such as number of tracks per second, number of hits per second, number of events per second etc. rather than a cross section. To correctly account for the range in mass and range in x_F of

acceptable events, it is also multiplied by $(M_{max} - M_{min})(x_{F_{max}} - x_{F_{min}})$. To determine the number of dimuons per second fitting any criteria, the weights of all events fitting this criteria are summed up, then divided by the number of events thrown by the generator.

The weighting for the J/Ψ and Ψ' are different. The p_T distribution is taken from *Measurement of J/Ψ and Ψ' production in 800 GeV/c proton-gold collisions*[31]. The cross section is also taken from the same source and the branching ratio into $\mu^+\mu^-$ from *Particle Physics Booklet*[45]. They also have the same modifications by nucleons per area and beam current, and the rates of dimuons per second are calculated in the same fashion.

3.2 Physics List

Geant4 provides several prebuilt physics lists that contain a best guess at what physics experiments might need to include in their simulations. Originally it was our intent to build a physics list from processes and particles provided by Geant4 instead of using one of the prebuilt lists. The first versions of GMC did use such a list compiled by my predecessor and I had hoped that the gun generator might gain some performance by not including processes that were unnecessary. When we needed to upgrade Geant4 though it became impossible to ensure that such a user built list had everything we needed due to undocumented changes in the names of several processes and other poor Geant4 documentation. Using the internet[46] for guidance it appeared that the FTTP_BERT physics list was a good default choice for our energies. We went with FTTP_BERT_EMX, although in retrospect the tweaking to the default EM settings by including the .EMX was completely unnecessary. We didn't see the need to include any processes in addition to the FTTP_BERT_EMX list.

3.3 Geometry

There are two parts to the geometry of the experiment that is implemented in GMC. The first part contains all the information needed to be given to GMC to simulate the movement of particles through our spectrometer. Geant4 uses several objects to contain the information used in simulating the spectrometer. The G4Material object contains the information Geant4 needs to simulate a material, which is its density and the list of elements in the material and the percent of the material's mass each element makes up. The G4VSolid objects contain information about a shape and its dimensions. The G4LogicalVolume object combines a solid with a material and includes the information of whether or not the volume is a detector. Each logical volume is attached to one or more physical volumes which contain the position and orientation of each

piece of the spectrometer[47]. The magnetic fields are also part of the information given to Geant4 for the simulations. The magnetic field files for FMag and KMag are grids of x, y, and z positions with x, y, and z field strengths. The strength at any given point is determined by interpolating between the eight closest vertices of the grid, which form a cube around the point.

The MySQL servers all have a copy of the latest geometry files in which this information is kept. The names of the geometry schemas are of the form `geometry_G##_run#`. There is a separate geometry for each run as detectors have been added, moved, and replaced between runs. The geometry schemas have required constant updates as bugs are fixed and more precise detector survey and alignment information is available; the number after G is the revision number of the geometry. Old versions of the geometry are kept available so that in progress studies can be finished without losing reproducibility. These schemas have several tables, one each for the material, logical volume, and physical volume objects, and several for the different variations of solid objects (cylinders, rectangular prisms, etc.). There are also a couple of tables for the magnetic fields, although these are typically loaded from tab separated ASCII files instead. These files are located in the `geometry/magnetic_fields/` folder of the SeaQuest Software Distribution.

The other part of the geometry is the part that doesn't get loaded into the Geant4 part of the simulation but are still loaded into GMC to help interpret the information that Geant4 returns. The Planes table in the MySQL geometry schemas connects all of the Physical Volumes used in the simulation to the actual planes of the experiment. This table holds the information of how many detector planes are within each Physical Volume, the coordinates of the center of the plane, its rotation, how many wires are in the plane, what the spacing is between wires, the rotation of the wires with respect to the plane, and how much the center wire is offset from the center of the chamber. For the hodoscopes it contains how much the paddles overlap each other. The positions and rotations of the planes in this table are determined by surveys done by Fermilab. These positions and rotations are used as input into calculating an even finer alignment by tracking results from special data taking runs where KMag was turned off. Such special runs have straight tracks through all of the detectors which makes alignment much easier. These alignment results are stored in the PlaneOffsets table in the MySQL geometry schemas. The Planes and PlaneOffsets tables combined allow GMC to calculate which wires, paddles, and tubes are struck when a simulated particle passes through a simulated detector, as well as calculating a drift distance. Other relevant detector information is stored in text files in `/GMC/code/sqlTables/` which are uploaded to the GMC output schema at the beginning of the run. The `hodoInfo.tsv` and `chamberInfo.tsv` tables link each wire, paddle, and tube to a `rocID`, `boardID`, and `channelID`. These IDs identify which channel of the DAQ electronics are connected to which detector element. The `RT.tsv` table contains the information which maps the drift distance to drift time for our wire

chambers and prop tubes.

3.4 Output

All of the output of GMC is put into a MySQL database. The amount of information uploaded for a single instance of GMC is low compared to its run time, so it is easily possible for many parallel instances of GMC to be simultaneously running and uploading information to a single MySQL server. For each table that GMC uploads, it packages together many rows into a single upload query, and then uploads it in one query once a threshold is reached before starting on a new query. This avoids the traffic jam of tens of GB being uploaded at once, which is undesirable. It also avoids a different possible traffic jam of bogging down the MySQL server in the massive overhead generated by putting each uploaded row into a separate query.

Some of the tables are Monte Carlo truth tables and are prefaced by an m, for tables such as mHit or mTrack. These tables are not used as input to kTracker, but are used to compare the output of kTracker to the truth values to see where adjustments in the tracking algorithm are needed. For example, the mHit table will contain the momentum of the particle when it struck the detector, information that is not available in real data. GMC will also contain other tables, such as Hit, which mimic the data structure of real data and lack this truth data. These tables are the ones used as input by kTracker.

One of the most important tables is the mRun table, which has a single row for each parallel instance of GMC in that production. In this row all of the settings used in that run are detailed, such as which PDF set was used, magnetic field strengths as a fraction of the field files, kinematic ranges for x and mass, and a variety of other settings.

The other important truth tables are the mTrack, mDimuon, and mHit tables. The mTrack table contains the tracks momentum and position at the origin and the first and third detector stations, its particleID, which hodoscope, wire chamber, and prop tube stations it hit, and if it isn't a primary particle it contains the trackIDs of the parent and the Geant4 process that created it. The mDimuon table contains the kinematics of the dimuon, such as invariant mass, x_F , x_B , x_T , and its Collins-Soper angles. It contains the position and momentum it had at its origin. It also contains trackIDs for the positive and negative muons. It also contains the weight for the dimuon. The mHit tables contain the position and momentum of the particle where it intersected the detector, its true drift time, and which track it belongs to.

Most of the non-truth tables are provided by kTracker, which provide results in kTrack and kDimuon to compare to the Monte Carlo results. The Hit table, however, is provided by GMC, and contains only information that would be found in the real data. In addition, kTracker has a function that will make

random changes to the drift time and distance of each Hit entry to match the uncertainties generated by the finite resolution of our detectors, while mHit keeps the true information.

The output name of the MySQL productions that determine this information are as `mc_[generator]_[target]_M###_S###`. The generator is a name like drellyan, jpsi, or gun to indicate which generator is used. The target is the name of which target was used, like C for carbon. If the dimuons have their origin in the beam dump then it says dump instead. The M number is the revision number for GMC, and there is a table on the Fermilab Redmine page for the Seaquest Monte Carlo that links that version number to the github hash for that commit, as well as supplying some small comments on what was changed. The S number is used to distinguish between multiple GMC productions that have different settings but would otherwise have the same name.

3.5 Running GMC

Creating a GMC production requires the use of a couple of helper programs. First, the TableLoader table is run, which takes a geometry file and some tab separated text files and processes them into tables used by GMC in its MySQL schema. This takes time on the order of several minutes. Then, the GMC program itself is run. It takes a little less than a day to generate about 3,000 dimuons in the spectrometer acceptance and or about a single spill's worth of protons. The MySQL servers can handle a few hundred parallel GMC productions, give or take based on what else is using the server. Each parallel instance of GMC generates separate tables, a collection of parallel instances will generate tables named Event_1, Event_2, Event_3, etc. After all the GMC instances finish running, the TableMerger program should be run. This merges the tables together so there is only one Event table, one mDimuon table, etc. It also removes any rows from any run that did not finish running and creates the indices on the finished tables. This takes about 2 days to complete. TableLoader and TableMerger both give a list of possible run time arguments with the -h argument. Both programs will need a MySQL login, MySQL password, and GMC schema name, and TableLoader will need a geometry schema name.

The easiest way to run a single instance of GMC is to give it a macro file at runtime with the -m argument, such as "GMC -m file.mac". The macro file is simple a text file with each command on a separate line in order. The easiest way to run many instances is on the Fermilab seaquestgpvm machines, using the runGMC.py program. "runGMC.py -h" will list the options for running it. When run, it will run TableLoader first before submitting the GMC runs as jobs to Fermilab's grid computing system. TableMerger still has to be run separately by the user once all the jobs have finished.

3.5.1 Commands

A full list of the commands is on the wiki on the Fermilab Redmine page for the Seaquest Monte Carlo. The important commands are listed in table 3.1.

Command	Argument	Explanation
/control/server	string	Name of the MySQL server to write the output to.
/control/login	string	MySQL login
/control/password	string	MySQL password
/control/outputFile	string	Name of the MySQL schema to write the output to.
/control/geometrySchema	string	Name of the MySQL schema to fetch geometry info from.
/set/eventGenType	enum(gun, dimuon)	Which generator to use.
/set/dimuonSource	enum(DY, JPsi, Psi_Prime)	Process that generates dimuons.
/set/eventPos	enum(target, dump, upstream, all)	Location of dimuon origin.
/set/target	int	Sets the target material.
/set/FMagMultiplier	double	Multiplies the field in the magnetic field file for FMag. Important for simulating a flipped polarity. The values used are typically not exactly one and are based on the magnet calibration.
/set/KMagMultiplier	double	As above, but for KMag.
/set/recordMethod	enum(hits, dimuon-Full, dimuonOnly)	The hits option makes it so tracks that cause at least one hit are recorded. The dimuonFull option only records events where both muons are within spectrometer acceptance. The dimuonOnly option records no tracks, only initial kinematics for all dimuons.
/control/initialize	none	Initializes some Geant4 objects. Required, second to last command.
/run/beamOn	int	How many protons or dimuons to generate. Required, last command.

Table 3.1: Table of GMC commands.

3.6 GMC Improvements

When I joined this experiment, I was tasked with running, maintaining, and improving GMC, and getting it to work on our systems. While I did not write the initial code, it has gone through so many iterations that I have written the majority of the code that currently makes up the program.

One of the first major changes that was made was changing the geometry from hard coded instances of each detector to loading it from MySQL schemas. This made the geometry much more human readable and the code much more manageable. It is a good rule of thumb to store information used in a program in

input files outside of the code so that these parameters can be edited easily by people unfamiliar with the code and so that multiple input options can be maintained without bloating the code. It also lets programs analysing the output of GMC understand the geometry, it would be completely impractical to have such programs parse the GMC code for those parameters.

Another early major change was the digitization of the hits. Early output of GMC just had a position and detector name of each hit, and the position was a general position and not relative to the center of the detector. By loading in survey information for each detector I could find the intersection between the particle's line and the plane of the detector[48]. I could then get the relative position of the hit in the plane, and calculate which wire, paddle, or tube was struck and the drift distance. With the association of DAQ channelIDs, drift times, detector elementIDs, and drift distances to each hit I was able to provide a data format mimicking the experiment's data format so that analysis programs could easily be run on both real data and simulated data.

Another problem I worked on was the unexpectedly small number of hits in the edges of the detectors in the x direction in gun generator mode. We were expecting the magnets to push most of these particles to the edges so it was surprising to see two peaks closer to the middle of the detector, one on each side. Eventually I found that the culprit was an optimization cut that tried to make the inefficient gun generator more efficient. It cut particles that were travelling at a large angle under the presumption that these particles would miss the detectors. I removed this cut and the simulation matched what we expected, but then the run speed slowed to a crawl. I changed the cut to remove particles moving backwards through the magnet, and this gave accurate results at a slower but manageable run speed.

Another project involving GMC was cross checking it against FastMC, the Monte Carlo from the previous experiment which was written in Fortran, modified to use SeaQuest's beam energy, and only used rough calculations for tracking particles through materials. The dimuon generator code in GMC is a C++ translation of the Fortran code used in a section of FastMC. While the tracking in Geant4 is more precise, FastMC should be just as accurate in generating the initial dimuon kinematics and weighting. However, the output from FastMC and GMC just wasn't matching up. We found a few typos but could not track down where the differences were coming from. The culprit turned out to be different standards of units in Geant4 and the PDFlib libraries. In Geant4, the default unit is MeV, but PDFLib was expecting all arguments for energy to be in GeV. This resulted in all energy parameters being passed to PDFLib to be multiplied by 1,000 compared to what they should have been, which caused the PDFs to return much different results than we expected.

Another improvement I made to GMC was replacing PDFlib with LHAPDF. LHAPDF contains more

recent PDF sets and is also available in C++, while PDFlib is in Fortran and required complications in coding and the makefile to have the C++ and Fortran interface which made it harder to consistently compile in multiple environments. This improvement also made things more human readable with the all of the code involving Drell-Yan physics being in the same place.

3.7 MySQL Usage

Using a MySQL database to store much of our data, both simulated and real, is much less common than using ROOT. There were both advantages and disadvantages to this approach, and I believe that a relational database such as MySQL can have a strong place in physics analysis while not being the answer for everything. Also, like any software tool, knowledge of how to use it best is important.

The largest problem with using MySQL for everything is that it isn't efficient for anything that requires reading in every single row. Above I mentioned that while the magnetic fields can be read in from the MySQL database, they are almost always read in through the tab separated ASCII files. This is because reading in the data through the text files is several times faster. For tracking, the hit data(real, not simulated) is available in ROOT file format as well as MySQL format, and it was found to be much faster to read in the data from ROOT. In this case every hit needed to be used as input into the tracking program.

Another problem is that MySQL can also take longer to write data. Data coming in from hundreds of programs running in parallel on grid computing can bog down a MySQL server. This is especially true if the tables have indices enabled as data is being written to them. If they are disabled while being written to and enabled after, the building of the indices can take even days depending on the size of data.

Another problem that is less of an issue with today's hard drive capacities is the extra room that is taken up by MySQL databases compared to the data structures of a library such as ROOT. MySQL databases are larger even without indices on the fields, although in practice there will almost always be an index on at least one field. Typical tables will have multiple indices and these indices can take up space comparable to the raw data. Our data storage has reached the level of Terabytes, and space has sometimes become a bit tight on our MySQL servers.

One of the great things about MySQL is how quickly and easily you can fetch information that requires cutting on some condition. If you cut on an indexed field it greatly reduces the amount of data that has to be read. Queries are also quicker than writing a program to loop through data to get what you want, when you need to ask a lot of questions about the data these savings in human time add up. For example, a flat file is better for reading in the entire magnetic field, but if you wanted to ask MySQL what the

field in the y direction is integrated over a line through the beam axis, you could just type in "SELECT SUM(By)*(MAX(z) - MIN(z))/(COUNT(1) - 1) FROM FMag WHERE x = 0 AND y = 0" and the answer pops up on your screen, while retrieving the information from a flat file would take longer.

Another advantage of MySQL is that it is well documented and easy to learn. The official documentation is detailed and extensive and there are a ton of articles to be found online giving advice on optimizing performance and if you have an issue you can almost certainly find a question on Stack Exchange where someone else has had your problem before.

Yet another advantage is that MySQL is supported by almost all programming languages. There are code libraries for interfacing between MySQL and C++, python, java, ruby, and others. Many programs, such as ROOT, have an interface for MySQL. Whatever someone prefers to use, odds are they can connect to MySQL with it without much fuss.

In order to use MySQL optimally both the person managing the database and the person writing the queries need to know good practices with indices. The person managing the database needs to know which fields should be indexed to save query time, and which fields would do nothing other than slow writing time and bloat data size if indexed. The person writing the queries needs to know how to check which fields are indexed, which is quick and easy, and also how to write a query to take advantage of these indices. Also, anyone who reads from or writes to the database using a program should absolutely not read or write a single row at a time, as there is overhead in network time for every query that becomes significant if one tries to submit stupidly large numbers of queries per second. Learning how to write MySQL queries is similar to learning how to write a programming language, you won't get much out of MySQL if you don't know how to do a JOIN like you won't get much out of C++ if you don't know how to write a for loop. Often the penalty for a poor query in MySQL isn't an error message from bad syntax, but a query that runs for orders of magnitude longer than necessary.

Chapter 4

Analysis

There are several steps in the extraction of $\sigma_{pd}/2\sigma_{pp}$ from the data. First a lot of cuts have to be made on the spill data and the reconstructed dimuons to ensure that the data is accurate. There are several separate rate dependent corrections to be made based on the tracking efficiency, background subtraction, and miscellaneous rate dependence. There is also a correction to be made for 1H contamination in the 2H target. Once $\sigma_{pd}/2\sigma_{pp}$ is known then the value of \bar{d}/\bar{u} can be calculated through an iterative procedure.

4.1 Kinematic Variables

Before we even start talking about cuts we need to explicitly define how we calculate the quantities we are cutting on. For most variables it is straightforward, but for Bjorken x and Feynmann x we need to be clear on how we calculate them since there are multiple equations that can be used. The calculation of Bjorken x in particular is far from straightforward.

Feynmann x , or x_F is defined as $q_{\parallel}/q_{\parallel max}$, where q_{\parallel} is the longitudinal momentum of a particle. The particle in our case is the virtual photon in the Drell-Yan process. x_F is sometimes written as $2q_{\parallel}/\sqrt{s}$, but this ignores the mass of the virtual photon, which should be taken into account. We choose to use equation 4.1 as our definition of x_F , which is the other common form of x_F .

$$x_F = \frac{2q_{\parallel}}{\sqrt{s-M^2}/\sqrt{s}} \quad (4.1)$$

Bjorken x , which I will often shorten to just x , is commonly defined as the ratio between the parton's momentum and its proton's momentum when boosted longitudinally to an infinite momentum frame. If we boost something with momentum \vec{p} to its infinite momentum frame it will have momentum \vec{p}' . $p'_{\parallel} = \gamma(p_{\parallel} + \beta p_0)$, so the momentum fraction x of a parton of momentum \vec{k} and its proton of momentum \vec{P} is then equation 4.3.

$$x = \frac{\gamma(k_{\parallel} + \beta k_0)}{\gamma(P_{\parallel} + \beta P_0)} \quad (4.2)$$

Infinite momentum frame, $\beta = 1$.

$$x = \frac{(k_{\parallel} + k_0)}{(P_{\parallel} + P_0)} \quad (4.3)$$

We can not measure the longitudinal momentum of a single parton involved in the Drell-Yan reaction, so we can not calculate x directly. We have to estimate the value of x by using one of several formulas, equations 4.4 through 4.7, which assume that the mass and p_{\perp} of the parton are negligibly small.

$$x_A = \frac{Q^2}{2\vec{P}_A \cdot \vec{q}} \quad (4.4)$$

$$x = \sqrt{\tau + \frac{x_F^2}{4}} \pm \frac{x_F}{2} \quad (4.5)$$

$$x = \sqrt{\tau} e^{\pm y} \quad (4.6)$$

$$x_A = \frac{\vec{P}_B \cdot \vec{q}}{\vec{P}_B \cdot \vec{P}_A} \quad (4.7)$$

τ is equal to M^2/s , and y is the rapidity equal to $0.5 \ln((q_0 + q_{\parallel})/(q_0 - q_{\parallel}))$. If a formula has a \pm , then the $+$ is for calculating x for the beam and the $-$ is for calculating x for the target. The fourth definition, equation 4.7, uses the momentum of both protons in the equation so they get A and B subscripts to tell them apart. Clearly this last calculation can not be used in certain experiments, such as DIS.

As an example I will demonstrate how the first example reduces to x in this approximation. I will do this for the beam parton and work in the center of mass frame. Using k for the beam parton momentum and j for the target parton momentum,

$$x = \frac{Q^2}{2\vec{P} \cdot \vec{q}} \quad (4.8)$$

$$Q^2 = k_0^2 + j_0^2 + 2k \cdot j \quad (4.9)$$

$$Q^2 = 2(k_0 j_0 - k_{\parallel} j_{\parallel}) \quad (4.10)$$

k_0 , j_0 , and k_{\parallel} are all positive, but j_{\parallel} is negative. Where parton mass and p_T are zero k_0 is equal in

magnitude to k_{\parallel} .

$$Q^2 = -4k_{\parallel}j_{\parallel} \quad (4.11)$$

Now for the denominator.

$$2\vec{P} \cdot \vec{q} = 2P_0q_0 - 2P_{\parallel}q_{\parallel} \quad (4.12)$$

$$2\vec{P} \cdot \vec{q} = 2P_0(k_{\parallel} - j_{\parallel}) - 2P_{\parallel}(k_{\parallel} + j_{\parallel}) \quad (4.13)$$

$$2\vec{P} \cdot \vec{q} = 2P_0\left(\left(1 - \frac{P_{\parallel}}{P_0}\right)k_{\parallel} - \left(1 + \frac{P_{\parallel}}{P_0}\right)j_{\parallel}\right) \quad (4.14)$$

$$2\vec{P} \cdot \vec{q} = -2P_0\left(1 + \frac{P_{\parallel}}{P_0}\right)j_{\parallel}\left(1 - \left(1 - \frac{P_{\parallel}}{P_0}\right)\frac{k_{\parallel}}{j_{\parallel}}\right) \quad (4.15)$$

Putting it together.

$$\frac{Q^2}{2\vec{P} \cdot \vec{q}} = \frac{-4k_{\parallel}j_{\parallel}}{-2P_0\left(1 + \frac{P_{\parallel}}{P_0}\right)j_{\parallel}\left(1 - \left(1 - \frac{P_{\parallel}}{P_0}\right)\frac{k_{\parallel}}{j_{\parallel}}\right)} \quad (4.16)$$

$$\frac{Q^2}{2\vec{P} \cdot \vec{q}} = \frac{2k_{\parallel}}{(P_0 + P_{\parallel})\left(1 - \left(1 - \frac{P_{\parallel}}{P_0}\right)\frac{k_{\parallel}}{j_{\parallel}}\right)} \quad (4.17)$$

Using the approximation $\frac{1}{1-z} = 1 + z$ where $z \ll 1$, and the fact that $1 - \frac{P_{\parallel}}{P_0}$ is very close to 0.

$$\frac{Q^2}{2\vec{P} \cdot \vec{q}} = \frac{2k_{\parallel}}{P_0 + P_{\parallel}}\left(1 + \left(1 - \frac{P_{\parallel}}{P_0}\right)\frac{k_{\parallel}}{j_{\parallel}}\right) \quad (4.18)$$

$$\frac{Q^2}{2\vec{P} \cdot \vec{q}} = \frac{k_0 + k_{\parallel}}{P_0 + P_{\parallel}}\left(1 + \frac{P_0 - P_{\parallel}}{P_0}\frac{k_{\parallel}}{j_{\parallel}}\right) \quad (4.19)$$

$$\frac{Q^2}{2\vec{P} \cdot \vec{q}} = x\left(1 + \frac{P_0 - P_{\parallel}}{P_0}\frac{k_{\parallel}}{j_{\parallel}}\right) \quad (4.20)$$

$P_0 \approx P_{\parallel}$, and if one treats the difference as negligible then equation 4.20 becomes equation 4.3. Now this is almost equal to the momentum fraction x , as $P_0 \approx P_{\parallel}$, but the equation can be improved. If instead of using the proton's 4 momentum, we used a different vector that is similar, we could end up with an

equation exactly equal to x when ignoring the parton p_T^2 terms. This new vector, \vec{P}' , would need to have $P'_0 + P'_\parallel = P_0 + P_\parallel$ so that the $(k_0 + k_\parallel)/(P_0 + P_\parallel)$ part of equation 4.19 is properly equal to x . Also, $P'_0 = P'_\parallel$ so that the $\frac{P_0 - P_\parallel}{P_0} \frac{k_\parallel}{j_\parallel}$ in equation 4.20 reduces to 0. The vector $\vec{P}' = (P', 0, 0, P')$, where $P' = (P_0 + P_\parallel)/2$, meets both these conditions. So I modified equation 4.4 to use \vec{P}' instead of \vec{P} . This changes equation 4.20 to equation 4.22, giving us a more accurate way of calculating x .

$$\frac{Q^2}{2\vec{P}' \cdot \vec{q}} = x \left(1 + \frac{0}{P_0} \frac{k_\parallel}{j_\parallel} \right) \quad (4.21)$$

$$\frac{Q^2}{2\vec{P}' \cdot \vec{q}} = x \quad (4.22)$$

After working out the other formulas in equations 4.5 through 4.7 I also replaced all instances of τ with $\sqrt{M^2/4P'^2}$, all instances of x_F with q_\parallel/P' , and all other instances of \vec{P} with \vec{P}' .

If the parton mass and p_T are equal to zero then these new formulas are equal to one another. However, in our data, p_\perp of the parton is not always negligibly small and the choice of formula can actually have a significant effect on the resulting calculation of x . It is still negligible at $p_T < 1\text{GeV}$, with the differences in the various definitions being in the range of about 0.001 and 0.002 for x_T . At high p_T the differences between equations 4.4 and 4.7 were the largest, with the difference being about 0.02 for x_T at p_T between 1.5 and 2 GeV, which is enough of a change to shift results to another bin in x at low x . The differences in x_B are much more pronounced, being about 0.07 at p_T between 1.5 and 2 GeV. This is significant enough that some care and attention to the choice of formula is deserved.

So in order to figure out which formula for x should be used when the parton momentum is not known and the parton p_\perp is not negligible, I tried write the formulas for x out to quadratic terms in p_\perp . I used approximations with the assumption that $p_\perp^2 \ll p_\parallel^2$ and that quark mass = 0. For each formula that approximates x I algebraically transformed the formula into a part equal to the right side of equation 4.3 plus some p_\perp^2 terms. I then estimated which formula would have the smallest p_\perp^2 terms in our kinematic regime. As an example, I will derive the result for equation 4.4 for the beam parton, starting with the Q^2 portion,

$$Q^2 = k \cdot k + j \cdot j + 2k \cdot j \quad (4.23)$$

$$Q^2 = 2k_0 j_0 - 2k_\perp \cdot j_\perp - 2k_\parallel j_\parallel \quad (4.24)$$

$$k_0 = \sqrt{k_{\parallel}^2 + k_{\perp}^2} \quad (4.25)$$

$$k_0 = k_{\parallel} \sqrt{1 + k_{\perp}^2/k_{\parallel}^2} \quad (4.26)$$

Using the approximation $\sqrt{1+z} \approx 1 + \frac{z}{2}$ where $z \ll 1$.

$$k_0 = k_{\parallel} \left(1 + \frac{k_{\perp}^2}{2k_{\parallel}^2}\right) \quad (4.27)$$

$$k_0 = k_{\parallel} + \frac{k_{\perp}^2}{2k_{\parallel}} \quad (4.28)$$

Since $j_{\parallel} < 0$

$$j_0 = -j_{\parallel} - \frac{j_{\perp}^2}{2j_{\parallel}} \quad (4.29)$$

$$Q^2 = -2\left(k_{\parallel} + \frac{k_{\perp}^2}{2k_{\parallel}}\right)\left(j_{\parallel} + \frac{j_{\perp}^2}{2j_{\parallel}}\right) - 2k_{\perp} \cdot j_{\perp} - 2k_{\parallel}j_{\parallel} \quad (4.30)$$

Dropping terms of p_{\perp}^4

$$Q^2 = -k_{\parallel} \frac{j_{\perp}^2}{j_{\parallel}} - j_{\parallel} \frac{k_{\perp}^2}{k_{\parallel}} - 2k_{\perp} \cdot j_{\perp} - 4k_{\parallel}j_{\parallel} \quad (4.31)$$

$$Q^2 = -4k_{\parallel}j_{\parallel} \left(1 + \frac{k_{\parallel} \cdot j_{\parallel}}{2k_{\parallel}j_{\parallel}} + \frac{k_{\perp}^2}{4k_{\parallel}^2} + \frac{j_{\perp}^2}{4j_{\parallel}^2}\right) \quad (4.32)$$

Now for the $2\vec{P}' \cdot q$ portion.

$$2\vec{P}' \cdot q = 2P'(k_0 + j_0 - k_{\parallel} - j_{\parallel}) \quad (4.33)$$

$$2\vec{P}' \cdot q = 2P' \left(\frac{k_{\perp}^2}{2k_{\parallel}} - 2j_{\parallel} - \frac{j_{\perp}^2}{2j_{\parallel}}\right) \quad (4.34)$$

$$2\vec{P}' \cdot q = -4P'j_{\parallel} \left(1 - \frac{k_{\perp}^2}{4k_{\parallel}j_{\parallel}} + \frac{j_{\perp}^2}{4j_{\parallel}^2}\right) \quad (4.35)$$

Using the approximation $\frac{1}{1-z} = 1 + z$ where $z \ll 1$.

$$\frac{Q^2}{2\vec{P}' \cdot q} = \frac{k_{\parallel}}{P'} \left(1 + \frac{k_{\perp} \cdot j_{\perp}}{2k_{\parallel} j_{\parallel}} + \frac{k_{\perp}^2}{4k_{\parallel}^2} + \frac{j_{\perp}^2}{4j_{\parallel}^2} \right) \left(1 + \frac{k_{\perp}^2}{4k_{\parallel} j_{\parallel}} - \frac{j_{\perp}^2}{4j_{\parallel}^2} \right) \quad (4.36)$$

Dropping p_{\perp}^4 terms

$$\frac{Q^2}{2\vec{P}' \cdot q} = \frac{k_{\parallel}}{P'} \left(1 + \frac{k_{\perp}^2}{4k_{\parallel} j_{\parallel}} + \frac{k_{\perp} \cdot j_{\perp}}{2k_{\parallel} j_{\parallel}} + \frac{k_{\perp}^2}{4k_{\parallel}^2} \right) \quad (4.37)$$

$$\frac{Q^2}{2\vec{P}' \cdot q} = \frac{1}{P'} \left(\frac{k_{\parallel} + k_0 + k_{\parallel} - k_0}{2} + \frac{k_{\perp}^2}{4j_{\parallel}} + \frac{k_{\perp} \cdot j_{\perp}}{2j_{\parallel}} + \frac{k_{\perp}^2}{4k_{\parallel}} \right) \quad (4.38)$$

$$\frac{Q^2}{2\vec{P}' \cdot q} = x + \frac{1}{P'} \left(\frac{k_{\parallel} - k_0}{2} + \frac{k_{\perp}^2}{4j_{\parallel}} + \frac{k_{\perp} \cdot j_{\perp}}{2j_{\parallel}} + \frac{k_{\perp}^2}{4k_{\parallel}} \right) \quad (4.39)$$

$$\frac{Q^2}{2\vec{P}' \cdot q} = x + \frac{1}{P'} \left(\frac{k_{\perp}^2}{4j_{\parallel}} + \frac{k_{\perp} \cdot j_{\perp}}{2j_{\parallel}} \right) \quad (4.40)$$

The results for the other formulas can be derived in a similar manner, and they all have different results when p_{\perp}^2 terms are included. The results can be found in table 4.1.

Formula	End result
$\frac{Q^2}{\vec{P}' \cdot q}$	$x + \frac{1}{P'} \left(\frac{k_{\perp}^2}{4j_{\parallel}} + \frac{k_{\perp} \cdot j_{\perp}}{2j_{\parallel}} \right)$
$\sqrt{\tau + \frac{x_F^2}{4}} \pm \frac{x_F}{2}$	$x - \frac{1}{P'} \left(\frac{k_{\perp} \cdot j_{\perp}}{2(k_{\parallel} - j_{\parallel})} + \frac{j_{\perp}^2 k_{\parallel}}{4j_{\parallel}(k_{\parallel} - j_{\parallel})} + \frac{k_{\perp}^2}{4(k_{\parallel} - j_{\parallel})} \right)$
$\sqrt{\tau} e^{\pm y}$	$x + \frac{1}{P'} \left(\frac{k_{\perp} \cdot j_{\perp}}{4j_{\parallel}} - \frac{j_{\perp}^2}{8j_{\parallel}} + \frac{k_{\perp}^2}{8j_{\parallel}} \right)$
$\frac{\vec{P}'_j \cdot q}{\vec{P}'_j \cdot \vec{P}'_k}$	$x - \frac{j_{\perp}^2}{4P' j_{\parallel}}$

Table 4.1: List of approximation formulas for Bjorken x to quadratic terms in parton p_{\perp} . Do note that k_{\parallel} and j_{\parallel} have opposite signs.

Most of the terms have j_{\parallel} in the denominator, which means the worst inaccuracies are going to be in calculating x of the beam (x_B) at low x of the target (x_T). In this region, $\frac{\vec{P}'_j \cdot q}{\vec{P}'_j \cdot \vec{P}'_k}$ and $\sqrt{\tau + \frac{x_F^2}{4}} \pm \frac{x_F}{2}$ are going to have the best results and are almost equal to each other. We decided to use $\frac{\vec{P}'_j \cdot q}{\vec{P}'_j \cdot \vec{P}'_k}$ to calculate x in our experiment because it looked slightly more accurate in other kinematic regions.

4.2 Cuts

There are two levels of cuts in this analysis. The first level is the spill level. Spills failing these cuts have all the events in the spill cut and the protons are cut from the live proton count as well. Tables involved in these cuts are the Spill, Beam, BeamDAQ, Target, and Scaler tables. The second level is the event level. Tables for this level of cuts are the kTrack, kDimuon, Event, and QIE tables.

4.2.1 Spill Level

The spill level cuts ensure that the data taking conditions were both normal and accurately recorded. Conditions such as very low beam intensity, an anomalous magnet current, or an unrealistically high duty factor can all cause the spill to be cut. These cuts are all found in table 4.2. There are also several spill ranges that have known problems that make them unsuitable for analysis, these ranges and the reason for exclusion can be found in table 4.3. The number of spills left after each stage of cuts can be found in table 4.4.

A type of cut that can be found for almost every table is the no duplicates cut. Some tables, such as the Spill table, should only have one entry per spillID. If there are multiple rows then it is a sign that something has gone wrong with the data recording, and also it is not possible to tell which of the recorded rows is correct. Some tables, such as the Beam table, record values in multiple rows for each spill. The name field contains a string that says what value is being recorded, such as beam intensity if the name is S:G2SEM. So for a given spillID there would be one row for the S:G2SEM value, one row for the F:NM4AN value, and one row each for the other values, but there should be no duplicates of both spillID and a name field, such as two S:G2SEM rows for the same spillID. The Scaler table is similar but has two rows for each value, a beginning of spill (BOS) value and an end of spill (EOS) value, and the spillType field tells which row is which.

The targetPos value in the spill table contains an integer that corresponds to the target for that spill. We have seven targets and the IDs range from 1 to 7, so if the value is outside that range the spill information is obviously incorrect. The other cut on the spill table, spillID \neq 0, gets rid of spills that were not assigned a spillID due to incomplete DAQ information.

The only cut on the Target table is that the target ID it records has to match the target ID from the spill table. This is just to make sure the data is consistent.

The Scaler table cuts on EOS values for TSgo, acceptedMatrix1, and afterInhMatrix1 ensure that the total number of triggers, the total number of matrix 1 triggers, and the number of matrix 1 triggers that weren't during dead time are a reasonable value, respectively. The cut ranges are wide and contain all data

Table	Value	Roadsets	Good range
Spill	targetPos	all	[1, 7]
	spillID	all	$\neq 0$
	spillID	all	no duplicates
Target	TARGPOS_CONTROL	all	Spill table targetPos
	spillID, name	all	no duplicates
Scaler	TSgo, EOS	57, 59	[1,000, 8,000]
		62, 67, 70	[100, 6,000]
	acceptedMatrix1, EOS	57, 59	[1e3, 8e3]
		62, 67, 70	[100, 6e3]
	acceptedMatrix1, BOS	all	Entry exists
	afterInhMatrix1, EOS	57, 59	[1e3, 3e4]
		62, 67, 70	[100, 1e4]
acceptedMatrix1/afterInhMatrix1, EOS	57, 59	[0.2, 0.9]	
	62, 67, 70	[0.2, 1.05]	
	spillID, scalerName, spillType	all	no duplicates
Beam	S:G2SEM	all	[2e12, 1e13]
	F:NM4AN	all	> 1000
	spillID, name	all	no duplicates
BeamDAQ	QIESum	all	[4e10, 1e12]
	trigger_sum_no_inhibit	all	[4e9, 1e11]
	inhibit_block_sum	57, 59	[4e9, 1e11]
		62, 67, 70	[4e9, 2e11]
	dutyfactor53MHz	57, 59	[15, 60]
62, 67, 70		[10, 60]	
	spillID	all	no duplicates
kTrack	# of rows	all	> 0

Table 4.2: List of Spill Quality cuts

where the beam was normal and the trigger and DAQ were functioning properly. There is a cut that requires there to be a beginning of spill entry for `acceptedMatrix1` that is a check to make sure that data was being recorded at the beginning of the spill. Partial spills can not be correctly normalized by live proton count so it is important to exclude them from the data.

The `S:G2SEM` value in the Beam table is a measure of beam intensity. If it is too low then the beam was probably not active. Values higher than the cut off indicate a problem recording beam intensity. The `F:NM4AN` value measures the current powering FMag and ensures that the magnet was on during the spill.

The `QIEsum` cut in the BeamDAQ table is a second cut on a measure of beam intensity and also cuts out many spills where the QIE wasn't reading out properly. The `trigger_sum_no_inhibit`, `inhibit_block_sum`, and `dutyFactor53MHz` cuts all try to ensure that the quality of the beam was normal. The quality of the beam has a strong effect on how many events can be reconstructed and thus spills with very bad beam quality should be excluded.

The cut on the `kTrack` table is to make sure that reconstruction has been run on the spill in question. Since a typical spill contains over 1,000 `kTracks`, any spill without a single `kTrack` means that reconstruction has not been run on those events.

First spillID	Last spillID	Reason
303215	310954	QIE readout errors
371870	376533	Trigger timing shift
378366	379333	Trigger timing shift
394287	409540	Data Set 3 commissioning period
394287	414555	Deuterium flask filled with LH2
416207	424180	Manual target control
482574	484924	Magnet flipped compared to rest of roadset 62
526201	526364	Bad QIE inhibit timing
551030	610059	Middle of roadset 67 reconstruction issues
581369	582460	KMag off
675814	684041	Gas flow problems in station 1
684663	689443	D3p has wrong in time window
676242	685765	Trigger timing shift

Table 4.3: List of bad spill ranges. The problems with the middle of roadset 67 have been solved and will not be excluded from future analysis.

Some of the bad `spillID` ranges in table 4.3 are straightforward, but some are not. The `QIE` readout errors indicate a data taking range where a large number of `QIE` outputs had zeros in them instead of the correct value. This makes the `QIEsum` and live proton counts for these spill ranges incorrect. Trigger timing shifts cause the in time window for the drift chambers and prop tubes to shift relative to the trigger, causing some legitimate hits to be outside the in time window and not recorded into the data. During the manual target control period the sensors for reading out the target position were not working and the target table was

not automated. The target positions were written down in the run information and the table was manually adjusted between runs instead of during runs. I think the opportunity for human error here is high and I prefer not to include these spills, although other people think that these spills can be reliable if cross checked with the information from the radiation monitors. There is a period during roadset 62 where the magnet polarity is flipped compared to the rest of the roadset. This did not lead to good data because each roadset is designed for a specific magnet polarity. There was also an issue with approximately the middle third of roadset 67 where the data was reconstructed inaccurately. A fix for this was implemented but it was decided not to retrack the data since a new improved version of the reconstruction code was going to be run soon on all of the data. Once the R006 data is ready for analysis and quality checked this spill range should no longer be cut.

roadset	All	Complete	Liquid or Empty Flask	Valid
57	48270	45716	32044	29207
59	10239	8565	5914	5343
62	54736	53269	39176	36078
67	117827	112291	81183	71539
70	6336	6230	4601	3911
All	237408	224442	162918	146078

Table 4.4: List of number of spills at different stages in the cutting process. All is number of spills in the Spill table outside the ranges in table 4.3. Complete is the number of spills that have entries in all tables, and both EOS and BOS entries in Scaler. Liquid or Empty Flask is the result of requiring that the spill be on LH2, LD2, or the empty flask. Valid is the number of spills left after applying all data quality cuts.

4.2.2 Event Level

Table 4.5 has a list of all the event level cuts. Quality cuts remove reconstructed dimuons that might not be real dimuons or might not be reconstructed accurately. Target cuts ensure that the dimuons came from the target. The Drell-Yan cut drastically increases the chances of a dimuon being from the Drell-Yan process, as opposed to combinatoric background or a J/Ψ or Ψ' event. The trigger cut ensures the event is a result of our dimuon trigger and not any of the pre-scaled special triggers. The results on the dimuon yields from applying these results are in table 4.6.

The first step in checking to see if a dimuon is legitimate is checking the two tracks that compose it. The numHits requirement requires 15 out of 18 of the drift chamber planes to contain a hit from the track, any track with less probably has some reconstruction issues. Tracks that pass through the top half of the hodoscopes in some stations and the bottom half in others receive a roadID of 0. We are trying to only include dimuons that could have fired the trigger and such tracks can not be part of any trigger. A z0 value

Table	Value	Good range	type
kTrack	numHits	> 14	quality
	roadID	$\neq 0$	quality
	z0	$(-400, 200)$	quality
	chisq/(numHits - 5)	< 5	quality
	roadID (mu+) * roadID (mu-)	< 0	quality
	chisq_dump - chisq_target	> 10	target
	pz1 (Where numHits != 18)	> 18	quality
kDimuon	pT	< 2	quality
	dx	$(-2, 2)$	quality
	dy	$(-2, 2)$	quality
	dz	$(-250, 200)$	quality
	dpz	$(30, 120)$	quality
	xB	$(0, 1)$	quality
	xT	$(0, 1)$	quality
	xF	$(-1, 1)$	quality
	trackSeparation	$(-250, 250)$	quality
	chisq_dimuon	< 15	quality
	px1	> 0	quality
	px2	< 0	quality
	dz	$(-250, -60)$	target
	mass	> 4.2	Drell-Yan
Event	MATRIX1	1	trigger
	runID, eventID	no duplicates	quality
kEvent	status	0	quality
	runID, eventID,	no duplicates	quality
QIE	RF+08 through RF-08	$< \text{Inh_thres}(\text{BeamDAQ})$	quality
	RF+16 through RF-16	> 0	quality
	triggerCount	≥ 0	quality
	rfOnset	1 to 588 inclusive	quality
	intensity_p	< 60000	quality
	runID, eventID	no duplicates	quality

Table 4.5: List of event level cuts.

outside the cut range is far outside the region where a track could have come from the target or dump. The $\text{chisq}/(\text{numHits} - 5)$ cut removes tracks of poor reconstruction quality. A track's roadID is positive if it passed through the top halves of the hodoscopes and negative if it passed through the bottom halves. By requiring that the product of the roadIDs of the two tracks is negative it ensures that one came from the top and one came from the bottom. A dimuon with two tracks from the top or two tracks from the bottom can not satisfy our trigger.

chisq_dump is smaller the better the fit is to a dump origin, and chisq_target is smaller the better the fit is to a target origin. These values are very important for our target dump separation. The cut on $\text{chisq_dump} - \text{chisq_target}$ removes dimuons where the origin is from the dump or the origin is ambiguous. It has been tested on GMC and works well, as shown in figure 4.1. The effects on data are shown in figure 4.2.

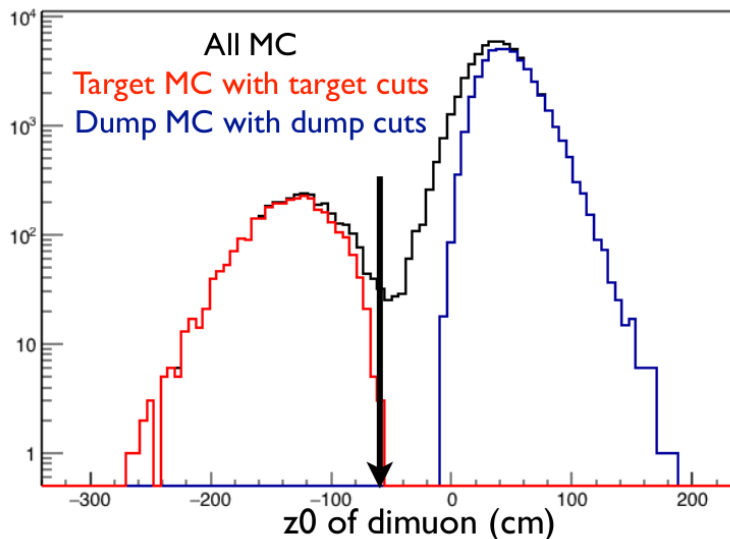


Figure 4.1: This graph shows reconstructed GMC dimuons originating from the target with the target cut applied and reconstructed GMC dimuons originating from the beam dump with the dump cut applied.

The cut on low z momentum tracks where the number of hits is not perfect is for removing a peak caused by background coincidences. The peak is from about 5 to 6 GeV and has a strong dependence on the intensity of the event as can be seen in figure 4.3 which suggests it is from combinations of unrelated hits and/or tracks. It was discovered that many of these dimuons had a track with very low momentum, when investigated it was shown that these low momentum tracks were strongly correlated with a low number of hits in the track, figure 4.4. It was hypothesized that these were probably not true tracks at all, but part of a track from stations two through four combining with background hits in station one. The cut of z momentum > 18 where $\text{numHits} < 18$ was implemented, and figure 4.5 shows an estimate of how much the background was reduced. When tested on reconstructed Monte Carlo, this cut removed less than 1% of high

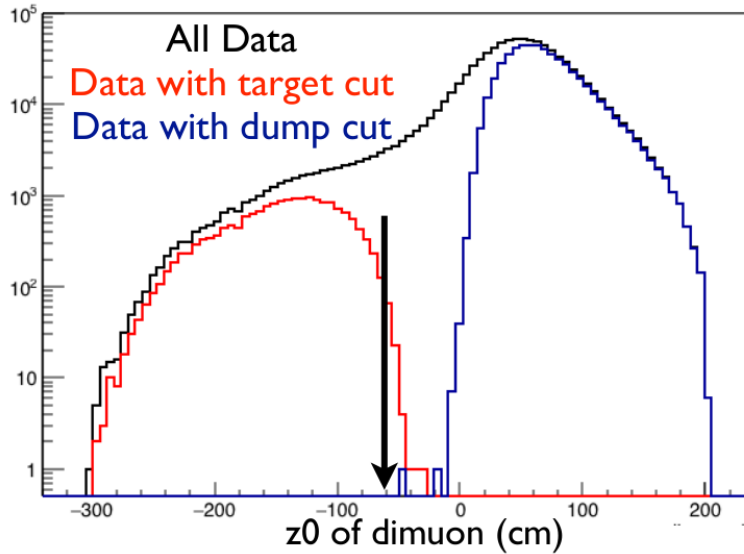


Figure 4.2: This graph shows dimuons reconstructed from data separated by the target and dump cuts.

mass dimuons.

The cut that removes events with p_T greater than 2 GeV is for cutting out a kinematic range that is mostly background. If one examines figures 4.6 and 4.7, one can see that the p_T distribution above 2 GeV is very different in data and Monte Carlo. If two uncorrelated single muons are reconstructed into a dimuon, though, if both their p_T are somewhat close to being in the same direction the reconstructed p_T can be high. This hypothesis is lent weight by the fact that the average intensity for events with $p_T > 2$ GeV is 35001 ± 357 but the average intensity for events with $p_T < 2$ GeV is 24737 ± 71 .

The dx, dy, and dz values in the kDimuon table are the coordinates for the origin of the dimuon. dx or dy values too far from the beam are probably not legitimate. The dz cut removes dimuons that are not a reasonable reconstruction to the dump or target. x_B , x_T , and x_F cuts remove dimuons with physically impossible attributes. The track separation is the difference in the z coordinate origin for both tracks. If the difference is too high then the tracks are not likely to be from the same source. The chisq_dimuon cut is a cut on how well the dimuon vertex reconstruction is a fit to the two original tracks. The px1 and px2 values are the x momentum of the positive and negative tracks after the vertex reconstruction step. Tracks with a charge and momentum combination that would've caused the magnet to bend their trajectory outside of the acceptance are not considered valid. The second, more strict dz cut is a target cut that is only used when one desires to exclude dump dimuons and ambiguous dimuons. The mass cut is for excluding dimuons from the J/Ψ and Ψ' region. There is also a lot of combinatoric background in the low mass region.

The Matrix1 cut on the Event table requires the FPGA1 trigger to have fired. It is required that the

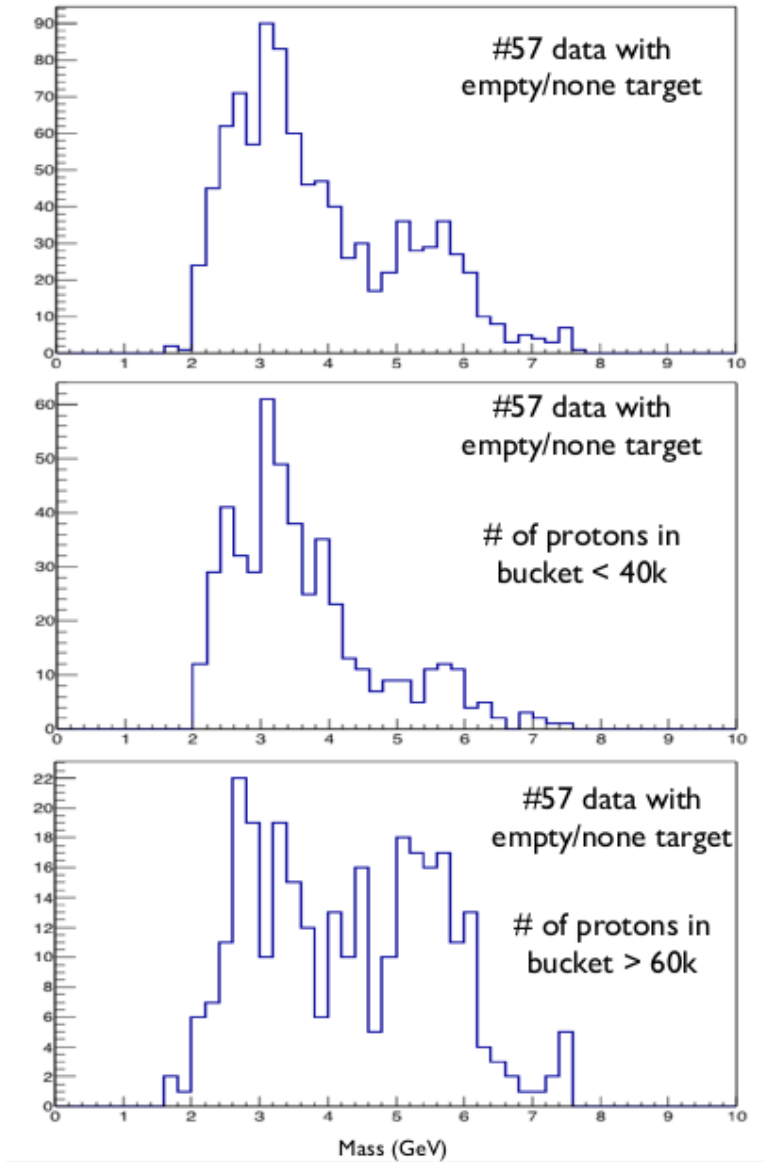


Figure 4.3: Graphs of the mass spectrum with different intensity cuts. The 5 to 6 GeV peak is much stronger at high intensity.

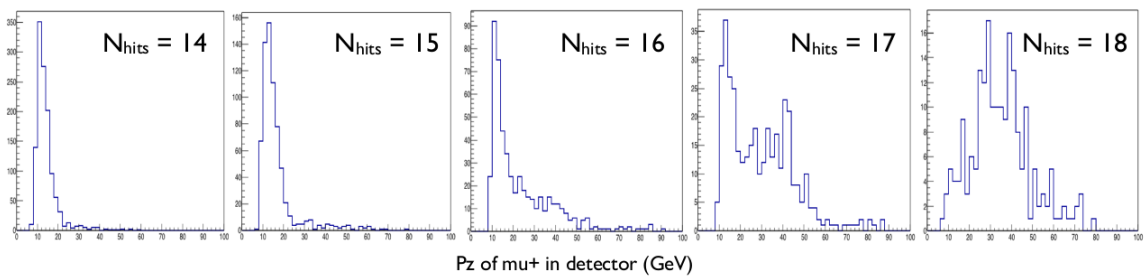


Figure 4.4: Graphs of the track z momentum spectrum for different numbers of hits per track. That low momentum tracks are much rarer at high quality suggests that many of the low momentum low quality tracks are not true tracks.

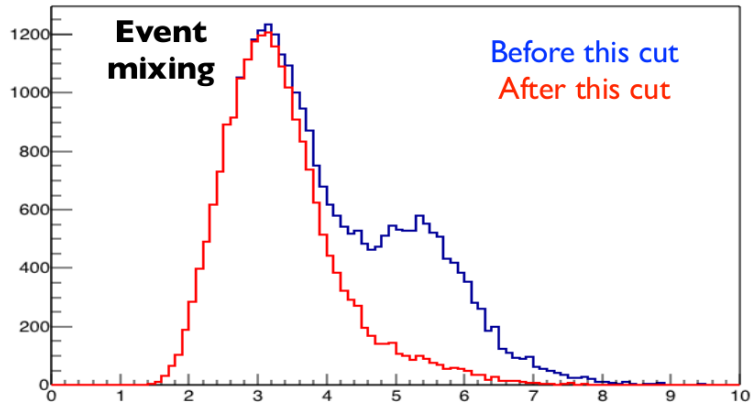


Figure 4.5: Graph of the mass spectrum of the combinatoric background estimate. This estimate is created by combining two muon tracks from separate events where no dimuon was found and doing vertex reconstruction on them. The suggested cut strongly reduces the background near 5 to 6 GeV.

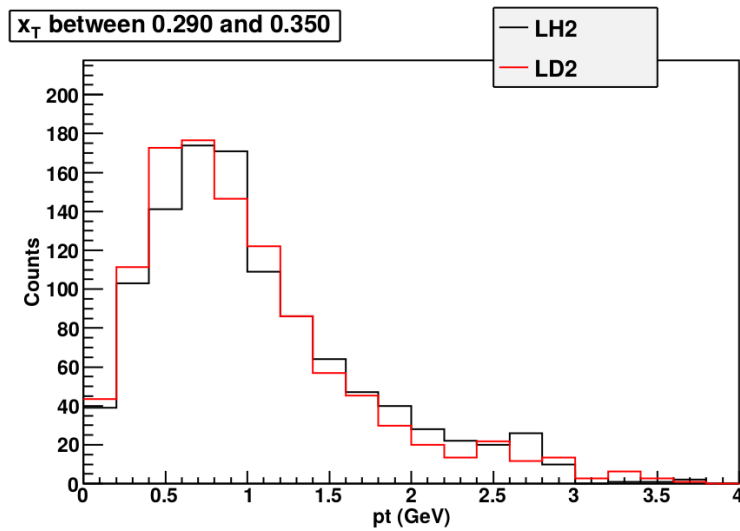


Figure 4.6: This graph shows the p_T distribution in data for one of the high x_T bins. Unlike the lower x_T bins, the p_T distribution is mostly flat instead of rapidly falling.

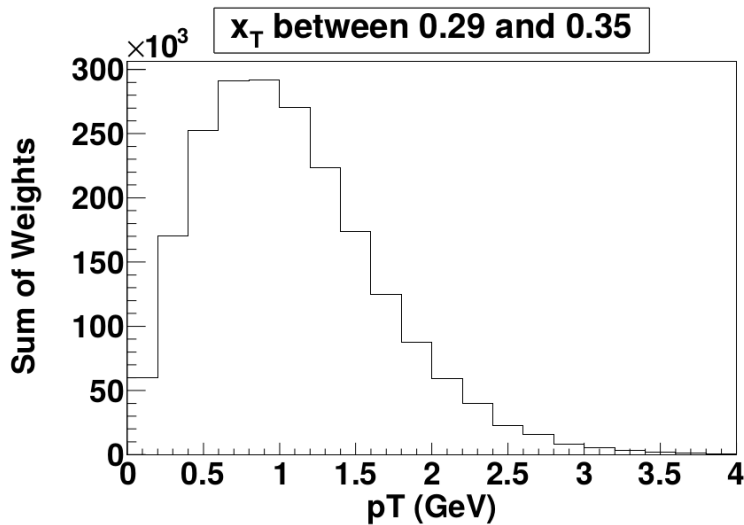


Figure 4.7: This graph is the same x_T range as 4.6, but with the distribution from the Monte Carlo instead of data. The yield falls rapidly with p_T above a p_T of 2 GeV compared to the data distribution.

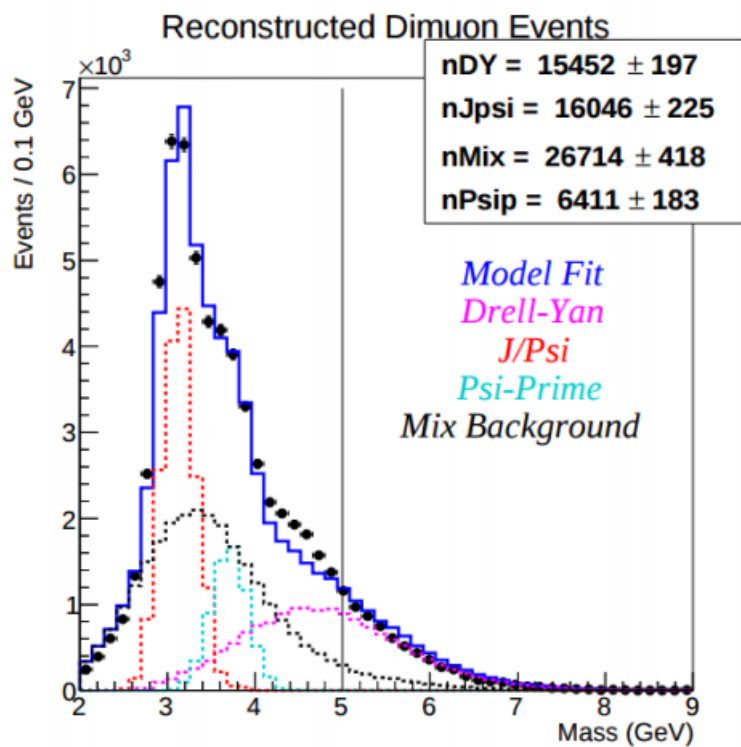


Figure 4.8: A mass fit of J/Ψ , Ψ' , Drell-Yan, and background spectrums. The dark blue curve is the total of the fits. The fits don't quite match the data between 4.2 and 5 GeV. Cutting at 5 GeV like the initial suggestion cuts too much data, I use a 4.2 GeV cut. The Drell-Yan curve comes from GMC which depends partially on the anti quark distributions which we are measuring, so some slight discrepancy between that and data does not bother me.

runID, eventID combination be unique in order to remove events that had DAQ issues.

The status = 0 cut on the kEvent table requires that the reconstruction code did not output an error code for that event. Again, the runID, eventID combination must be unique.

The QIE table has several cuts, as accurate intensity information is required to properly apply a rate dependence correction. There are 33 RF entries, RF-16 through RF+16, that record the intensity of the triggering bucket RF+00 and the 16 buckets before and after the triggering bucket. Any events where any of RF-08 through RF+08 are greater than the beam inhibit threshold are cut because the trigger should not have been able to fire. Any events where any RF value = 0 are cut because they are associated with bad QIE output; a value of zero is far enough below the QIE pedestal that it probably wasn't caused by QIE fluctuations during a time of no beam. triggerCount is a counter for the number of triggers fired during that spill, if it is > 0 then there is a DAQ problem, and such events have also been correlated with odd QIE output. rfOnset records the position of the trigger bucket in the turn, only values between 1 and 588 are sensible as there are exactly 588 buckets in a turn. Erroneous rfOnset values have also been correlated with bad QIE output. intensity_p is a measure of intensity for an event, it is the chamber intensity described in an upcoming section. If it is too high then the rate dependence fits for that region are unreliable and the weights for dimuons in that area are very high and actually increase the uncertainties on the results. Such events also have a high chance of being combinatorial background. The QIE table is also required to have a unique runID, eventID combination.

Roadset	Uncut	Valid	Target	Drell-Yan	T and DY	T, DY, and intensity
57	6257447	944088	11435	374225	6386	5975
59	1070454	138992	1643	54778	915	876
62	7894543	1445122	15906	605147	9295	9030
67	21106511	3629673	39729	1406008	22336	21871
70	992242	178527	2009	74152	1181	1154

Table 4.6: Uncut is all reconstructed dimuons from valid spills and relevant targets. Valid is the number of those dimuons in the x_T range that pass all of the quality cuts. Target also requires that the dimuon origin is from the target. Drell-Yan also includes the mass cut to cut out the Ψ peaks, but does not include the target cut. T and DY includes both the target and mass cut. The last field includes all of these cuts and the intensity cut as well. The intensity cut removes fewer dimuons in later roadsets as the beam quality has improved.

4.3 Rate Dependence Corrections

There are three rate dependence corrections in this analysis so far, the kTracker efficiency correction, the empty target correction, and the remaining rate correction. The kTracker efficiency correction is a target

and kinematic dependent correction for the inefficiency of the kTracker reconstruction program at high rates. This correction does not correct for any inefficiency that is not rate dependent. The empty flask correction is a target dependent correction that subtracts events from the empty flask from the total of liquid target events in order to account for anything that is not from the target that reconstructs to a target dimuon. This correction does correct for any such effects that aren't rate dependent. The remaining rate correction is a correction for all leftover rate dependence effects, currently the source of these are not known. It is likely that the combinatorial background is a large contributor to this. All of these corrections use fits that are a function of chamber intensity. Chamber intensity is an estimate of the intensity seen by our wire chambers. Almost any correction in this analysis has the potential to be rate dependent and a rate dependence analysis should be done on any new corrections in the future, such as a combinatorial background correction, unless it is very obviously not rate dependent like the target contamination. The empty flask correction was not expected to be rate dependent, but analysis shows that it unquestionably is.

The rate dependence corrections have to be three separate corrections instead of fitting the rate dependence and making a single correction. The empty flask correction is separate because only a portion of the correction is rate dependent, the portion that is not rate dependent would not be corrected for in a general rate dependence fit. In order to do the empty flask correction correctly the kTracker efficiency correction has to be calculated and extrapolated to the empty flask, so that is a separate correction as well.

4.3.1 QIE Pedestal

The response of the Cherenkov counter and the QIE to the presence of beam is linear with the intensity, but the y-intercept of this slope is not zero. This non-zero value when there is no beam is called the QIE pedestal and it is important to correct the QIE readout for it. Some of the rate dependence analyses graph dimuons per proton on the y-axis and intensity on the x-axis. Dimuons per proton has a measure of intensity in the denominator, and in the low intensity region neglecting the pedestal or getting it wrong can have a significant effect on this measurement even for a small pedestal. This can be seen in Figures 4.9, 4.10, and 4.11.

To calculate the pedestal is fairly straightforward. Almost all of the spill quality cuts fail when there is no beam, so these cuts are not used when calculating the pedestal. Since we are not looking for dimuons almost all of the event level cuts are also not used. Instead, only NIM3 events (random trigger) from spills where $G2SEM = 0$ are used. $RF+### > 0$ is still required, since $RF+###$ values equal to zero are associated with high values in nearby RF fields when there is no beam. Since the mean of the no beam $RF+###$ values is several standard deviations away from zero I think this cut does not bias the pedestal measurement. The

RF+00 values in these events are simply averaged together to find the pedestal. The pedestal does not seem to drift over time, but there is a jump in the pedestal in the middle of roadset 62 somewhere between spillIDs 448017 and 448470. All the spills between these two spillIDs have beam so it is not possible to locate when the split happens more precisely. The pedestal value before the jump is equal to 36.30 with a standard deviation of 6.48 and an uncertainty of 0.02. After the jump the pedestal is equal to 32.73 with a standard deviation of 6.69 and an uncertainty of 0.02. A plot of RF+00 values when the beam is off is in figure 4.12. A plot of the pedestal over time in roadset 62 where the jump occurs can be seen in figure 4.13.

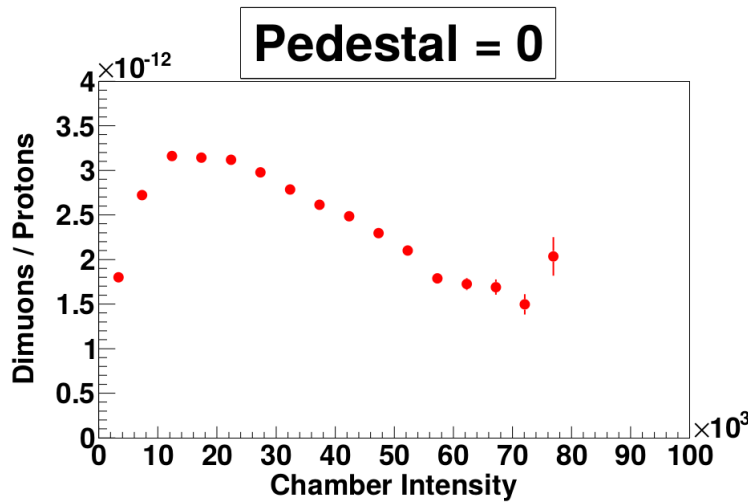


Figure 4.9: There is a very large hump in rate dependence at lower intensity when the pedestal is neglected. This is a graph for dump dimuons, since the statistics are better and shows the shape more clearly. The rate dependence is different for target dimuons but the idea here is to show the pedestal dependence.

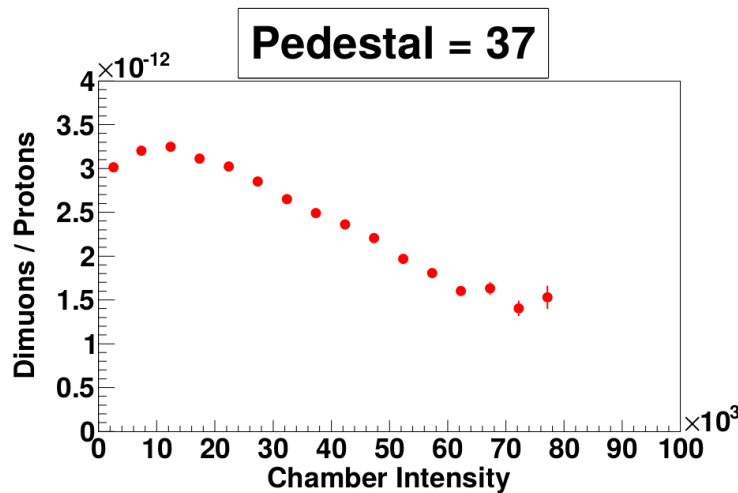


Figure 4.10: A rate dependence plot with the pedestal set to 37, fairly close to the correct value. When put next to a plot with a pedestal of zero the small hump suggests the pedestal is still a little too low, but since there are many contributions to the rate dependence we can't make such an assumption.

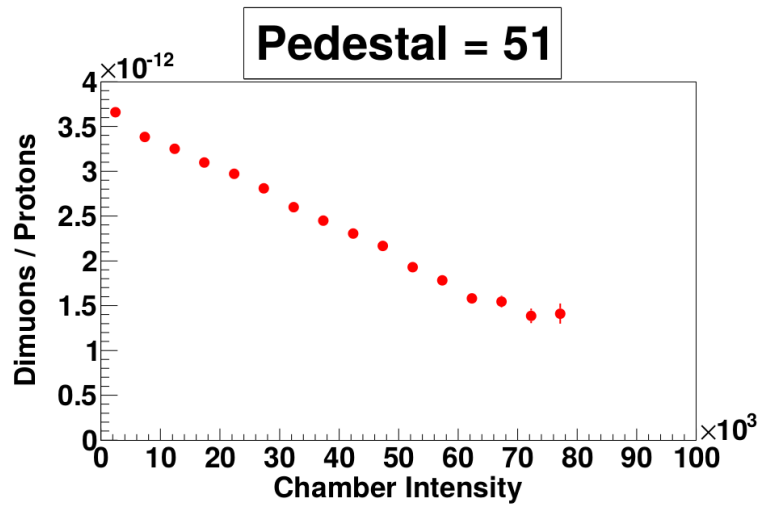


Figure 4.11: The pedestal set to 51, a value that is too high.

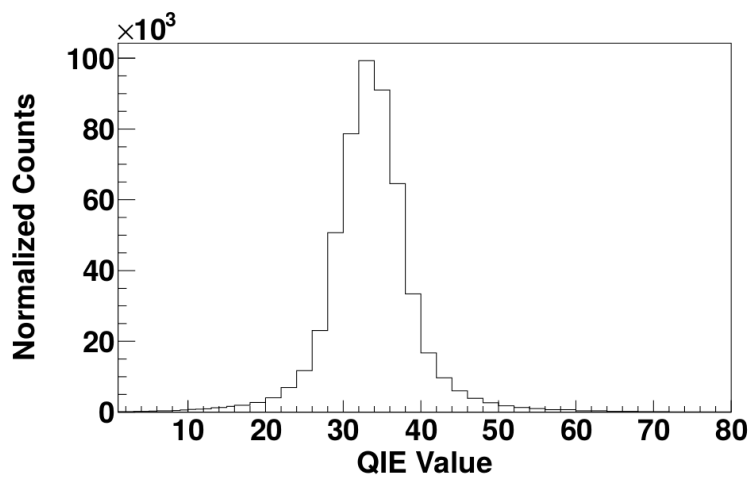


Figure 4.12: The distribution of RF+00 values when there is no beam.

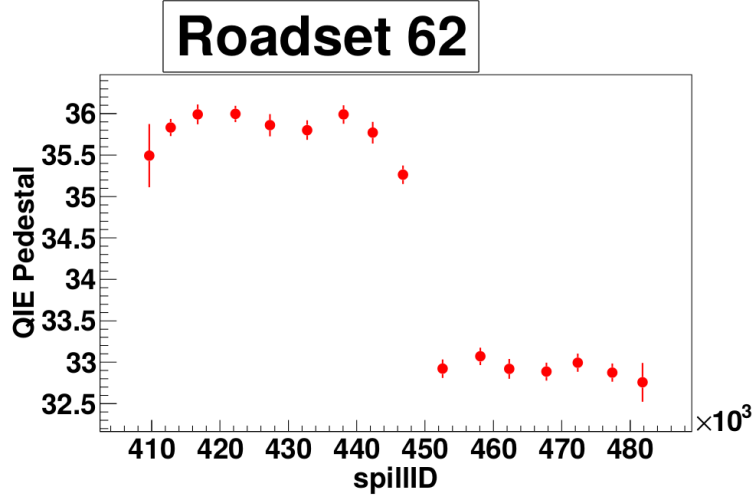


Figure 4.13: The pedestal jumps suddenly in the middle of roadset 62, but otherwise doesn't drift.

4.3.2 Chamber Intensity

The chamber intensity is an estimate of the intensity as seen by the drift chambers. The in time windows of the chambers cover several buckets. A hit in the chambers several buckets before or after the triggering bucket could possibly be in the in time window, but also possibly not, depending on the distance to the closest wire. The triggering bucket has a weight of 1 because hits from this bucket are always in the in time window. If, hypothetically, the tracks from the next bucket have a 90% chance of being in the in time window, then the weight for that bucket would be 0.9. To calculate the chamber intensity, first the weights are used to get a weighted average of the RF+### fields in the QIE table and the pedestal is subtracted from this average. Then this value is converted from QIE units to protons by multiplying by G2SEM/QIEsum. G2SEM is the best measure of the number of protons in a spill and QIEsum is the sum of the QIE readout for every bucket in that spill. The formula for the chamber intensity is given in equation 4.41.

$$chamber_intensity = \left(\frac{\sum_i w_i * RF_i}{\sum_i w_i} - pedestal \right) * \frac{G2SEM}{QIEsum} \quad (4.41)$$

In order to calculate the weights for the chamber intensity, the RT curves are used. All drift times for hits have been calculated with the assumption that they came from the triggering bucket. For buckets that come after RF+00, the reconstructed drift time will be greater than the real drift time, and the reconstructed drift time has to be less than or equal to the maximum drift time of an in time hit. The shift between reconstructed and real drift time is equal to the time between buckets (18.83 ns) multiplied by the difference in bucket number. I calculate the cutoff time, which is the maximum real drift time that could be reconstructed to less than or equal to the maximum drift time. This cutoff time can be turned into a cutoff distance by using the

RT table. Everything that hits closer than this distance is within the in time window, while everything that hits farther away is not. So to get the acceptance of tracks in this bucket, divide the cutoff distance by the max drift distance in the chamber. For buckets before RF+00, the math is similar, with a few differences. The reconstructed drift time has no chance of being greater than the max drift time, but it does have a chance of being less than zero, which would be outside the in time window. After calculating the cutoff distance, all hits greater than this distance are accepted, not less than this distance. This acceptance has to be calculated separately for each chamber, as they have different RT curves and in time windows. The weights for the different chambers are averaged together to get the overall weights for the chamber intensity calculation. Equation 4.42 is used for calculating the weights for a single chamber for buckets following the triggering bucket, where $R(t)$ is a function that gives the drift distance given a drift time and i is from RF \pm i . Equation 4.43 is used for buckets preceding the triggering bucket. In the analysis $R(t)$ is not truly a function, it is interpolated from entries in an RT table. The calculated weights can be found in table 4.7.

$$w_i = \frac{R(MaxDriftTime-18.83*i)}{MaxDriftDistance} \quad (4.42)$$

$$w_i = \frac{MaxDriftDistance-R(-18.83*i)}{MaxDriftDistance} \quad (4.43)$$

There is another intensity, the trigger intensity, which uses RF+00 instead of a weighted average of RF fields. It is called the trigger intensity because it measures the intensity of the triggering bucket only. Although all the rate dependencies found so far have a much stronger dependence on the chamber intensity, it is possible that there is a source of rate dependence that has a stronger dependence on the trigger intensity. The equation for trigger intensity is in equation 4.44.

$$trigger_intensity = (RF+00 - pedestal) * \frac{G2SEM}{QIEsum} \quad (4.44)$$

4.3.3 kTracker Efficiency

The kTracker efficiency is the efficiency of the tracking software, kTracker, at reconstructing dimuons. As intensity increases there are more background hits in the chambers and the efficiency drops. This increase in hits and the resulting drop in efficiency has a small but significant target dependence. This is because pions from the target instead of the dump have a better chance of decaying into a muon before being destroyed in a nuclear interaction because they are travelling through air instead of iron. As some areas of the detectors have more background hits than others a strong kinematic dependence can be seen by graphing the kTracker

bucket	weight
-13	0.000814249448012561
-12	0.00286624394357204
-11	0.00597014464437962
-10	0.0121262921020389
-9	0.0300863217562437
-8	0.0777262449264526
-7	0.159446656703949
-6	0.259932696819305
-5	0.36718875169754
-4	0.48815906047821
-3	0.678969323635101
-2	0.847788095474243
-1	0.956475257873535
0	1
1	0.989173948764801
2	0.897678017616272
3	0.76782888174057
4	0.647167325019836
5	0.533894777297974
6	0.448848754167557
7	0.356435418128967
8	0.26369309425354
9	0.177964717149734
10	0.108504571020603
11	0.0540100000798702
12	0.0192185696214437
13	0.00308302068151534

Table 4.7: The weights associated with each RF bucket.

efficiency of different kinematic regions.

The kTracker efficiency can be calculated by using two sets of data. The first set, the clean set, is simply GMC Drell-Yan simulated data. The second set, the messy set, is the same GMC events with the hits from NIM3 events from data added to the Hit table. Both sets are then reconstructed using kTracker. To calculate the kTracker efficiency one divides the total GMC weight of good kDimuons in the messy sample by the total GMC weight of good kDimuons in the clean sample. I require all spill and event level cuts on this data, with two exceptions. I don't require the intensity < 60000 cut, as these fits help me decide where to place the intensity cut. I don't require the MATRIX1 = 1 cut since the embedded events are NIM3 events, not MATRIX1 events. An additional cut I require is the messy events to have been reconstructed in the clean sample as well to the same bin in x_T . If this data is binned by intensity (of the NIM3 event), the rate dependence of the kTracker efficiency can be seen.

In order to get an accurate fit I took into account the fact that the uncertainties are significantly asymmetric when p is close to zero or one. I used the Wilson score interval to calculate the asymmetric uncertainties, with the equations modified to reflect the fact that the events are weighted. I did not believe ignoring the Monte Carlo weights on the events was legitimate due to the strong kinematic dependence from several kinematic variables. It would be ideal to fit to multiple kinematic bins at once but this is difficult due to the amount of statistics required to get a good fit. There could be some systematic error due to the kinematic distribution of Monte Carlo being different than data, but I believe this effect would be small.

The original Wilson score interval[49] is equation 4.45 where $x = \lambda^2/n$ and $\hat{p} = \sum success/n$. The interval is for a confidence of P_λ where P_λ is the area between $+\lambda\sigma$ and $-\lambda\sigma$ in a bell curve. As the fitter (ROOT) expected one σ error bars I used $\lambda = 1$. The Wilson score interval also uses the Gaussian approximation of the distribution of observed values of p around the real value of p so it should also be avoided at small n .

$$p = \frac{\hat{p}+0.5x}{1+x} \pm \frac{\sqrt{\hat{p}(1-\hat{p})x+0.25x^2}}{1+x} \quad (4.45)$$

To modify the equations for a set of weighted data, I made the substitutions in equations 4.46 and 4.56. The mean and variance of the total weight of all the successes can be derived from knowing the mean and variance for a single event, which are $p_i W_i$ and $p_i(1-p_i)W_i^2$ respectively. The mean of the total weight of successes is then $\sum_i^n p_i W_i$ for multiple events, and one divides by the sum of the weights to go from the total weight of successes to \hat{p} .

$$\hat{p} = \frac{\sum_i^n p_i W_i}{\sum_i^n W_i} \quad (4.46)$$

To get 4.56 we need the variance so we can find a substitution that is analogous to the part of the original derivation in equations 4.47, 4.48, and 4.49.

$$(p - \hat{p})^2 = \lambda^2 \sigma_{\hat{p}}^2 \quad (4.47)$$

$$(p - \hat{p})^2 = \lambda^2 p(1 - p)/n \quad (4.48)$$

$$(p - \hat{p})^2 = xp(1 - p) \quad (4.49)$$

Find the variance of the total weight of success.

$$\sigma^2 = \sum_i^n p_i(1 - p_i)W_i^2 \quad (4.50)$$

Get the variance of \hat{p} .

$$\sigma_{\hat{p}}^2 = \frac{\sum_i^n p_i(1 - p_i)W_i^2}{(\sum_i^n W_i)^2} \quad (4.51)$$

Assign ϵ_i as the difference between mean p and p_i .

$$\sigma_{\hat{p}}^2 = \frac{\sum_i^n (p + \epsilon_i)(1 - p - \epsilon_i)W_i^2}{(\sum_i^n W_i)^2} \quad (4.52)$$

$$\sigma_{\hat{p}}^2 = p(1 - p) \frac{\sum_i^n W_i^2}{(\sum_i^n W_i)^2} + \frac{\sum_i^n \epsilon_i W_i^2}{(\sum_i^n W_i)^2} - \frac{\sum_i^n 2p\epsilon_i W_i^2}{(\sum_i^n W_i)^2} - \frac{\sum_i^n \epsilon_i^2 W_i^2}{(\sum_i^n W_i)^2} \quad (4.53)$$

Assume all the ϵ_i are insignificantly small.

$$\sigma_{\hat{p}}^2 \approx p(1 - p) \frac{\sum_i^n W_i^2}{(\sum_i^n W_i)^2} \quad (4.54)$$

$$\frac{1}{n} = \frac{\sum_i^n W_i^2}{(\sum_i^n W_i)^2} \quad (4.55)$$

$$x = \lambda^2 \frac{\sum_i^n W_i^2}{(\sum_i^n W_i)^2} \quad (4.56)$$

The variance in this method is an approximation and so there will be some slight mistake in the length

of the error bars. However, the mean point is still placed correctly so I believe that overall this leads to good fits.

I combine all the roadsets into one clean sample and one messy sample. Then I fit the efficiency of each x_T bin and each target as a function of chamber intensity, with a bin width of 5,000 and bins from 0 to 100,000 intensity. After trying several fit forms I found that exponential decay works the best. An example of this fit can be found in figure 4.14.

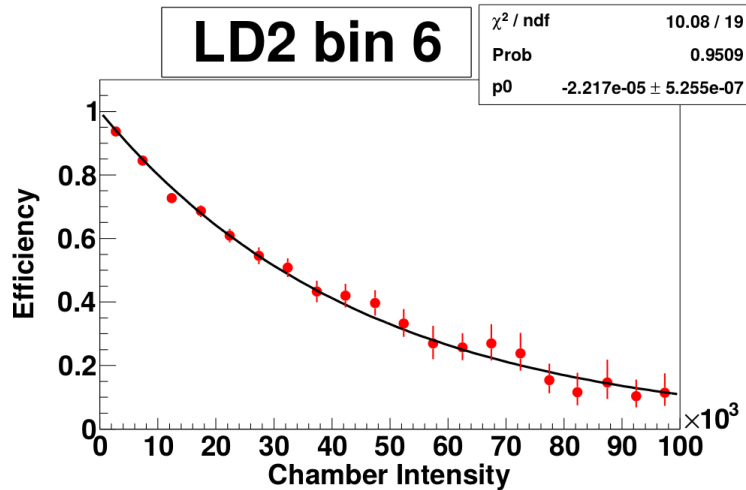


Figure 4.14: Example of a fit of kTrackerEfficiency data to exponential decay.

The exponents for the fits for each x_T bin show a clear x_T dependence. Plotting these exponents as a function of x_T shows a linear relation between the fit exponent and x_T . I fit a linear function to these exponents to get the efficiency as a function of x_T and intensity. The formula for the efficiency is in equation 4.57. Each individual dimuon is assigned an efficiency and is given a weight equal to $1/\text{efficiency}$. The fitting program also return a correlation matrix for the fit, which is necessary for proper uncertainty calculation, especially in cases like these with strong off diagonal elements. The fit quantities can be found in table 4.3.3. The fit for deuterium can be found in figure 4.15.

$$Efficiency = e^{-(p_0 + p_1 * x_T) * intensity} \quad (4.57)$$

The fit values for the empty flask in table 4.3.3 were extrapolated from the LH2 and LD2 values based on the nuclear interaction lengths of the targets because there are currently no empty flask GMC productions with empty flask embedded random triggers. One can assume that the difference between the targets is a function of how much of the beam interacts with the target. Using $P_{0,Target}$ as the kTracker efficiency p_0 from table 4.3.3 for target T we can linearly extrapolate to come up with a formula for P_E where no beam

target	p_0	p_0 uncertainty	p_1	p_1 uncertainty	$\text{corr}(p_0, p_1)$
LH2	8.030e-6	5.170e-7	3.589e-5	1.914e-6	-0.929
LD2	8.835e-6	5.926e-7	4.206e-5	2.206e-6	-0.926
Empty	6.758e-6	1.628e-6	2.617e-5	6.039e-6	-0.927

Table 4.8: The fit parameters for the LD2 and LH2 targets and the empty flask. The empty flask fit parameters were extrapolated from the LH2 and LD2 parameters.

interacts with the target. p_1 is calculated in the same manner.

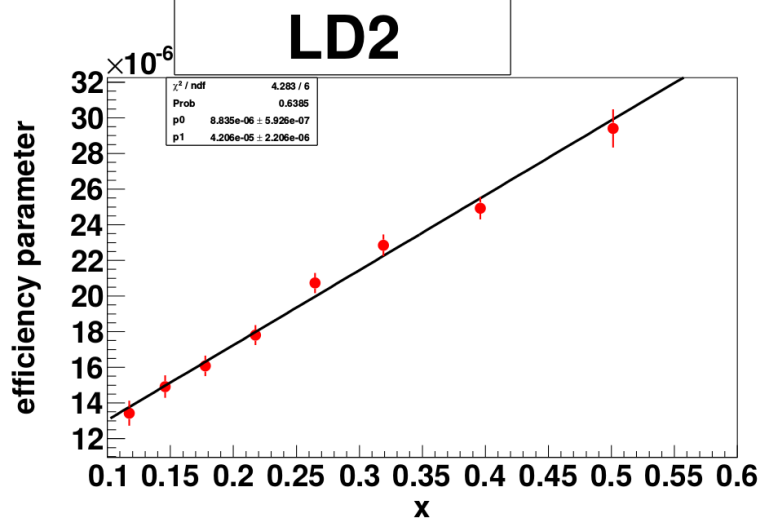


Figure 4.15: Fitting the strength of the rate dependence as a function of x_T .

$$P_{0_Empty} = P_{0_LH2} - IFrac_{LH2} * \frac{\Delta P_0}{\Delta IFrac} \quad (4.58)$$

$$P_{0_Empty} = P_{0_LH2} - IFrac_{LH2} * \frac{P_{0_LD2} - P_{0_LH2}}{IFrac_{LD2} - IFrac_{LH2}} \quad (4.59)$$

To find the affect of the uncertainty of the hydrogen fit on the cross section ratio, I calculate the cross section ratio several times, once with the exponent at its normal value, and once each with p_0 changed by $\pm 1\sigma$. The difference between the base cross section ratio and the $+\sigma$ cross section ratio is $K_{LH2_P0_Plus}$. I calculate $K_{LH2_P1_Plus}$ in the same manner. The equation for calculating the overall upper uncertainty for the hydrogen fits is equation 4.60. The lower uncertainties and the deuterium uncertainties are calculated in the same manner.

$$\sigma = \sqrt{K_{LH2_P0_Plus}^2 + K_{LH2_P1_Plus}^2 + Corr_{LH2}(p_0, p_1) * K_{LH2_P0_Plus} * K_{LH2_P1_Plus}} \quad (4.60)$$

It should be noted that both the messy and clean samples have 6% of the Monte Carlo hits removed (the same hits). This was done to simulate chamber inefficiency, although the chamber inefficiency is not well known. This could be related to the fact that some events that failed to reconstruct in the clean sample were successfully reconstructed in the messy sample. Additionally, the residuals between the reconstructed quantities and those of Monte Carlo truth were similar for events reconstructed in the clean sample and events only reconstructed in the messy sample. It has been hypothesized that a messy hit near a removed true hit can aid the reconstruction, therefore the chamber efficiency could have an effect on the strength of the kTracker efficiency. A study that is a good idea but which has not been done yet is to redo the kTracker efficiency studies at several different simulated chamber inefficiencies to study the correlation between chamber efficiency and kTracker efficiency.

I considered the possibility that the true rate dependence of the kTracker efficiency could be on trigger intensity instead of chamber intensity. If efficiency is graphed as a function of trigger intensity there is a strong correlation with it. Trigger intensity and chamber intensity are strongly correlated so a dependence on one can appear similar to a dependence on the other. To test how much of a dependence there was on each type of intensity I graphed the efficiency of LD2 as a function of chamber intensity while cutting all dimuons not between 20,000 and 30,000 trigger intensity. Then I graphed the efficiency as a function of trigger intensity while cutting all dimuons not between 20,000 and 30,000 chamber intensity. Figure 4.16 where I fixed trigger intensity and let chamber intensity vary still shows a strong dependence, while figure 4.17 where chamber intensity was fixed while trigger intensity was varied is flat. It is clear that the dependence of kTracker efficiency is on chamber dependence.

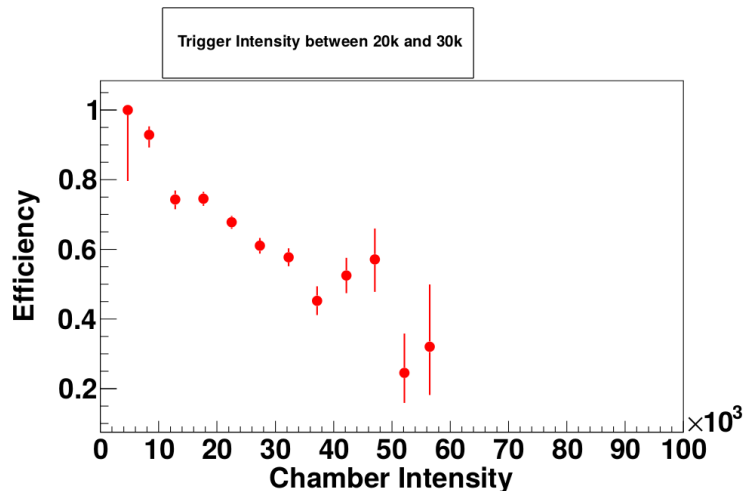


Figure 4.16: The dependence of the kTracker efficiency on chamber intensity, with dependence on trigger intensity removed.

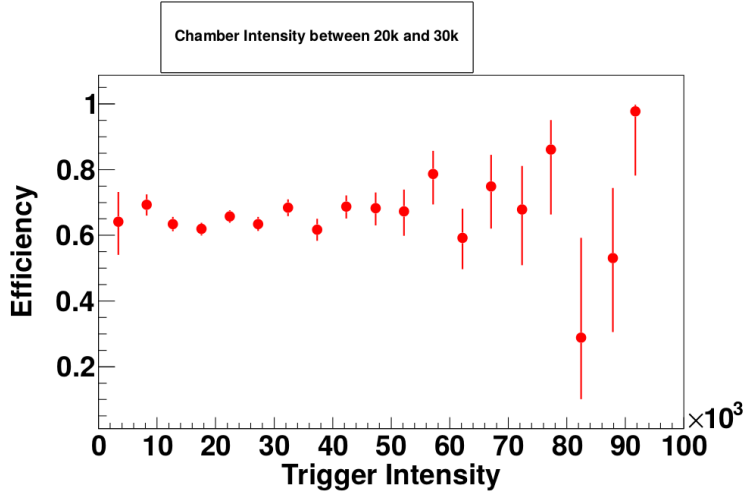


Figure 4.17: The dependence of the kTracker efficiency on trigger intensity, with dependence on chamber intensity removed.

4.3.4 Empty Flask Correction

The empty flask data has a strong rate dependence, with many more reconstructed dimuons per proton being found at higher intensities. When the \bar{d}/\bar{u} analysis was being developed, a single fit was made to the rate dependence for each target without breaking the rate dependence down into its components. Additionally, an empty flask correction was made that had no rate dependence in it. Because of the strong but unknown rate dependence of empty flask events, this led to the rate dependent part of the empty flask events being corrected for twice, once in the empty target correction and once in the rate dependence correction. The shift in the cross section ratio from this mistake was significant enough that the \bar{d}/\bar{u} extraction was inconsistent with E866. Now the empty flask correction is a rate dependent correction. The lesson to be learned here is that different corrections should not be assumed to be independent of each other. There was no reason to expect rate dependence in the empty target correction, but we found it there anyway.

The point of the empty flask correction is to remove the influence of several sources of false positives of dimuons originating from the target. If dimuons being generated from the dump or the upstream apparatus are being reconstructed to the target region then they will also show up in data taken on an empty flask. If a single muon from the dump and a single muon from upstream are being reconstructed together as a dimuon from the target region, that too will show up in data taken on an empty flask. Since there is no target the data will be lacking any true dimuons that originate from the target. Thus, the rate of empty flask dimuons can be subtracted from the rate of liquid target dimuons to get the rate of true liquid target dimuons.

To correct for the empty flask events I calculated the ratio of empty flask dimuons per empty flask

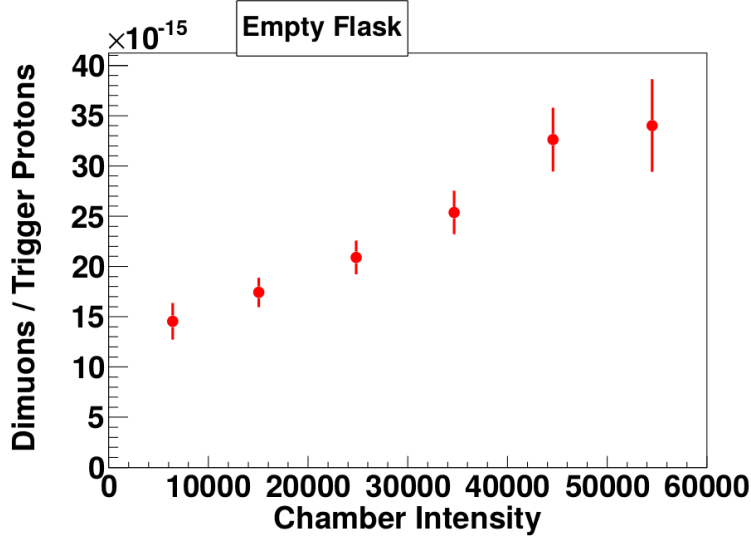


Figure 4.18: The rate dependence of empty flask events. It is strongly rate dependent but also does not go to zero at zero intensity.

proton to liquid target dimuons per liquid target proton, binned in chamber intensity. In this calculation the dimuons were given weights according to the kTracker efficiency fits. I then calculated the natural log of these ratios and graphed them vs. chamber intensity. I made a linear fit and the parameters for each liquid target can be found in table 4.9. The value of the fit at any intensity is the natural log of the chance that a liquid target dimuon is actually from a non-target source. Each dimuon is given a weight according to equation 4.61, where I is the intensity and K is the weight given to them from the kTracker efficiency fits. p_0 and p_1 are the y-intercept and linear coefficient for the linear fit, respectively. An example of one of these fits is in figure 4.19.

Target	p_0	p_0 uncertainty	p_1	p_1 uncertainty	$\text{corr}(p_0, p_1)$
LH2	-2.323	8.835e-2	1.014e-5	2.805e-6	-0.8933
LD2	-3.062	8.820e-2	1.251e-5	2.803e-6	-0.8933

Table 4.9: Table of parameters for empty flask corrections.

$$\text{Weight} = (1 - e^{p_0 + p_1 * I}) * K \quad (4.61)$$

To find the effect of the uncertainty of the empty flask fits on the cross section ratio, I calculate the cross section ratio several times, once with the fit parameters at their normal values, once each with p_0 for both targets changed by $\pm 1\sigma$, and once each with p_1 for both targets changed by $\pm 1\sigma$. Since most of the uncertainty in the parameters came from the low empty flask statistics I changed the parameters for both

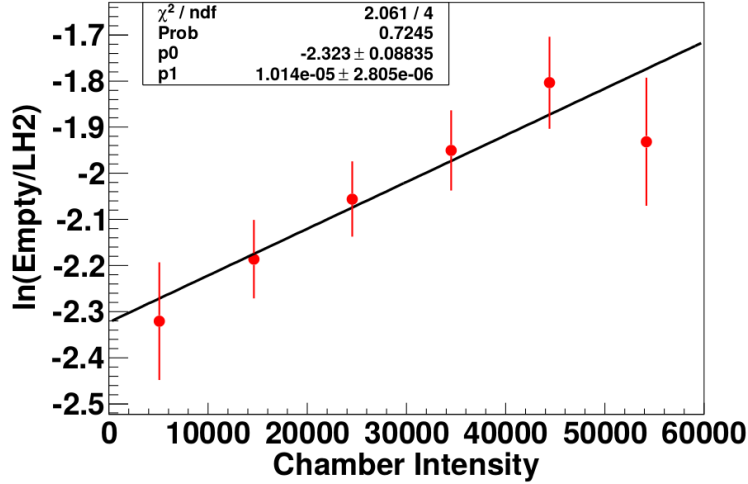


Figure 4.19: A fit of the natural log of the ratio of empty flask events to liquid target events, corrected for the number of protons on each target.

targets at the same time instead of calculating individual uncertainties for each liquid target. The difference between the base cross section ratio and the $+\sigma_{p_0}$ cross section ratio is E_{P0_Plus} . I calculate E_{P1_Plus} in the same manner. The equation for calculating the overall upper uncertainty is equation 4.62. The lower uncertainties are calculated in the same manner.

$$\sigma = \sqrt{E_{P0_Plus}^2 + E_{P1_Plus}^2 + Corr(p_0, p_1) * E_{P0_Plus} * E_{P1_Plus}} \quad (4.62)$$

It is possible that the empty target correction should be slightly reduced to account for the attenuation of the beam through the target that is not present with the empty flask in place. This would be needed if the contribution was mostly dimuons from the dump. However, without knowing how many of the empty flask constructed dimuons come from the dump, how many from upstream, and how many from a combination of two independent muons from upstream or dump, it is not possible to properly tune the empty target correction in such a way.

Like the kTracker efficiency correction, I considered the possibility of the fits having a stronger dependence on trigger intensity. This seemed very likely since most of the empty flask dimuons are probably made up of real tracks. Since hits from tracks from buckets outside the triggering bucket would not line up correctly when kTracker attempts to reconstruct them, tracks from outside the triggering bucket would be much less likely to contribute to empty flask false positives. Unlike with kTracker efficiency, making graphs for a small range of trigger intensity and graphing vs chamber intensity was not viable due to the much lower statistics. However, figure 4.20 is good evidence that there is almost no trigger intensity dependence in the empty flask

events.

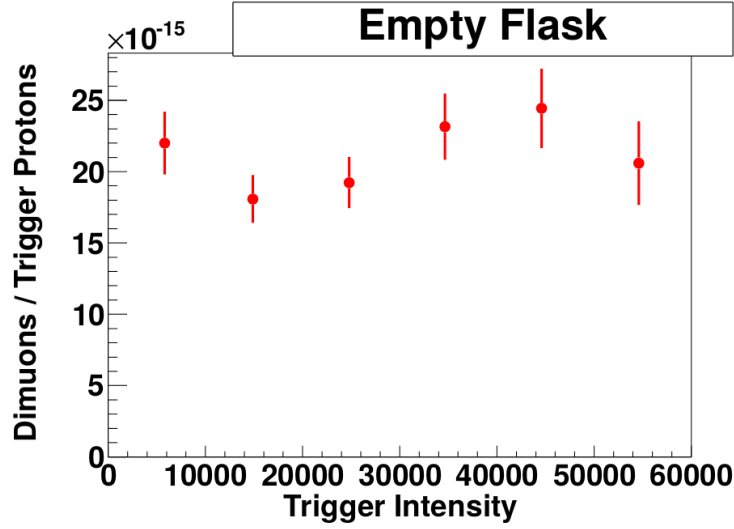


Figure 4.20: The rate dependence of empty flask events when plotted against trigger intensity instead of chamber intensity. It is relatively flat.

4.3.5 Remaining Rate Dependence

After applying both the kTracker efficiency and empty flask corrections there is still some rate dependence with a positive slope. The origin of this rate dependence is not yet known. The rate dependence for the deuterium target is shown in figure 4.21. Since I had trouble fitting both LH2 and LD2 targets to the same shape and in general the fits were bad, I decided to fit a graph of the natural log of the ratio of LD2 and LH2. I would assume that the rate dependence goes to zero at zero intensity and take the y-intercept of the fit as the true value. The idea is to weight the LD2 dimuons based on the fit so that the natural log of the ratio at any intensity value is equal to the natural log of the ratio at intensity equal to zero. I find it useful to break the fit $f(I) = \ln(\frac{LD2}{LH2}(I))$ down into an intercept p_0 and a rate dependent part $g(I)$.

$$\ln(\frac{LD2}{LH2}(0)) = \ln(\frac{LD2}{LH2}(I) * W(I)) \quad (4.63)$$

$$p_0 = \ln(\frac{LD2}{LH2}(I)) + \ln(W(I)) \quad (4.64)$$

$$p_0 = p_0 + g(I) + \ln(W(I)) \quad (4.65)$$

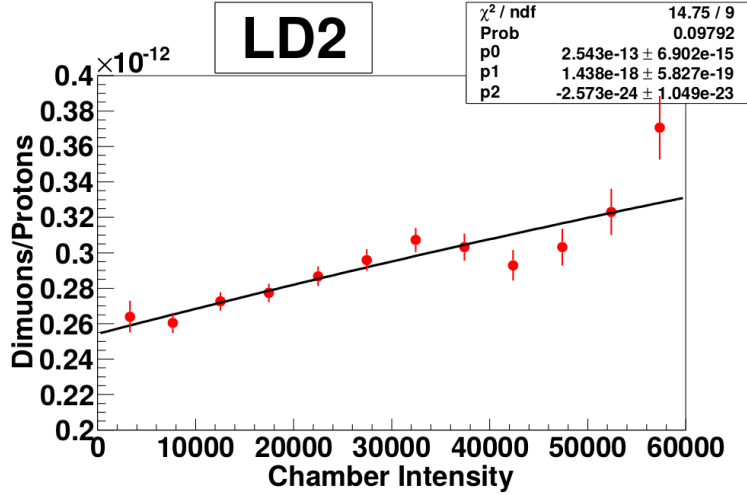


Figure 4.21: The remaining rate dependence after the kTracker efficiency and the empty flask corrections. It is still not very flat.

$$W(I) = e^{-g(I)} \quad (4.66)$$

The final weight of an LD2 dimuon is the weight from equation 4.66 multiplied by the weights from the kTracker efficiency and empty target corrections. LH2 dimuons just use the empty flask and kTracker efficiency weights.

This method of weighting the dimuons makes the results very dependent on what the y-intercept turns out to be. I tried a variety of fits and got reasonable results from multiple fits that had significantly different y-intercepts. Figures 4.22 through 4.24 show the fits that I tried. I prefer the fit that is a quadratic fit without a linear term because it has a balance between good χ^2 and a small number of parameters, so I used it as the main fit. However, since the shape of this fit wasn't a clear winner, I used the other two fits as well to generate systematic uncertainties related to this correction. Equation 4.67 gives the additional weight added to deuterium dimuons to correct for the remaining rate dependence.

$$W(I) = e^{-3.988\text{e-}11*I} \quad (4.67)$$

To find the effect of the remaining rate dependence fits on the cross section ratio, I calculate the cross section ratio several times, once with the p_1 fit parameter at its normal value, and once each with p_1 for changed by $\pm 1\sigma$. These give the upper and lower uncertainties from the fit parameter. I also calculate the cross section ratio using the linear and quadratic fits. The difference between the linear fit and the nominal fit is the upper uncertainty from the choice of fit shape and the difference between the quadratic fit and

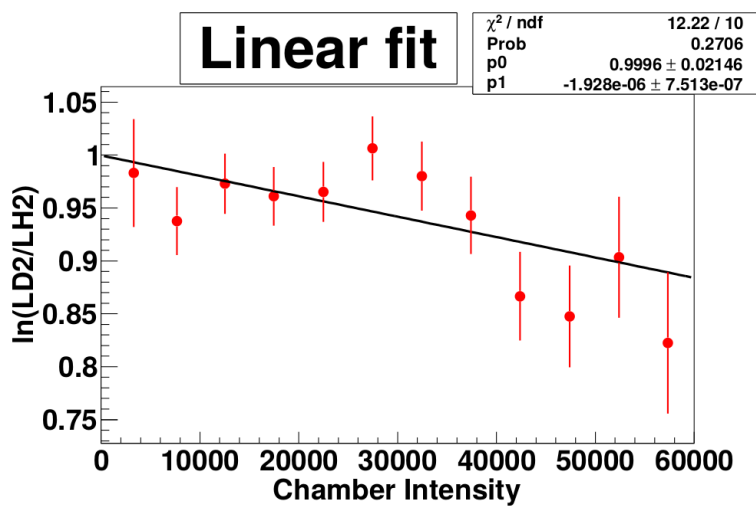


Figure 4.22: The natural log of the ratio of LD2 to LH2 as a function of chamber intensity. It is fit with a linear fit.

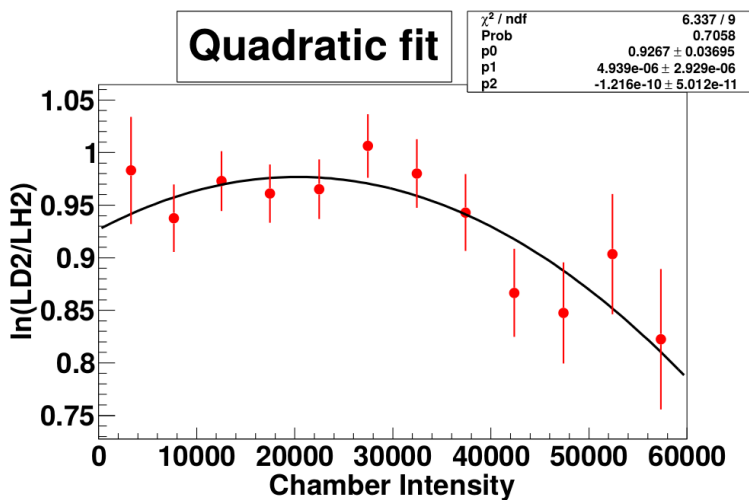


Figure 4.23: The natural log of the ratio of LD2 to LH2 as a function of chamber intensity. It is fit with a quadratic fit.

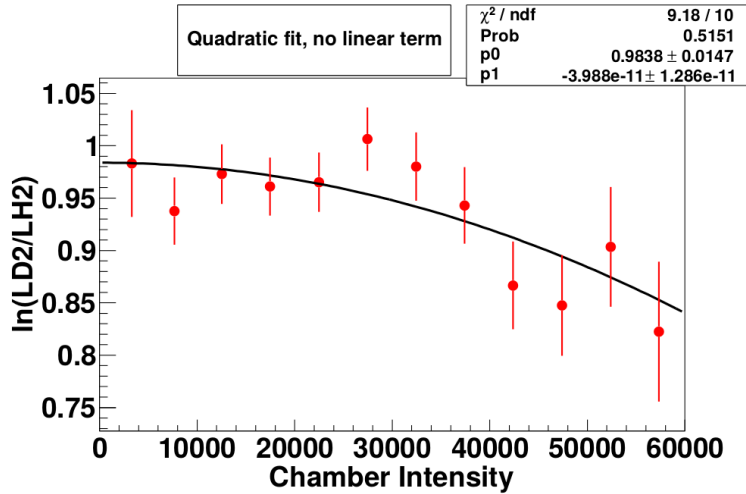


Figure 4.24: The natural log of the ratio of LD2 to LH2 as a function of chamber intensity. It is fit with a quadratic fit that is missing the linear term.

the nominal fit is the lower systematic uncertainty from the choice of fit shape. Both upper uncertainties are added in quadrature to get the upper uncertainty associated with the remaining rate dependence, and similarly for the lower uncertainty.

I also considered the possibility of a stronger dependence on trigger intensity than on chamber intensity. Looking at figure 4.25 it looks as though the dependence on trigger intensity is weaker. Because simply eye balling it or choosing the graph with the strongest slope isn't enough justification for such a decision, I made two graphs. The first, figure 4.26, shows the dependence on trigger intensity after the points have been weighted according to the fit from figure 4.24. The second, figure 4.27, shows the dependence on chamber intensity after the points have been weighted according to the fit from figure 4.25. Both of the graphs are relatively flat, so it is difficult to discern what the graphs truly depend on, so I went with the fit to chamber intensity since it has a stronger correlation. This will be worth looking at again when the experiment has more data and less statistical uncertainty.

I also checked for a dependence in these fits on x_T . To check this, I divided the data up into an $x_T < 0.2$ half and a $x_T > 0.2$ half. I made graphs for each after weighting the points based on the fit from figure 4.24. As can be seen in figures 4.28 and 4.29 both of these graphs seem reasonably flat after the correction, so there is probably no x_T dependence in this rate dependence correction. Again, this will be worth looking at again when the experiment has more data and less statistical uncertainty.

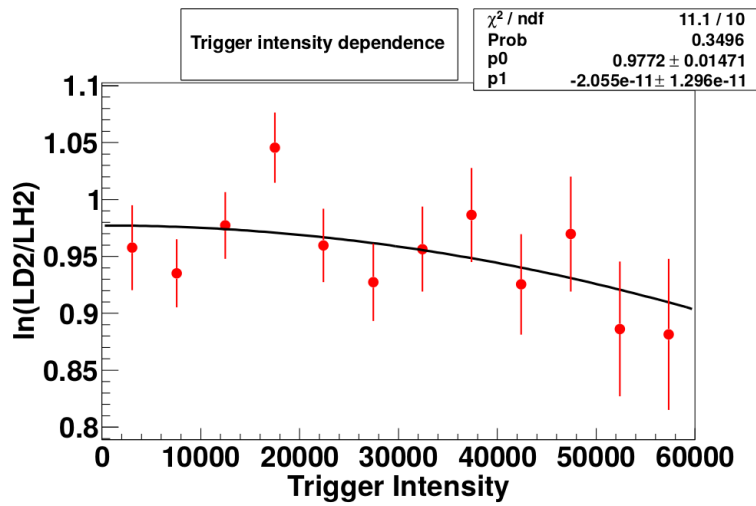


Figure 4.25: The natural log of the ratio of LD2 to LH2 as a function of trigger intensity. It is fit with a quadratic fit that is missing the linear term. The dependence is not as strong as the chamber dependence.

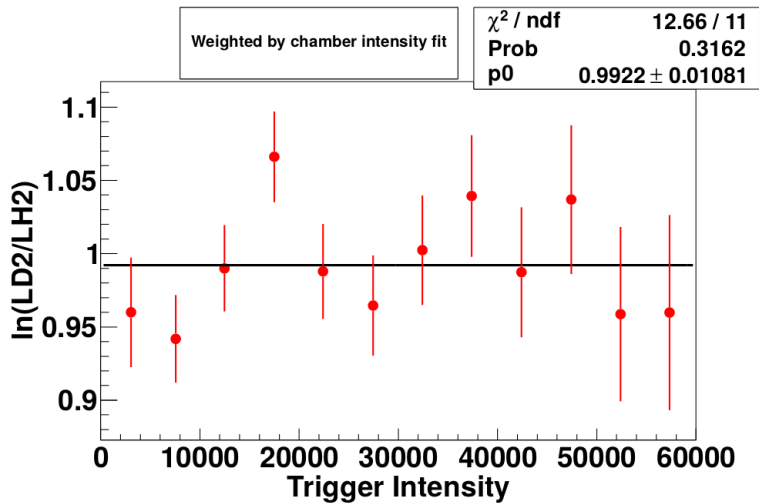


Figure 4.26: The natural log of the ratio of LD2 to LH2 as a function of trigger intensity. The points have been weighted based on a fit to the trigger intensity. It seems flat within the uncertainties.

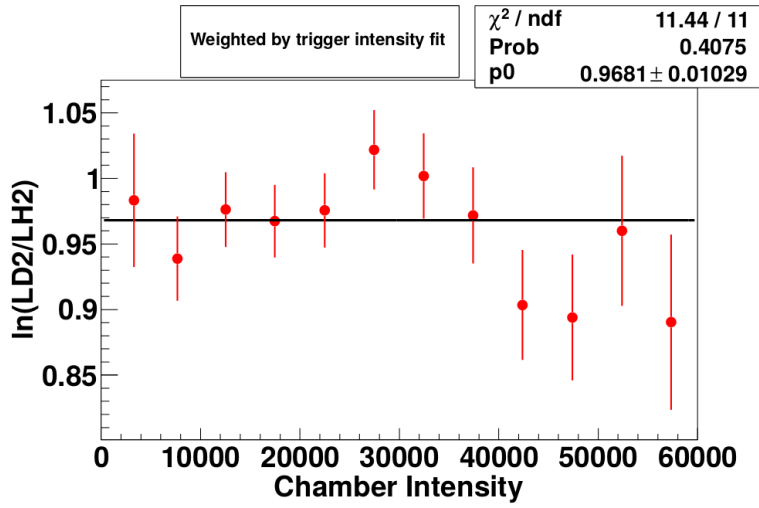


Figure 4.27: The natural log of the ratio of LD2 to LH2 as a function of chamber intensity. The points have been weighted based on a fit to the chamber intensity. It seems flat within the uncertainties.

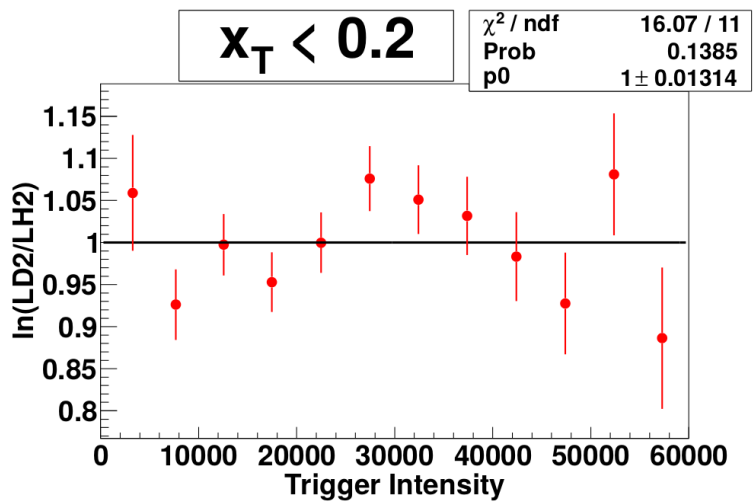


Figure 4.28: The rate dependence of the low x_T data after the remaining rate correction has been applied. It looks reasonably flat.

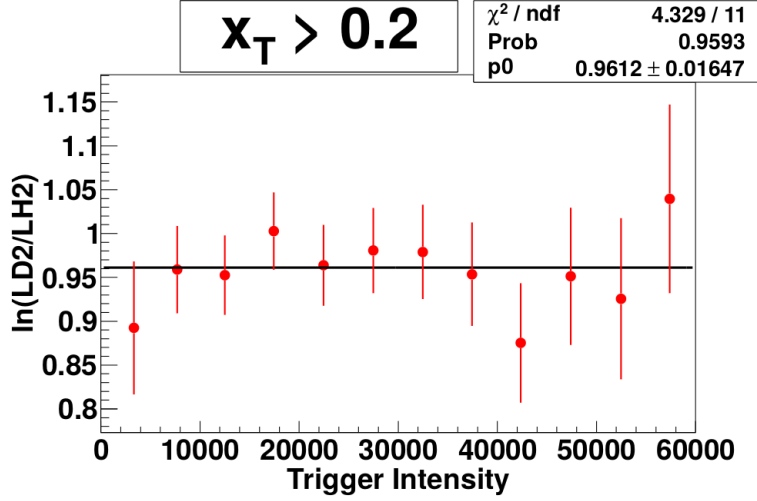


Figure 4.29: The rate dependence of the high x_T data after the remaining rate correction has been applied. It looks reasonably flat.

4.4 Target Contamination

As mentioned earlier, the liquid deuterium target has a significant contamination from 1H . We have to correct for the fact that some dimuons on the LD2 target come from Hydrogen atoms. Using T_x as the target cross section, p as the proton-proton cross section, n as the proton-neutron cross section, $LH2$ and $LD2$ as the cross sections between a proton and the pure material, a and c as the number of protons per atom in LH2 and LD2 targets, and b and d as the number of neutrons per atom in the LH2 and LD2 targets, respectively (which are the fractions of deuterium atoms in those targets):

$$T_H = ap + bn \quad (4.68)$$

$$T_D = cp + dn \quad (4.69)$$

Basic linear algebra results in:

$$LH2 = p = \frac{bT_D - dT_H}{bc - ad} \quad (4.70)$$

$$n = \frac{aT_D - cT_H}{ad - bc} \quad (4.71)$$

$$LD2 = p + n \quad (4.72)$$

a and c are both one, since the number of protons in a hydrogen or deuterium atom are both one. Our LH2 target is also pure to several digits of precision, so we can set b to zero. d ranges between 0.9 and 1, and closer to one the less contamination there is. I will refer to it as Pu for purity for the rest of the thesis.

$$LH2 = p = T_H \quad (4.73)$$

$$n = \frac{T_D - T_H}{Pu} \quad (4.74)$$

$$LD2 = T_H + \frac{T_D - T_H}{Pu} \quad (4.75)$$

The amount of contamination in our target (for most of our data) has an uncertainty. To calculate the uncertainty in the cross section ratio as a result of this I calculate the cross section three times, once with the contamination at the base value and once each with the contamination raised or lowered by the uncertainty. The difference between the base cross section and the cross section at the limits of the contamination is a systematic uncertainty in the cross section ratio. These contamination uncertainties are very asymmetric and are found in table 2.3.

4.5 Logarithm of the Ratio

In previous experiments, what has been published has been \bar{d}/\bar{u} (or \bar{u}/\bar{d}) and cross section ratios. However, I believe the best way to present the data is $\ln(\bar{d}/\bar{u})$ and $\ln(\sigma_{pd}/2\sigma_{pp})$.

In the E866 experiment, there were multiple data sets that were analysed separately before combining their $\sigma_{pd}/2\sigma_{pp}$ results into a single result. Each data set i had a weight W_i equal to $1/\sigma_i^2$, where σ_i is the statistical uncertainty of the ratio in data set i . Using r_i as the ratio of data set i and R as the final ratio, equation 4.76 was used to calculate R for E866[50][30].

$$R = \frac{\sum_i r_i W_i}{\sum_i W_i} \pm \sqrt{1/\sum_i W_i} \quad (4.76)$$

I will use a simple example to show why equation 4.76 is not a good choice. In a hypothetical experiment measuring the ratio $R_{X/Y}$ of events of type X and events of type Y there are two data sets, A and B, where

all conditions are the same. The split into A and B is arbitrary and they could have been one combined data set, which we'll call C. The statistics for each data set are listed in table 4.10.

Data Set	X	Y
A	4	2
B	2	4
C	6	6

Table 4.10: A very simple example of a data set C, arbitrarily split into data sets A and B. Both X and Y follow Poisson distributions.

Now, for a single data set, the statistical uncertainty in X/Y to first order should be equation 4.77. E866 did not use higher order uncertainties[51].

$$\sigma_R = \sqrt{(\sigma_X \frac{1}{Y})^2 + (\sigma_Y \frac{X}{Y^2})^2} \quad (4.77)$$

$$\sigma_R = \frac{X}{Y} \sqrt{(\frac{\sigma_X}{X})^2 + (\frac{\sigma_Y}{Y})^2} \quad (4.78)$$

Which leads us to table 4.11.

Data Set	X	Y	R	σ_X	σ_Y	σ_R	W
A	4	2	2	2	$\sqrt{2}$	$\sqrt{3}$	$\frac{1}{3}$
B	2	4	0.5	$\sqrt{2}$	2	$\frac{\sqrt{3}}{4}$	$\frac{16}{3}$
A merge B			0.59			0.42	5.67
C	6	6	1	$\sqrt{6}$	$\sqrt{6}$	0.58	3

Table 4.11: Table 4.10 with more fields.

Using equation 4.76 to combine data sets A and B, we get a result of $R_{X/Y} = \frac{10}{17} \pm \sqrt{3/17} = 0.59 \pm 0.42$, which is clearly incorrect. The result for C is $R = 1 \pm 0.58$. The data set with the lower ratio has been given too much of a weight, and the data set with the higher ratio has been given too little of a weight, by a large margin. It is clear that the X/Y term in front of the square root in equation 4.78 is the culprit, suggesting that when the values of the data sets being merged are farther apart the mistake will be larger, which will tend to happen for points with higher uncertainties.

Instead of combining the ratios from different data sets, we could combine a different function of both X and Y. Ideally, we'd want something symmetric with respect to X and Y to avoid the above problem. An ideal function would be equal to zero at $X = Y$ and have the property $f(X, Y) = -f(Y, X)$. $\ln(X/Y)$ is such a function.

$$\ln(R) = \ln(X) - \ln(Y) \quad (4.79)$$

$$\sigma_{\ln(R)} = \sqrt{\left(\frac{\sigma_X}{X}\right)^2 + \left(\frac{\sigma_Y}{Y}\right)^2} \quad (4.80)$$

The weights are now no longer biased towards high Y, but give even weight to X statistics and Y statistics. Using $\ln(R)$, its uncertainty, and combining the data sets using equation 4.76 gives a much different result, found in table 4.12. This is the same as calculating a weighted geometric mean, with weights based off of equation 4.80.

Data Set	X	Y	R	$\ln(R)$	σ_X	σ_Y	$\sigma_{\ln(R)}$	W
A	4	2	2	0.693	2	$\sqrt{2}$	$\frac{\sqrt{3}}{2}$	$\frac{4}{3}$
B	2	4	0.5	-0.693	$\sqrt{2}$	2	$\frac{\sqrt{3}}{2}$	$\frac{4}{3}$
A merge B			1	0			0.61	2.67
C	6	6	1	0	$\sqrt{6}$	$\sqrt{6}$	0.58	3

Table 4.12: Like table 4.11, but for a logarithmic study.

Using equation 4.76 to combine data sets A and B, we get a result of $\ln(R_{X/Y}) = 0 \pm 0.61$, which is more sane. The value of R is 1 and the 1σ confidence interval for R is 0.54 to 1.84. The confidence interval for R from C is 0.56 to 1.78, so this isn't perfect, but it is quite an improvement. The confidence interval for R from C using the old method is 0.42 to 1.58. When using the natural log method the lower uncertainty is less while the upper uncertainty is greater. It should also be noted that in more complicated examples where $\ln(R) \neq 0$ that the log method does not find the correct average to 100% accuracy, although it is a lot closer than the old method. This can be improved by calculating uncertainties and expected values with higher order terms.

To convert older data, R can be turned into $\ln(R)$ easily enough. By comparing equations 4.78 and 4.80, we can get equation 4.81.

$$\sigma_{\ln(R)} = \frac{Y}{X} \sigma_R \quad (4.81)$$

Using this on the last data point of E866 for the high mass setting yields table 4.13. Note that the binning is different than that of the combined results from all mass settings that is the most well known E866 data. The difference between the two methods is not very large for the cross section ratio, but \bar{d}/\bar{u} changes by over a factor of two for changes in $\sigma_{pd}/2\sigma_{pp}$ and over a factor of three at higher x in E866,

magnifying the effects of this error for \bar{d}/\bar{u} . I have not been able to get my hands on the combined mass settings results broken down into data sets for E866, so I have not been able to correct those results like this. The correction for those points could be smaller or much larger than this correction. While I will plot E866 data later, keep in mind that the high uncertainty points at high x are likely lower than they should be.

Data Set	Ratio	Stat	Weight	Ln	Ln Stat	Ln Weight
7	0.843	0.277	13.033	-0.171	0.329	9.239
8	0.873	0.179	31.21	-0.136	0.202	24.507
11	1.251	0.448	4.982	0.224	0.358	7.803
E866 merge	0.903	0.143		-0.102	0.129	
ln merge	0.927	0.144		-0.076	0.155	

Table 4.13: Corrected cross section ratio values for the E866 high mass setting. Ratio and Ratio Stat are the traditional cross section ratio and their uncertainties. Log is $\ln(\sigma_{pd}/2\sigma_{pp})$. Log Stat is the uncertainty on $\ln(\sigma_{pd}/2\sigma_{pp})$. Ln Weight is the weight used when combining separate data sets using the log method.

In this analysis I have decided to combine the different data sets before calculating the cross section ratio, so I do not have to worry about the data points in SeaQuest being incorrect because of this effect. The comparison of SeaQuest data to E866 data is inevitable however and the mistake in combining data sets sheds light on potential apparent discrepancies between SeaQuest and E866 data points at high x. However, another reason to use $\ln(R)$ is sensible confidence intervals, and this does apply to SeaQuest. A large uncertainty combined with a low point can put some of the confidence interval for R below zero. The last \bar{d}/\bar{u} point in E866[52] is 0.346 ± 0.396 , which puts some of the interval below zero, a region which is physically impossible. With $\ln(R)$, the confidence interval is restricted to physically possible values. In regular ratio plots, $Y > X$ is crammed between 0 and 1 while $X > Y$ stretches from 1 to infinity. The choice of which value goes in the numerator and which in the denominator is arbitrary, so the presentation of the data should be balanced between the $X > Y$ region and the $Y > X$ region. In a \ln plot $X > Y$ covers the positive half and $Y > X$ covers the negative half and is balanced.

4.6 Cross Section Ratio Calculation

The yield of Drell-Yan events, based on the cross section, can be found in equation 4.82. This can be rearranged to calculate the cross section based off the yield.

$$\sigma * \text{protons} * \text{atomsPerArea} = \text{Yield} \quad (4.82)$$

target	live protons
LH2	2.1402e+17
LD2	1.0632e+17
Empty	4.3201e+16

Table 4.14: The number of live protons on each target.

$$\sigma = \frac{W}{\text{protons} * \text{atomsPerArea}} \quad (4.83)$$

W is the sum of the weights for all dimuons reconstructed from that target. The number of live protons on each target can be found in table 4.14. Without a correction for the acceptance of our spectrometer this should only be used for calculating cross section ratios, where that correction cancels out.

I use $Q_T = \frac{W_T}{P_T * \text{atomsPerArea}_T}$ where the subscripts denote which target. The cross sections are:

$$\sigma_{pp} = Q_H \quad (4.84)$$

$$\sigma_{pd} = Q_H + \frac{Q_D - Q_H}{Pu} \quad (4.85)$$

$$\sigma_{pd} = Q_H * (1 - \frac{1}{Pu}) + \frac{Q_D}{Pu} \quad (4.86)$$

$$\frac{\sigma_{pd}}{2\sigma_{pp}} = \frac{1}{2} \frac{Pu-1}{Pu} + \frac{Q_D}{2Pu * Q_H} \quad (4.87)$$

However, it is better to analyse the natural log of the ratio.

$$L(Q_D, Q_H) \equiv \ln\left(\frac{\sigma_{pd}}{2\sigma_{pp}}\right) = \ln\left(\frac{1}{2} \frac{Pu-1}{Pu} + \frac{Q_D}{2Pu * Q_H}\right) \quad (4.88)$$

$$L(Q_D, Q_H) = \ln(Pu - 1 + \frac{Q_D}{Q_H}) - \ln(2Pu) \quad (4.89)$$

$$L(Q_D, Q_H) = \ln\left(\frac{Pu * Q_H - Q_H + Q_D}{Q_H}\right) - \ln(2Pu) \quad (4.90)$$

$$L(Q_D, Q_H) = \ln(Q_D - (1 - Pu)Q_H) - \ln(Q_H) - \ln(2Pu) \quad (4.91)$$

To analyse the statistical uncertainty on the cross section the statistical uncertainties on Q_H and Q_D are needed. There are two sources of uncertainty, the total number of events on LH2 or LD2 and the average weight of those events. Using \bar{W} as the average weight, Y as the total number of events from that target, and W as the total weight, the equation for the uncertainty on the total weight of events from a target is in equation 4.92. The uncertainty on the average weight is the standard deviation of the mean of the weights. The uncertainty on the yield is $\sqrt{Y_T}$ since it is a Poisson distribution.

$$\sigma_{W_T}^2 = \sigma_{Y_T}^2 \bar{W}_T^2 + \sigma_{\bar{W}_T}^2 Y_T^2 \quad (4.92)$$

$$\sigma_{Q_T}^2 = \frac{\sigma_{W_T}^2}{(P_T * atomsPerArea_T)^2} \quad (4.93)$$

Several partial derivatives are also needed for calculating the expected value to second order and the uncertainty to first order. I believe that with large uncertainties on the points at high x that a first order analysis of the expected value is difficult to justify, even with the log method reducing the need for higher order terms.

$$\frac{\delta_L}{\delta_{Q_D}} = \frac{1}{Pu * Q_H - Q_H + Q_D} \quad (4.94)$$

$$\frac{\delta_L}{\delta_{Q_H}} = \left(\frac{Pu-1}{d * Q_H - Q_H + Q_D} - \frac{1}{Q_H} \right) \quad (4.95)$$

$$\frac{\delta_L^2}{\delta_{Q_D}^2} = \frac{-1}{(Pu * Q_H - Q_H + Q_D)^2} \quad (4.96)$$

$$\frac{\delta_L^2}{\delta_{Q_H}^2} = \frac{-(Pu-1)^2}{(Pu * Q_H - Q_H + Q_D)^2} + \frac{1}{Q_H^2} \quad (4.97)$$

In the following equations I will use σ^2 to indicate the variance, it will not indicate cross sections. $E(variable)$ is the notation for the expected value of that variable. The expected value will use all the terms from a second order Taylor expansion[53], but the uncertainty will just be first order. When I later report the cross section ratios in the results section, I will report $E(\ln(\frac{D}{2H}))$, not $\ln(\frac{E(D)}{2E(H)})$.

$$E(L(Q_D, Q_H)) = L(E(Q_D), E(Q_H)) + \frac{1}{2} \frac{\delta^2 L}{\delta^2 Q_D} \sigma_{Q_D}^2 + \frac{1}{2} \frac{\delta^2 L}{\delta^2 Q_H} \sigma_{Q_H}^2 \quad (4.98)$$

$$\sigma_L^2 = \left(\frac{\delta L}{\delta Q_D}\right)^2 \sigma_{Q_D}^2 + \left(\frac{\delta L}{\delta Q_H}\right)^2 \sigma_{Q_H}^2 \quad (4.99)$$

In order to justify combining all the data before calculating the cross section ratios, I checked the kinematic distributions for each of the large roadsets to make sure they matched. Roadsets 59 and 70 had too few statistics to check in this way. I graphed x_T , x_B , and p_T for all the roadsets with their areas normalized to be equal in figures 4.30 through 4.34. Since they are so similar, this justifies merging the cross section ratio results together. This is the best approach if it can be justified as it keeps the uncertainties as small as possible. The smaller the uncertainties, the more accurate the uncertainty propagation. This also allows the inclusion of data sets where the uncertainties are too large to do a proper \bar{d}/\bar{u} extraction.

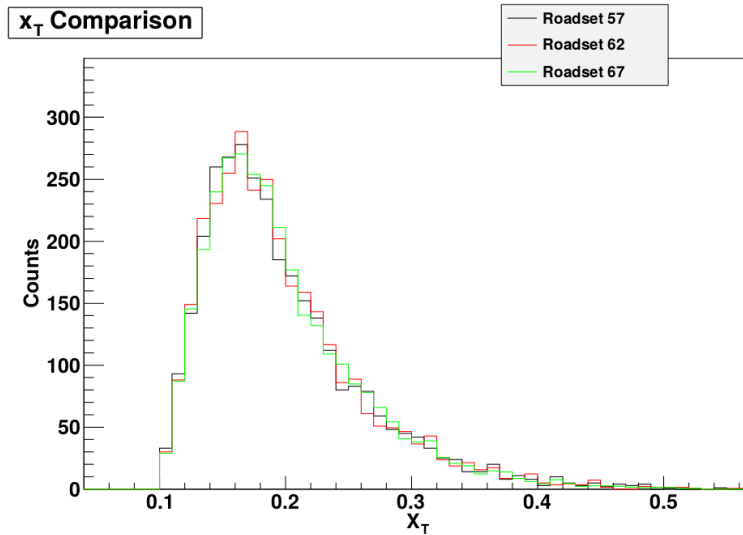


Figure 4.30: Plot of the x_T distribution for all three roadsets. The areas under the curves have been normalized to the same value.

The collaboration decided that statistical uncertainties would be those uncertainties that are uncorrelated between bins and systematic uncertainties would be those uncertainties that are correlated between bins. The basis of this decision is how groups like CTEQ will fit our data. Each point of our data will be allowed to move up and down a distance based on its statistical uncertainty, while the collection of our data points as a whole will be allowed to together move a distance based on the systematic uncertainties. The sources for the statistical uncertainty comes from the statistical uncertainties in the LH2 total weight and LD2 total weight. These sources are added in quadrature. The sources of systematic uncertainty are the kTracker efficiency fits, the empty flask fits, the remaining rate dependence fits, the uncertainty from the target contamination,

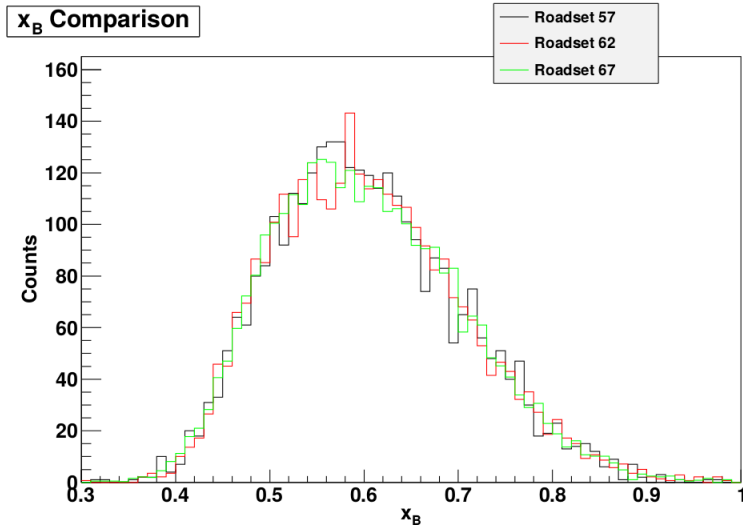


Figure 4.31: Plot of the X_B distribution for all three roadsets. The areas under the curves have been normalized to the same value.

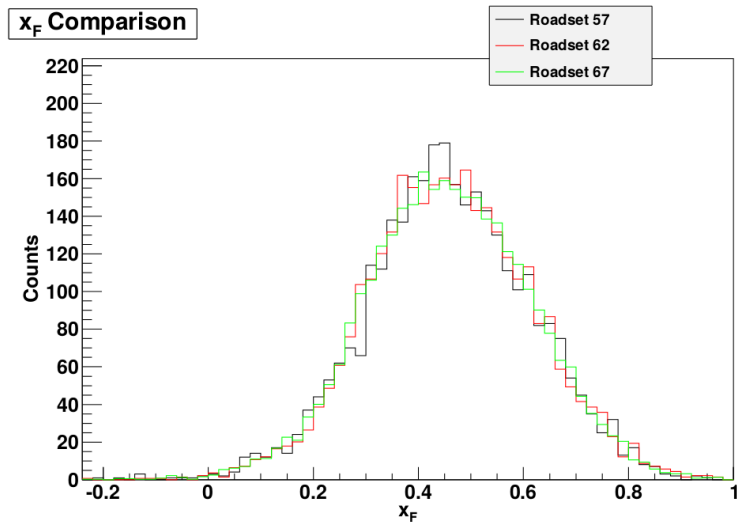


Figure 4.32: Plot of the X_F distribution for all three roadsets. The areas under the curves have been normalized to the same value.

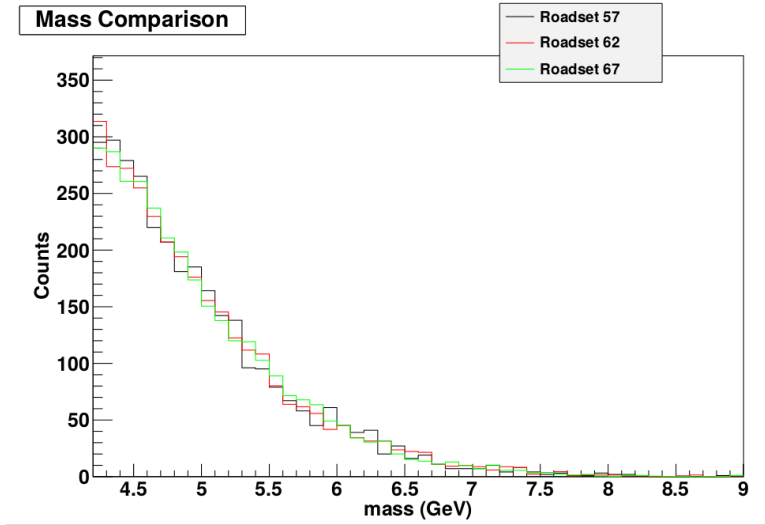


Figure 4.33: Plot of the mass distribution for all three roadsets. The areas under the curves have been normalized to the same value.

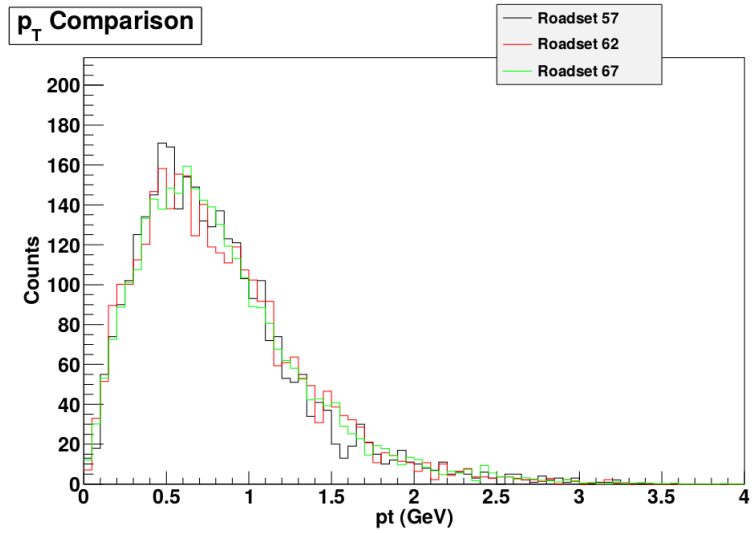


Figure 4.34: Plot of the P_T distribution for all three roadsets. The areas under the curves have been normalized to the same value.

and the uncertainty from nuclear effects in deuterium. All of the systematic uncertainties are added in quadrature.

There is no correction calculated for the contamination of the results from J/Ψ and Ψ' dimuons. In a J/Ψ Monte Carlo reconstructed by kTracker there were no reconstructed dimuons above the mass threshold that passed validity and target cuts. In a Ψ' Monte Carlo reconstructed by kTracker, out of all the valid reconstructed dimuons passing the target cut, 0.31% were above the mass threshold. Some thought is due to how much of a systematic error to place on this, but it will be very small.

There is no correction calculated for the contamination of the results from combinatorial background. As combinatorial background is proportional to intensity² while dimuons are proportional to intensity, the combinatorial background as a fraction of our data should go to zero in the limit that intensity goes to zero. This means it is a rate dependent contamination, and the remaining rate dependence has been corrected for and uncertainties associated with it have been assigned. Once the experiment has taken enough like sign coincidence data then the combinatorial background can be accurately calculated and assigned its own correction. Much care should be taken to estimate how much it overlaps with the empty target and remaining rate dependence corrections.

There is no correction calculated for chamber inefficiency. As mentioned in the kTracker efficiency section, even a non rate dependent chamber inefficiency might affect the rate dependence, and the two effects need to be untangled with more study. However, since we don't know the chamber efficiencies well, then a correction for this can not be made.

4.7 \bar{d}/\bar{u} Extraction

Once the log of the ratio of LD2/LH2 cross sections is obtained from data, which I will call L_d , it is time to calculate \bar{d}/\bar{u} . First, an initial estimate of \bar{d}/\bar{u} is set, although this initial value is not important. Then, for each dimuon in the yield of LH2 and LD2, an estimate of the log of the cross section ratio for that dimuon's mass, x_B , and x_T is calculated with the initial value of \bar{d}/\bar{u} . The mean value of all of the predictions is taken as the prediction of the log of the cross section ratio, which I will call L_p . The difference $L_d - L_p$ is then used to modify the estimate of \bar{d}/\bar{u} . This procedure is then repeated until $L_d = L_p$ within 1e-4.

In all calculations the $\bar{d} + \bar{u}$ distribution and all quark distributions other than \bar{d} and \bar{u} are taken from a PDF set. \bar{d}/\bar{u} inside the analysis range for both beam and target quarks is taken from the current estimate. For the leading order calculation I used MMHT2014lo68cl PDFs. For the NLO calculation I used MMHT2014nlo68cl.

The cross section calculations use some Fortran code provided by W. K. Tung in a private communication to the E866 collaboration[54]. This code can provide LO or NLO cross sections. The NLO cross sections from this code were double checked against numbers provided by Marco Stratmann of DSSV in a private communication[55]. My extraction program can be switched between using the NLO code, the LO code from Tung, or LO C++ code I wrote. I know I have incorporated the Fortran code correctly as the LO results from Fortran match the LO results from the C++ code. The LO calculation is shown below:

$$\begin{aligned} \sigma_{H2} = & 4u(x_B)\bar{u}(x_T) + d(x_B)\bar{d}(x_T) + 4\bar{u}(x_B)u(x_T) + \\ & \bar{d}(x_B)d(x_T) + 8c(x_B)c(x_T) + 2s(x_B)s(x_T) \end{aligned} \quad (4.100)$$

$$\begin{aligned} \sigma_{D2} = & \sigma_{H2} + 4u(x_B)\bar{d}(x_T) + d(x_B)\bar{u}(x_T) + 4\bar{u}(x_B)d(x_T) + \\ & \bar{d}(x_B)u(x_T) + 8c(x_B)c(x_T) + 2s(x_B)s(x_T) \end{aligned} \quad (4.101)$$

$$L_p(\text{single dimuon}) = \ln\left(\frac{\sigma_{D2}}{2\sigma_{H2}}\right) \quad (4.102)$$

Note that due to the terms with anti-quarks from the beam, L_d in one bin can have a small effect on other bins. There is even more entanglement between bins in the NLO calculation (explain how).

The incrementing method is based on the approximation in equation 4.103. This approximation takes the leading order equation, ignores the strange and charm terms, and assumes that the quark is from the beam and the anti-quark from the target, due to our high x_F .

$$\frac{\sigma_{pd}}{\sigma_{pp}} \approx \frac{1 + \frac{d(x_B)}{4u(x_B)}}{1 + \frac{d(x_B)\bar{d}(x_T)}{4u(x_B)\bar{u}(x_T)}} \left(1 + \frac{\bar{d}(x_T)}{\bar{u}(x_T)}\right) \quad (4.103)$$

For the sake of taking up a reasonable amount of space, I will define CSR as $\frac{\sigma_{pd}}{\sigma_{pp}}$, and QR as $\frac{d(x_B)}{4u(x_B)}$ for all dimuons in that bin. Equation 4.103 can be rearranged into equation 4.104

$$\frac{\bar{d}(x_T)}{\bar{u}(x_T)} = \frac{CSR - 1 - QR}{1 + QR - CSR * QR} \quad (4.104)$$

$$\ln\left(\frac{\bar{d}(x_T)}{\bar{u}(x_T)}\right) = \ln(CSR - 1 - QR) - \ln(1 + QR - CSR * QR) \quad (4.105)$$

Taking a derivative leads us to equations 4.106 and 4.107.

$$\frac{\delta \ln(\frac{\bar{d}(x_T)}{\bar{u}(x_T)})}{\delta CSR} = \frac{1}{CSR-1-QR} + \frac{QR}{1+QR-CSR*QR} \quad (4.106)$$

$$\Delta \ln(\frac{\bar{d}(x_T)}{\bar{u}(x_T)}) = \Delta CSR (\frac{1}{CSR-1-QR} + \frac{QR}{1+QR-CSR*QR}) \quad (4.107)$$

QR is calculated for every dimuon and log averaged. ΔCSR is the difference between L_d and L_p . CSR is the average of L_d and L_p . Equation 4.107 is good but not perfect, and NLO computations can take a long time, so I modified it to equation 4.108 where i is the iteration it is on and $F_1 = 1$. This decreases the magnitude of the iteration if it overshoots and increases the magnitude when it falls short. This method converges in about 6 iterations, which is very useful when calculating NLO results.

$$\Delta \ln(\frac{\bar{d}(x_T)}{\bar{u}(x_T)}) = \Delta CSR (\frac{1}{CSR-1-QR} + \frac{QR}{1+QR-CSR*QR}) F_i \quad (4.108)$$

$$F_i = (\frac{\Delta CSR_{i-1}}{\Delta CSR_{i-1} - \Delta CSR_i}) * F_{i-1} \quad (4.109)$$

To confirm that the results do not depend upon the initial estimate, I ran the program with an initial estimate of $\bar{d}/\bar{u} = 0.5$ for all bins and again for an initial estimate of $\bar{d}/\bar{u} = 2.0$ for all bins. The results were identical.

Once \bar{d}/\bar{u} is calculated, the uncertainties are calculated. This requires running the extraction part of the program $2n$ times more, where n is the number of bins. For the first n times, one bin of L_d is adjusted upwards by an amount equal to its statistical uncertainty, while all other bins of L_d stay the same. The last n times are similar, except the bin of L_d is adjusted downwards. The results of each of the $2n$ extractions are compared to the original extraction of \bar{d}/\bar{u} , and the differences are taken as uncertainties. The resulting uncertainties from increasing L_d are then added in quadrature to get the upper statistical uncertainties for \bar{d}/\bar{u} . Similarly for the uncertainties from decreasing L_d and the lower statistical uncertainties. It is important to note that changing L_d in one bin can affect the \bar{d}/\bar{u} results in other bins by a small amount.

In each bin I have calculated \bar{d}/\bar{u} with three different L_d values, which I will call L_- , L_0 , and L_+ . I will call the resulting $\ln(\bar{d}/\bar{u})$ results y_- , y_0 , and y_+ . If we take (L_-, y_-) , (L_0, y_0) , and (L_+, y_+) to be three points, a quadratic form can be fit to these points and used to estimate the expected value of \bar{d}/\bar{u} to second order. If a is the quadratic coefficient and b is the linear coefficient then equation 4.110 gives the formula for the expected value of $\ln(\bar{d}/\bar{u})$. I average the upper and lower statistical uncertainties on L_d to find σ_L .

$$E(\ln(\frac{\bar{d}}{\bar{u}})) = y_0 + a\sigma_L^2 \quad (4.110)$$

To propagate the systematic uncertainty in the cross section ratio, I use equation 4.111 to calculate the portion. The \pm is plus for the upper uncertainty and minus for the lower uncertainty.

$$\sigma_{\ln(\bar{d}/\bar{u})-propagated(sys)} = (b + 2aL_d)\sigma_{L_d(sys)} \pm a\sigma_{L_d}^2 \quad (4.111)$$

There is a source of uncertainty due to nuclear effects in deuterium. The calculations presented in this section have all assumed that $\sigma_D = \sigma_p + \sigma_n$, which may not be entirely accurate, especially at high x. Two papers[56][57] with estimates for the effect on $\sigma_{pd}/2\sigma_{pp}$ were found, but the corrections had opposite signs at high x. It was decided to use the differences between these models and an uncorrected cross section ratio as systematic uncertainties and not to make a correction for this effect. Table 4.7 has a list of the corrections to the deuterium cross section. The numbers from [56] are not exact, they were eyeballed off of a graph in their paper.

min x	max x	$\frac{\sigma_{pd}}{(\sigma_p + \sigma_n)}$ [57]	$\frac{\sigma_{pd}}{(\sigma_p + \sigma_n)}$ [56]
0.1	0.13	0.981	0.99
0.13	0.16	0.980	0.98
0.16	0.195	0.980	0.97
0.195	0.24	0.980	0.97
0.24	0.29	0.983	0.96
0.29	0.35	0.989	0.95
0.35	0.45	1.003	0.96
0.45	0.58	1.050	0.96

Table 4.15: Models comparing the cross section of deuterium to what it would be if the nucleons were free.

The uncertainties in the PDF set are also taken as a systematic uncertainty. LHAPDF, the program I use to access the PDFs, contains a function that will return the uncertainty in any function of parton distribution functions you submit. Using the average x_b and Q values in each bin I submitted the function in the right hand side of equation 4.104 to get the uncertainty on $\bar{d}(x)/\bar{u}(x)$, then divided that value by $\bar{d}(x)/\bar{u}(x)$ to get the uncertainty on $\ln(\bar{d}(x)/\bar{u}(x))$. This is a crude estimation of the uncertainty from the PDFs but this uncertainty is small. I also add a systematic uncertainty in each bin due to the uncertainty in \bar{d}/\bar{u} above $x = 0.58$. I estimate this systematic uncertainty by running the extraction two more times, once with $\bar{d}/\bar{u} = 1.0$ and once with it equal to the log average of the last two points. I also estimate an additional systematic uncertainty associated with my choice of PDF set by running the extraction three more times using the PDF sets CT14nlo, and abm11.5n.as.nlo. All of the systematic uncertainties have upper and lower

uncertainties estimated separately. All of the systematic uncertainties are added in quadrature.

Chapter 5

Results

The two main goals of this entire analysis are the estimation of the natural log of the cross section ratio, $\ln(\frac{\sigma_{pd}}{2\sigma_{pp}})$ and the estimation of the natural log of the ratio of sea antiquarks, $\ln(\frac{\bar{d}}{\bar{u}})$, both as a function of x . The uncertainties on these values are also an essential part of the result. $\ln(\frac{\bar{d}}{\bar{u}})$ is the more fundamental physics result of the two, and is the more important result that way. However, future experimenters and theorists will be taking $\ln(\bar{d}/\bar{u})$ from PDFs generated by groups such as CTEQ who fit the data from dozens of different experiments instead of directly using the SeaQuest results. Undoubtedly SeaQuest will have an important influence on these fits but groups such as CTEQ will be asking for our cross section ratio data, so in one sense the cross section ratio is the main result of our experiment.

5.1 Cross Section Ratio

Not just our results are important in the use of our data by fitting groups, but the kinematics of those results. The average kinematics of events in each bin of x_T for the LH2 target is in table 5.1 and for the LD2 target is in table 5.2. The total weights of the LH2 dimuons in each bin at each step of the analysis are shown in table 5.3 and the weights of the LD2 dimuons are in table 5.4. $\ln(\frac{2\sigma_{pd}}{2\sigma_{pp}})$ and its uncertainties for each bin in x_T is shown in table 5.5. A breakdown of the various uncertainties are provided in tables 5.6 and 5.7. A graph of the results is shown in figure 5.1.

x_T range	$\langle x_T \rangle$	$\langle x_B \rangle$	$\langle Q^2 \rangle$	$\langle p_T \rangle$
0.1-0.13	0.1199	0.7415	19.12	0.6993
0.13-0.16	0.146	0.6465	20.41	0.7523
0.16-0.195	0.1766	0.5894	22.63	0.7855
0.195-0.24	0.2148	0.565	26.52	0.8317
0.24-0.29	0.2626	0.5485	31.65	0.8571
0.29-0.35	0.3153	0.5383	37.4	0.9045
0.35-0.45	0.3852	0.5155	44.15	0.8284
0.45-0.58	0.4925	0.5143	56.34	0.911

Table 5.1: This table lists the average kinematics for reconstructed dimuons from the LH2 target. The dimuons were weighted with the rate dependence weights.

x_T range	$\langle x_T \rangle$	$\langle x_B \rangle$	$\langle Q^2 \rangle$	$\langle p_T \rangle$
0.1-0.13	0.12	0.7468	19.24	0.7138
0.13-0.16	0.146	0.6484	20.48	0.7463
0.16-0.195	0.1768	0.5903	22.7	0.7788
0.195-0.24	0.2151	0.5655	26.66	0.7976
0.24-0.29	0.2624	0.5533	31.96	0.8298
0.29-0.35	0.3155	0.5382	37.51	0.867
0.35-0.45	0.3863	0.5293	45.39	0.8763
0.45-0.58	0.4915	0.5126	56.2	0.8043

Table 5.2: This table lists the average kinematics for reconstructed dimuons from the LD2 target. The dimuons were weighted with the rate dependence weights.

x_T range	raw yield	kTracker efficiency correction	empty flask correction
0.1-0.13	1417	1991	1742
0.13-0.16	3892	5583	4888
0.16-0.195	4676	6854	6005
0.195-0.24	3722	5628	432
0.24-0.29	1940	3082	2699
0.29-0.35	974	1610	1411
0.35-0.45	373	656.7	575
0.45-0.58	67	134.2	117.4

Table 5.3: This table lists how many dimuons were reconstructed from the LH2 target for each bin, and the total weight of all the dimuons at each step.

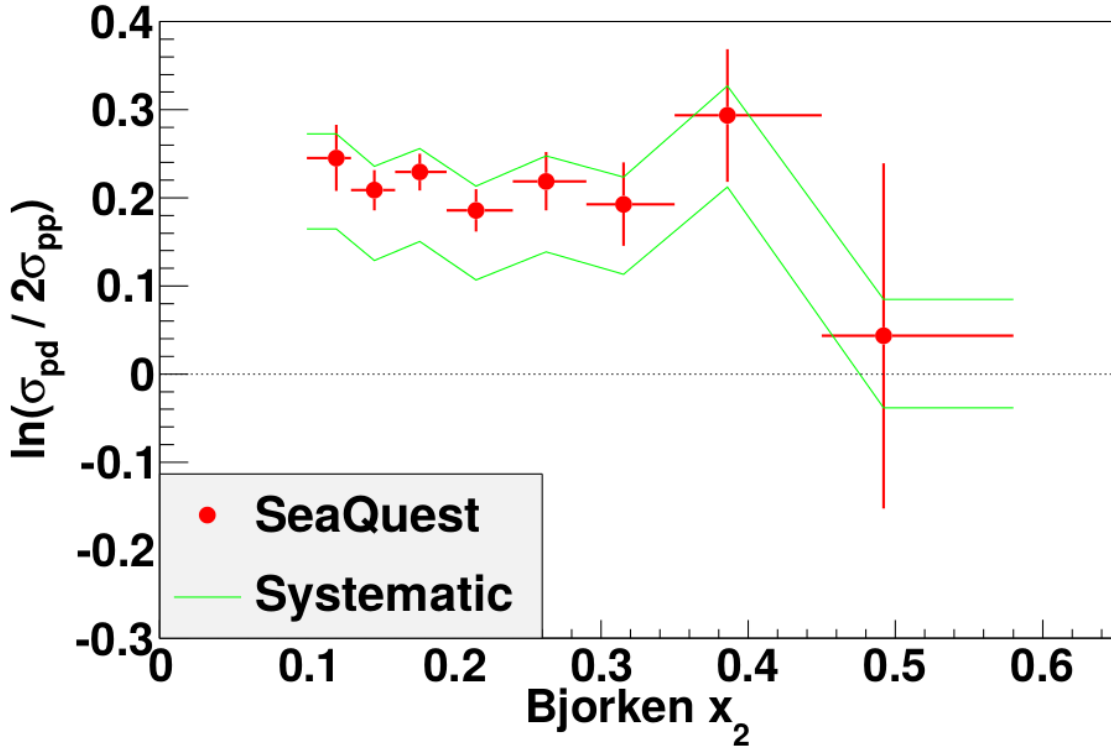


Figure 5.1: A graph of $\ln(\frac{\sigma_{pd}}{2\sigma_{pp}})$ as a function of x_T .

x_T range	yield	kTracker efficiency correction	empty flask correction	full correction
0.1-0.13	1697	2478	2322	2392
0.13-0.16	4491	6711	6291	6479
0.16-0.195	5534	8418	7896	8121
0.195-0.24	4177	6625	6213	6393
0.24-0.29	2238	3742	3509	3612
0.29-0.35	1095	1907	1789	1840
0.35-0.45	470	856.9	804.3	825.6
0.45-0.58	67	135.2	126.9	130.5

Table 5.4: This table lists how many dimuons were reconstructed from the LD2 target for each bin, and the total weight of all the dimuons at each step.

x_T range	$\langle x_T \rangle$	$\ln(\frac{2\sigma_{pd}}{2\sigma_{pp}})$	statistical	upper systematic	lower systematic
0.1-0.13	0.12	0.2453	0.03754	0.02712	0.08056
0.13-0.16	0.146	0.2086	0.02294	0.02693	0.07994
0.16-0.195	0.1767	0.2292	0.02087	0.02654	0.07884
0.195-0.24	0.215	0.1858	0.02385	0.02732	0.0787
0.24-0.29	0.2625	0.2187	0.03301	0.02901	0.07988
0.29-0.35	0.3154	0.1928	0.04736	0.03065	0.07943
0.35-0.45	0.3857	0.2936	0.07533	0.0335	0.08126
0.45-0.58	0.492	0.04333	0.196	0.04128	0.0818

Table 5.5: $\ln(\frac{\sigma_{pd}}{2\sigma_{pp}})$ and its uncertainties for each bin.

x_T range	Tracking Efficiency	Empty Target Subtraction	Remaining Rate Dependence	Target Contamination
0.1-0.13	0.02076	0.007891	0.01526	0.003095
0.13-0.16	0.02065	0.007861	0.01510	0.003028
0.16-0.195	0.02051	0.007784	0.01462	0.003066
0.195-0.24	0.02148	0.007682	0.01474	0.002984
0.24-0.29	0.02347	0.007828	0.01483	0.003047
0.29-0.35	0.02564	0.007761	0.01457	0.002998
0.35-0.45	0.02913	0.008199	0.01402	0.003181
0.45-0.58	0.03768	0.008392	0.01437	0.002688

Table 5.6: A breakdown of the upper uncertainties on $\ln(\frac{\sigma_{pd}}{2\sigma_{pp}})$. Efficiency is the systematic uncertainty from the kTracker efficiency corrections. Empty is the uncertainty from the empty flask corrections. Remaining rate is the uncertainty from the corrections for the remaining rate dependence. Contamination is the uncertainty for the target contamination correction.

x_T range	Tracking Efficiency	Empty Target Subtraction	Remaining Rate Dependence	Target Contamination
0.1-0.13	0.02077	0.006994	0.07446	0.02161
0.13-0.16	0.02065	0.006968	0.07395	0.02113
0.16-0.195	0.02052	0.006913	0.07272	0.0214
0.195-0.24	0.02149	0.006827	0.07247	0.02082
0.24-0.29	0.02348	0.006943	0.07300	0.02126
0.29-0.35	0.02566	0.006894	0.07187	0.02092
0.35-0.45	0.02913	0.007236	0.07217	0.02221
0.45-0.58	0.03774	0.00743	0.06972	0.01873

Table 5.7: A breakdown of the lower uncertainties on $\ln(\frac{\sigma_{pd}}{2\sigma_{pp}})$. The fields are the same as in table 5.6.

5.2 \bar{d}/\bar{u}

$\ln(\frac{\bar{d}}{\bar{u}})$ and its uncertainties can be found in table 5.8. A breakdown of the lower and upper uncertainties into its parts can be found in tables 5.9 and 5.10. A graph of the results along with the results from E866 and NA51 can be found in figure 5.2.

x range	$\langle x \rangle$	$\ln(\frac{\bar{d}}{\bar{u}})$	statistical +	statistical -	systematic +	systematic -
0.1-0.13	0.12	0.4248	0.04545	0.04664	0.04425	0.1563
0.13-0.16	0.146	0.3955	0.0319	0.03361	0.04747	0.1721
0.16-0.195	0.1767	0.4356	0.03095	0.03137	0.06043	0.167
0.195-0.24	0.215	0.3903	0.04211	0.03977	0.07345	0.1709
0.24-0.29	0.2625	0.4574	0.05549	0.05637	0.09165	0.1775
0.29-0.35	0.3154	0.4563	0.08609	0.08755	0.1202	0.1799
0.35-0.45	0.3857	0.6998	0.1396	0.1438	0.1496	0.1694
0.45-0.58	0.492	0.3013	0.446	0.5597	0.1327	0.2718

Table 5.8: $\ln(\frac{\bar{d}}{\bar{u}})$ and its uncertainties, binned in x.

x Range	$\sigma_{pd}/2\sigma_{pp}$	PDF Uncertainty	\bar{d}/\bar{u} very high x	PDF Choice	Deuterium Nuclear Effects
0.1-0.13	0.03296	0.01824	4.318e-05	0.008149	0.02174
0.13-0.16	0.03727	0.006992	7.131e-05	0.01341	0.02522
0.16-0.195	0.03928	0.006418	0.0001408	0.01982	0.04093
0.195-0.24	0.04844	0.005004	0.0001028	0.02904	0.04669
0.24-0.29	0.0488	0.00575	0.0001378	0.04724	0.06126
0.29-0.35	0.05588	0.00498	0.0002164	0.06928	0.08057
0.35-0.45	0.06259	0.007403	0.000508	0.1139	0.07364
0.45-0.58	0.1034	0.001116	0.0006944	0.03736	0.0743

Table 5.9: The breakdown of upper systematic uncertainties on $\ln(\frac{\bar{d}}{\bar{u}})$. Propagated is the systematic uncertainty propagated from the cross section ratio. PDF uncertainty is the uncertainty within the PDF set. PDF high x is the uncertainty from the unknown value of $\ln(\frac{\bar{d}}{\bar{u}})$ outside of our measuring range. PDF group is the systematic uncertainty from the choice of PDF set, i.e. we chose MMHT2014 instead of CT14. Nuclear correction is the systematic uncertainty from nuclear effects in deuterium.

The SeaQuest data shows no sign of dropping off at higher x like the E866 does, and the statistical significance is strong up to the end of the E866 data. The data clearly shows that \bar{d} does not drop below \bar{u} , removing a feature from the data that models had great difficulty in adjusting to. Our data is consistent with E866 except for a couple of points in their high x region where their high uncertainties combined with their error in merging the results of multiple data sets together has likely offset their data to lower than it should be. Our data indicates that $\bar{d}(x)/\bar{u}(x)$ flattens out at higher x , but with the high uncertainties it is not possible to conclude whether it continues to slowly increase, flatten out asymptotically, or turn back

x Range	$\sigma_{pd}/2\sigma_{pp}$	PDF Uncertainty	\bar{d}/\bar{u} very high x	PDF Choice	Deuterium Nuclear Effects
0.1-0.13	0.1015	0.02129	0.0004413	0.1169	0
0.13-0.16	0.1245	0.008956	0.0008264	0.1184	0
0.16-0.195	0.1207	0.006784	0.0007852	0.1152	0
0.195-0.24	0.1224	0.005051	0.0008979	0.1192	0
0.24-0.29	0.1379	0.005786	0.001241	0.1116	0
0.29-0.35	0.1477	0.005012	0.001977	0.1025	0
0.35-0.45	0.1553	0.00743	0.004794	0.06692	0.00557
0.45-0.58	0.2198	0.001123	0.008525	0.1273	0.09649

Table 5.10: The breakdown of lower systematic uncertainties on $\ln(\frac{\bar{d}}{\bar{u}})$. The fields are the same as in table 5.9.

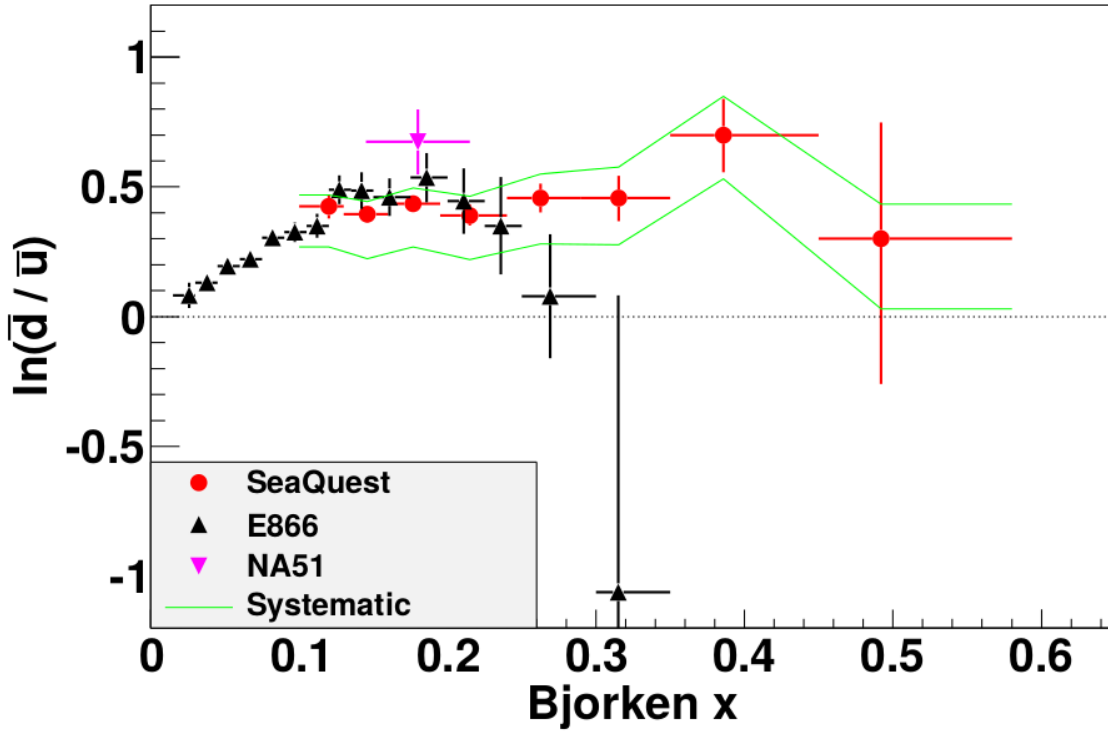


Figure 5.2: A graph of $\ln(\frac{\bar{d}}{\bar{u}})$ as a function of x.

around towards $\bar{d}(x) = \bar{u}(x)$. Figure 5.2 shows our \bar{d}/\bar{u} results again, this time plotted with the $\bar{d}(x)/\bar{u}(x)$ values of two recent PDF sets. Our data indicates that these ratios should be higher above $x = 0.25$; the PDF ratios are likely lower than they should be due to the E866 data. PDF parametrizations were updated after E866, and I expect that the next set of PDF parametrizations will be updated to include the SeaQuest results.

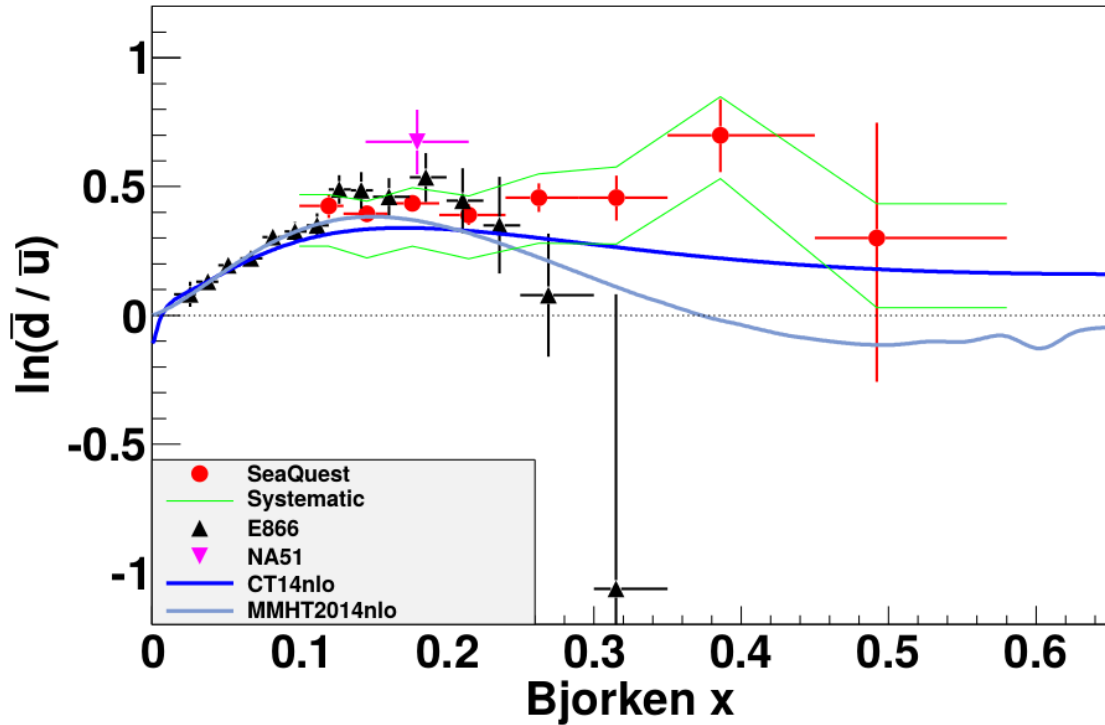


Figure 5.3: A graph of $\ln(\frac{\bar{d}}{\bar{u}})$ as a function of x , with comparison to two recent nlo PDF parametrizations. It is likely that these parametrizations above $x = 0.25$ will change with the publication of SeaQuest data.

Chapter 6

Conclusions

The several main points to take away from this analysis are:

- $\bar{d}(x)/\bar{u}(x)$ has been measured at SeaQuest at x between values of 0.1 and 0.58.
- This result is consistent with past experiments with the exception of a couple of high x data points from E866, but this inconsistency has an explanation.
- The results overturn the E866 result that $\bar{d} < \bar{u}$ at x past 0.3. This result is good news for the many models attempting to accurately describe the mechanism behind the flavor asymmetric sea, as the feature of $\bar{d}/\bar{u} < 1$ was difficult to incorporate into these models.
- This measurement shows that current $\bar{d}(x)/\bar{u}(x)$ ratios in PDFs are too low at x past 0.25.
- It is worth considering exactly how to estimate x from measured quantities for Drell-Yan events as the partons tend to have high p_T that makes all known approximations less accurate.
- Uncertainties in the hydrogen contamination of the deuterium target for the earlier data lead to a large contribution to the systematic error.
- The rate correction due to SeaQuest's unstable beam is very complicated. A detailed attempt at a correction was attempted in this thesis, and despite the large improvements to our data I think the rate correction could possibly be improved with a better background subtraction method.
- Care needs to be taken to merge data sets when studying ratios of measured quantities to avoid an error that systematically reduces the value of the ratio.
- While a simple $\bar{d}(x)/\bar{u}(x)$ presentation of results is more intuitive, a less mathematically misleading presentation of this ratio is $\ln(\bar{d}(x)/\bar{u}(x))$.
- This thesis has not analysed all of the data taken. There is a lot of data from run 5 that has an extra wire chamber installed to measure higher x events. The spectrometer had changed enough that I did

not consider this new data stable enough for this thesis, but there is every reason to think that it will be analysed in a future publication. Another advantage of any newer data is the pure deuterium target that will avoid the large systematic uncertainties associated with target contamination.

References

- [1] M. Gell-Mann. A schematic model of baryons and mesons. *Physics Letters*, 8:214–215, 1964.
- [2] G. Zweig. An su_3 model for strong interaction symmetry and its breaking. 1964.
- [3] O. W. Greenberg. Spin and unitary-spin independence in a paraquark model of baryons and mesons. *Physical Review Letters*, 13:598–602, 1964.
- [4] Michael E. Peskin and Daniel V. Schroeder. *An Introduction to Quantum Field Theory*. Westview Press, 1 edition, 1995.
- [5] Francis Halzen and Alan D. Martin. *Quarks & Leptons: An Introductory Course in Modern Particle Physics*. John Wiley & Sons, 1 edition, 1984.
- [6] J. D. Bjorken and E. A. Paschos. Inelastic electron-proton and γ -proton scattering and the structure of the nucleon. *Physical Review*, 185:1975–1982, 1969.
- [7] E. D. Bloom et. al. High energy inelastic e-p scattering at 6° and 10° . *Physical Review Letters*, 23:930–934, 1969.
- [8] M. Breidenbach et. al. Observed behavior of highly inelastic electron proton scattering. *Physical Review Letters*, 23:935–939, 1969.
- [9] David J. Gross and Frank Wilczek. Ultraviolet behavior of non-abelian gauge theories. *Physical Review Letters*, 30:1343–1346, 1973.
- [10] H. David Politzer. Reliable perturbative results for strong interactions. *Physical Review Letters*, 30:1346–1349, 1973.
- [11] J. D. Bjorken. Asymptotic sum rules at infinite momentum. *Physical Review*, 179:1547–1553, 1968.
- [12] Graeme Watt, Mike Whalley, Joanne Bentham, and Frank Krauss. The durham hepdata project. <http://hepdata.cedar.ac.uk/pdf/pdf3.html>.
- [13] CTEQ Collaboration. Ct10 parton distribution functions, 2010.
- [14] G. Altarelli and G. Parisi. Asymptotic freedom in parton language. *Nuclear Physics*, 126:298–318, 1977.
- [15] Sidney D. Drell and Tung-Mow Yan. Massive lepton-pair production in hadron-hadron collisions at high energies. *Physical Review Letters*, 25:316–320, 1970.
- [16] T-M. Yan. Naive drell-yan and its successor. arXiv preprint hep-ph/9810268, 1998.
- [17] D. C. Hom et. al. Production of high mass muon pairs in hadron collisions at 400 gev. *Physical Review Letters*, 37:1374, 1976.
- [18] K. J. Anderson et. al. Inclusive μ -pair production at 150 gev by π^+ mesons and protons. *Physical Review Letters*, 37:799, 1976.

- [19] G. Altarelli, R.K. Ellis, and G. Martinelli. Large perturbative corrections to the drell-yan process in qcd. *Nuclear Physics B*, 157:461–497, 1979.
- [20] John C. Collins and Davison E. Soper. Angular distribution of dileptons in high-energy hadron collisions. *Physical Review D*, 16:2219–2225, 1977.
- [21] B. Pasquini and P. Schweitzer. Pion tmds in light-front constituent approach, and boer-mulders effect in the pion-induced drell-yan process. *Physical Review D*, 90:014050, 2014.
- [22] Kurt Gottfried. Sum rule for high-energy electron-proton scattering. *Physical Review Letters*, 18:1174–1177, 1967.
- [23] P. Amaudruz et. al. Gottfried sum from the ratio f_2^p/f_2^n . *Physical Review Letters*, 66:2712–2715, 1991.
- [24] D. Allasia et. al. Measurement of the neutron and the proton f_2 structure function ratio. *Physics Letters B*, 249:366–372, 1990.
- [25] A. Baldit et. al. Study of the isospin symmetry breaking in the light quark sea of the nucleon from the drell-yan process. *Physics Letters B*, 332:244–250, 1994.
- [26] E. A. Hawker et. al. Measurement of the light antiquark flavor asymmetry in the nucleon sea. *Physical Review Letters*, 80:3715–3718, 1998.
- [27] R. S. Towell. Improved measurement of the \bar{d}/\bar{u} asymmetry in the nucleon sea. *Physical Review D*, 64:052002, 2001.
- [28] Isenhower et. al. Drell-yan measurements of nucleon and nuclear structure with the fnal main injector. Funding Proposal submitted to The United States Department of Energy, May 2005.
- [29] J. Arrington et. al. Drell-yan measurements of nucleon and nuclear structure with the fermilab main injector: E906. Fermilab 2006 PAC proposal, Oct. 2006.
- [30] R. S. Towell. *Measurement of the Antiquark Flavor Asymmetry in the Nucleon Sea*. PhD thesis, University of Texas at Austin, 1999.
- [31] Schub et. al. Measurement of J/ψ and ψ' production in 800 GeV/c proton-gold collisions. *Physical Review D*, 52:1307, 1995.
- [32] R. D. Field and R. P. Feynman. Quark elastic scattering as a source of high-transverse-momentum mesons. *Physical Review D*, 15:2590–2616, 1977.
- [33] F. M. Steffans and A. W. Thomas. The flavor asymmetry of the nucleon sea. *Physical Review C*, 55:900, 1997.
- [34] Wen-Chen Chang and Jen-Chieh Peng. Flavor structure of the nucleon sea. *Progress in Particle and Nuclear Physics*, 79:95–135, 2014.
- [35] J. Alwall and G. Ingelman. Quark asymmetries in the proton from a model for parton densities. *Physical Review D*, 71:094015, 2005.
- [36] Huiying Song, Xinyu Zhang, and Bo-Qiang Ma. Light flavor asymmetry of nucleon sea. *The European Physical Journal C-Particles and Fields*, 71:1–10, 2011.
- [37] M. Wakamatsu. Transverse momentum distributions of quarks in the nucleon from the chiral quark soliton model. *Physical Review D*, 79:094028, 2009.
- [38] Claude Bourrely and Jacques Soffer. A statistical approach for polarized parton distributions. *The European Physical Journal C-Particles and Fields*, 23:487–501, 2002.
- [39] Particle Data Group. Atomic and nuclear properties of materials for more than 300 materials. <http://pdg.lbl.gov/2015/AtomicNuclearProperties/>, Aug. 2014.

- [40] National Institute of Standards and Technology. Thermophysical properties of fluid systems. <http://webbook.nist.gov/chemistry/fluid/>, Sept 2015.
- [41] W. R. Leo. *Techniques for Nuclear and Particle Physics Experiments*. Springer-Verlag, 2 edition, 1994.
- [42] Randall Evan McClellan. *Angular Distributions of High-Mass Dilepton Production in Hadron Collisions*. PhD thesis, University of Illinois at Urbana-Champaign, 2016.
- [43] Bryan P. Dannowitz. *Nuclear Dependence of Proton-Induced Drell-Yan Dimuon Production at 120 GeV at SeaQuest*. PhD thesis, University of Illinois at Urbana-Champaign, 2016.
- [44] Moreno et. al. Dimuon production in proton-copper collisions at $\sqrt{s}=38.8$ GeV. *Physical Review D*, 43:2815–2835, 1991.
- [45] Particle Data Group. *Particle Physics Booklet*. 2008.
- [46] Dennis Wright. Physics i: Physics lists. <http://geant4.slac.stanford.edu/SLACTutorial14/Physics1.pdf>, March 2014.
- [47] Geant4 Collaboration. Geant4 user’s guide for application developers. <http://geant4.web.cern.ch/geant4/UserDocumentation/UsersGuides/ForApplicationDeveloper/html/>, December 2016.
- [48] Dan Sunday. Intersections of lines and planes. http://geomalgorithms.com/a05-_intersect-1.html, 2012.
- [49] Edwin B. Wilson. Probable inference, the law of succession, and statistical inference. *Journal of the American Statistical Association*, 22:209–212, 1927.
- [50] Eric Andrew Hawker. *Measurement of the Flavor Asymmetry in the Nucleon Sea*. PhD thesis, Texas A&M University, 1998.
- [51] R. S. Towell. Email.
- [52] R. S. Towell et al. Improved measurement of the \bar{d}/\bar{u} asymmetry in the nucleon sea. *Physical Review D*, 64:052002, 2001.
- [53] D Vaja S Mekid. Propagations of uncertainty: Expressions of second and third order uncertainty with third and fourth moments. *Journal of the International Measurement Confederation*, 41:600–609, 2008.
- [54] W. K. Tung. Drell-yan nlo program. Email.
- [55] Marco Stratmann. Drell-yan nlo calculations. Email.
- [56] P.J. Ehlers, A. Accardi, L.T. Brady, and W. Melnitchouk. Nuclear effects in the proton-deuteron drell-yan process. *Physical Review D*, 90:014010, 2014.
- [57] H. Kamano and T.-S. H. Lee. Pion-exchange and fermi-motion effects on the proton-deuteron drell-yan process. *Physical Review D*, 86:094037, 2012.